ALMA MATER STUDIORUM UNIVERSITÀ DI BOLOGNA

DOTTORATO DI RICERCA IN
GEOFISICA

Ciclo XXVII

Settore Concorsuale di afferenza: 04/A4

Settore Scientifico disciplinare: GEO/10

Secondary Microseisms Characterization and Green's Function Extraction at the Larderello-Travale Geothermal Field (Italy)

Presentata da: Maria Zupo

Coordinatore Dottorato
Prof. M. Dragoni

Relatore
Ph.D. Gilberto Saccorotti

Esame Finale Anno: 2015

Abstract

Over the past ten years, the cross-correlation of long-time series of ambient seismic noise (ASN) has been widely adopted to extract the surface-wave part of the Green's Functions (GF). This stochastic procedure relies on the assumption that ASN wave-field is diffuse and stationary. At frequencies < 1 Hz, the ASN is mainly composed by surface-waves, whose origin is attributed to the sea-wave climate. Consequently, marked directional properties may be observed, which call for accurate investigation about location and temporal evolution of the ASN-sources before attempting any GF retrieval. Within this general context, this thesis is aimed at a thorough investigation about feasibility and robustness of the noise-based methods toward the imaging of complex geological structures at the local ($\sim$ 10-50km) scale. The study focused on the analysis of an extended (11 months) seismological data set collected at the Larderello-Travale geothermal field (Italy), an area for which the underground geological structures are well-constrained thanks to decades of geothermal exploration.

Focusing on the secondary microseism band (SM; $f > 0.1$ Hz), I first investigate the spectral features and the kinematic properties of the noise wavefield using beamforming analysis, highlighting a marked variability with time and frequency. For the 0.1-0.3 Hz frequency band and during Spring-Summer-time, the SMs waves propagate with high apparent velocities and from well-defined directions, likely associated with ocean-storms in the southern hemisphere. Conversely, at frequencies > 0.3 Hz the distribution of back-azimuths is more scattered, thus indicating that this frequency-band is the most appropriate for the application of stochastic techniques. For this latter frequency interval, I tested two correlation-based methods, acting in the time (NCF) and frequency (modified-SPAC) domains, respectively yielding estimates of the group- and phase-velocity dispersions. Velocity data provided by the two methods are markedly discordant; comparison with independent geological and geophysical constraints suggests that NCF results are more robust and reliable.

Contents

List of Figures

List of Tables

Introduction

Seismological studies traditionally approached the investigation of the velocity structures of the Earth's interior through the observation of seismic waves generated by earthquakes and active sources. Consequently, the continuous background vibrations superimposed on all recorded seismic time-series, have been normally discarded, because considered as a disturbance, and hence termed *noise*.

The recent expansion of large seismic arrays of long-period seismic stations, and the increased computational and data storage capacities allowed the inspection of the average properties of seismic noise wave-field. Hence, stochastic approaches provided proofs for coherent information carried by noise waves, thus allowing their exploitation to the purpose of subsoil imaging.

Spectra of the ambient noise of natural origin have most of the energy concentrated at frequencies below 1 Hz, a signal which is generally referred to as *microseism*. For these signals, early investigations (e.g. Milne, 1883; Longuet-Higgins, 1950; Haubrich et al., 1963; Asten and Henstridge, 1984; Kibblewhite and Wu, 1991; Babcock et al., 1994; Cessaro, 1994; Webb, 1998; Stutzmann et al., 2009) established a connection with ocean waves movements and interactions resulting in seismic vibrations that mirror the sea-state variability.

The most energetic portions of microseism's spectra are named *secondary microseism* (SM), whose origin is likely due to the non-linear interaction of gravity waves traveling in opposite directions, that generate standing waves coupled to the sea-floor (e.g Longuet-Higgins, 1950). The SM are also known as *double frequency microseisms*, as their main frequency peak (spanning the

0.1-0.2 Hz frequency band, with shoulder peaks up to 1 Hz) is twice the ocean wave spectral peak that generates them (e.g. Kibblewhite and Wu, 1991).

The main component of SM are the Rayleigh surface waves, that travel within the waveguide constituted by the sea-floor layer, ans whose low attenuation allows SM to travel long distances (e.g Haubrich et al., 1963; Lacoss et al., 1969; Roux et al., 2005). The dependence of surface-waves velocity on the frequency (dispersion) is the property used to derive vertical profiles of the shear-wave velocities, which allows for the indirect probing of the mechanical properties of the subsoil over different scale lengths.

Methods for imaging the underground velocity structures based on seismic ambient noise recordings are based upon the assumptions of a diffuse wavefield or energy equipartitioning. Under these conditions, a well-established theoretical background (e.g. Aki, 1957; ToksöZ and Lacoss, 1968; Lobkis and Weaver, 2001; Snieder, 2004; Larose et al., 2006; Wapenaar and Fokkema, 2006) states that the Green's functions (GFs) of surface wave propagation between two receivers can be estimated from the cross-correlation of ambient noise recorded at the two sites. The information about the GF can then be used to infer the dispersive characteristics of surface waves and, finally, the mechanical properties of the propagation medium underneath the two sensors.

Following these premises, over the past 15 years a number of studies derived images of the Earth's interior in different contexts and at different scales, using measurements of the Noise Correlation Functions (NCF) (e.g. Shapiro and Campillo, 2004; Campillo and Paul, 2003; Sabra et al., 2005a; Ritzwoller et al., 2011; Seats et al., 2012, and references therein).

Notwithstanding these numerous, successful applications, a still-pending question regards the reliability of GF's estimates via NCF when the wavefield is not perfectly isotropic and/or energy-equipartitioned. Within this general context, the present thesis aims at the quantitative investigation of the feasibility and reliability of the noise-based imaging methods, with particular reference to geothermal exploration, for which only few applications are reported (e.g. Calò et al., 2013; Lehujeur, 2013). The target of the study is the Larderello-Travale Geothermal Field (LTGF; Italy), whose internal

structure is well constrained through direct probing and geophysical exploration (e.g. Calcagnile and Panza, 1980; Batini et al., 1985; Vanorio et al., 2004; Bertini et al., 2006; Bertani et al., 2005; De Matteis et al., 2008), and which is presently the object of renewed exploration programs.

Data used for this study were gathered by a temporary seismic array (GAPSS - Geothermal Area Passive Seismic Sources), operated by the Italian Istituto Nazionale di Geofisica e Vulcanologia (INGV) throughout the May 2012-October 2013 timespan.

For this thesis I used noise recordings collected during the first eleven months of the experiment (May 2012 - March 2013). In that period, the array consisted of 13 seismic stations deployed over a 50 km X 50 km area, with average inter-station distance of $\sim$ 16 Km. The seismic recorders were equipped with either broadband (40s and 120s) or intermediate-period (5s), 3-components seismometers.

In order to quantify the directional properties of the SM wave-field, I first used a deterministic approach (namely: frequency-domain beam-forming (e.g Lacoss et al., 1969; Kennett et al., 2003)) that, under the common-waveform model, allows to estimate the slowness vectors of plane waves impinging at the array within short (10 minutes), subsequent time windows. Following these analyses, I demonstrated the non-homogeneous distribution of SM incoming directions, with persistent sources spanning 120-330°N directions. Moreover, I observed that SM records during summer-time periods are dominated by body-waves with dominant frequencies 0.1-0.3 Hz, hence constraining the feasibility of the stochastic techniques to frequencies > 0.3 Hz.

Subsequently, I applied to the entire dataset the stochastic techniques based on estimates of the noise correlation functions using both time-domain (NCF; e.g. Bensen et al. (2007)) and frequency-domain (modified-SPAC– Spatial Auto-Correlation; e.g. Ekström et al. (2009)) approaches. The NCF provided information about surface-waves group velocity, while modified-SPAC produced phase-velocity results. Once compared the results obtained from the two different methods, the feasibility criteria and quality control showed that the results produced by NCF are the most reliable and provide velocity models closer to those previously established ones for the study-area,

especially when accounting for the productive zones of the geothermal field.

This thesis is structured as follows:

- Chapter 1 introduces the microseism signals, describing their main spectral features and classification, with particular reference to the secondary microseims;
- Chapter 2 details the methods adopted for the deterministic analysis of the kinematic properties of the noise wave-field;
- Chapter 3 provides a formal introduction to the stochastic techniques (namely: NCF and SPAC) adopted to extract the Green's functions from seismic noise time- series, and it illustrates the methods for measuring both group- and phase velocities dispersion curves;
- in Chapter 4 I first present a geological and geophysical overview of the study-area, and then proceed to the description of the data-collection and archiving procedures. This chapter ends with the description of SM spectra, and their seasonal variability;
- Chapter 5 is dedicated to the SM wave-field characterization, as obtained from the application of the beamforming method (Chapter 2). The determination of the main incoming directions of microseisms and their apparent velocity allowed to highlight a frequency- and - seasonal dependence of several possible sources; these results are then compared to the previous knowledge about SM sources in the Mediterranean and adjoining areas;
- Chapter 6 presents the results derived from the application of the NCF and SPAC stochastic techniques. The possibility to retrieve reliable empirical GFs is discussed quantitatively, through signal-to-noise measurements and error analysis, and in light of the results of the deterministic method. Group and phase velocity dispersion curves, measured respectively from the NCF and the SPAC methods, are found to produce significantly different velocity models, whose validity is examined using the geological and geophysical data available for the study-region;

- in the conclusive part of the thesis, the overall results are summarized, and a discussion is reported about the reliability of the NCF and SPAC investigations in the specific geothermal area. Finally, future applications and further analyses are suggested.

Chapter 1

Microseisms

"Sì cogli uni che con gli altri [pendoli a grandi masse e pendoli leggerissimi] si ottengono oggi tracciati raramente rettilinei, ciò che mostra che il suolo, contrariamente a quanto una volta si credeva, non si trova mai in perfetta quiete. Siffatta perturbazione, quasi continua e più o meno accentuata, dei sensibilissimi sismografi, è stata chiamata agitazione microsismica e per brevità in seguito anche con la parola microsismi"

Agamennone (1932)

In this first chapter I illustrate a short excursus on the type of signal used on my analysis. I show what microseism are and how they are classified and identified among seismic time series, paying particular attention to the secondary microseims, that are the most energetic, and the object of my research.

The continuous seismic background vibrations, which are found in every seismic record worldwide, are known as seismic ambient noise. The seismic ambient noise is characterized by amplitudes ranging between 10^{-7} and 10^{-5} m/s in the frequency band 0.01-20 Hz (fig. 1.1); historically, it has been discarded as it was considered as a disturbance superimposed to the signals of interest, namely earthquakes or reflections/refractions. The first, pioneering study on seismic ambient noise dates back to Bertelli (Bertelli, 1872), who identified these neglected parts of ground motion and prompted

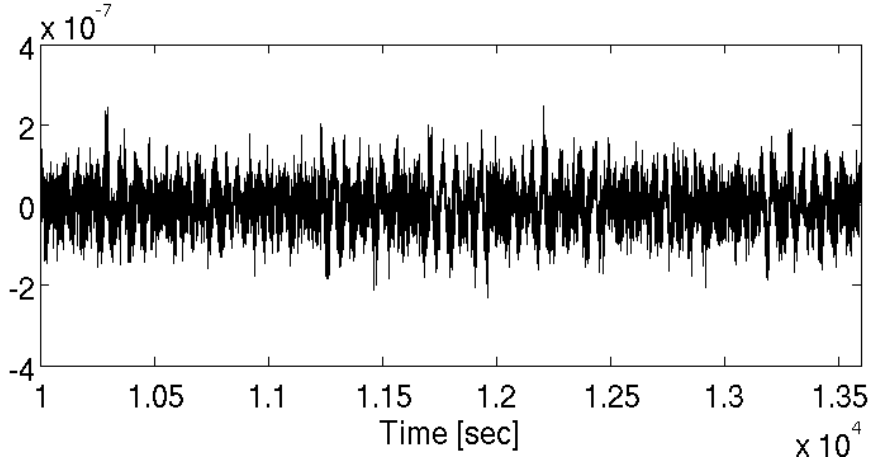

Figure 1.1: Example of seismic ambient noise waveform, recorded from a broad-band station in Larderello-Travale Geothermal Field (Tuscany, Italy), on 19/05/2012.

the subsequent investigations on their characterization and source location. The sources of seismic noise can be different and spatially spread, often acting contemporaneously and uncorrelated with each other. A part from the instrumental noise [1], it has been widely observed (e.g. Milne, 1883; Gutenberg, 1958; Asten, 1978; Asten and Henstridge, 1984) that natural sources mostly act at frequencies lower than 1 Hz; above this limit, sources are usually related to anthropic (cultural) sources. The vibrations at frequencies below 1 Hz are named *microseisms*. Numerous observations, conducted on both land and ocean bottom, showed that the main microseisms source is the ocean surface (e.g. Miche, 1944; Longuet-Higgins, 1950; Hasselmann, 1963; Cessaro, 1994; Webb, 1998). Microseisms are the result of different sources acting at the same time in different oceanic regions. Natural seismic noise sources other than Ocean surface, as for example rivers and volcanic tremors, generate higher frequency noise, overlapping the cultural band. The observation of the temporal variations of the seismic noise spectrum allows the recognition of the cultural frequencies from the natural ones. It is well known (e.g. Okada and Suto, 2003) that the cultural seismic noise amplitude

[1] The instrumental noise, called also self noise (the noise created by the equalizer, filter and amplifier circuitry), prevails at frequencies outside of the seismometer's performance bandwidth, where the signal is strongly attenuated.

spectrum oscillates with day-night succession, being lower during week-ends; on the other hand the microseism noise follows seasonal trends (e.g. Ebeling, 2012; Okada and Suto, 2003; Stutzmann et al., 2000, 2009), with major spectral amplitudes during winter and concomitantly with strong sea-storms. A historical overview on the early inspections of microseisms has been recently reported by Ebeling (2012). The study of location of microseisms' sources has been used for determination of remote wave-climate (e.g. Babcock et al., 1994; Bromirski, 2001) and reconstruction of sea states in the context of climate changes. Many scientists investigated quantitatively the relation between wave climate and microseism activity. For example, Bromirski et al. (1999) presented a study for California based on correlation between buoy and seismometer measurements, where they showed that elements of the wave climate can be accurately reconstructed using near-coastal inland broadband seismometer data. High correlations were found by Essen et al. (1999) between microseisms data recorded in Hamburg and ocean-wave fields modeled for the North Atlantic Ocean; they showed, also, that replacing ocean-wave height by wind speed in the correlations, it turned out that the correlation coefficients decrease by an amount between 4%and 20%, thus underlining the dependence of microseismic activity on ocean-wave oscillations. A strong potential of microseisms analysis is the advantage of the wide spreading of seismic stations and the availability of historical seismic data, that can integrate, and sometimes supply, the more sparse buoy data. A further study on a 40-year-long record of wintertime microseisms, by Grevemeyer et al. (2000) attempts an interesting reconstruction of the wave climate in the northeast Atlantic Ocean, comparing microseisms data with wave records and numerical wave model, that took into account the historical surface pressure and wind distribution data. Furthermore, polarization analysis and beamforming of recorded seismic ambient noise allowed to remotely follow -from California- the evolution of the Katrina hurricane storm waves in 2005 (Gerstoft et al., 2006a).

The energy of microseisms travels primarily as Rayleigh waves (e.g. Haubrich et al., 1963; Haubrich and McCamy, 1969; Lacoss et al., 1969; Roux et al., 2005; Tanimoto et al., 2006), within the sea-floor wave-guide, represented by

an increase in seismic velocities with depth (through the Ocean-crust-upper mantle) bounded above by a pressure release surface, that guarantees an efficient propagation of the acoustic energy generated at the surface. The generated surface waves can have many different velocities, but only those corresponding to the modes characteristic of the ocean sea-floor waveguide can propagate well abroad (Webb, 1992).

Love surface waves have been recognized in microseisms signals too, mostly at the lowest frequency band (e.g. Friedrich et al., 1998). Nishida et al. (2008) hypothesized a common origin with the Rayleigh waves, from their study on bore-hole array of tiltmeters' data in Japan. Lin et al. (2008) worked on a large-aperture seismic array in the West USA, and showed that Love waves emerged on the cross-correlations of the transverse components between most of the station pairs at frequencies higher than 0.05 Hz.

Also body waves have been found as ambient noise wave-field constituent, principally in the higher frequencies of the microseism band (> 0.16 Hz) (e.g. ToksöZ and Lacoss, 1968; Webb, 1998; Roux et al., 2005; Landès et al., 2010; Zhang et al., 2010; Koper et al., 2010; Hillers et al., 2013). Those seismic phases show longitudinally polarized particle motion and high apparent horizontal velocities, that are expression of teleseismic body-waves arrivals that follow the global weather pattern (e.g. Haubrich and McCamy, 1969; Schulte-Pelkum et al., 2004; Gerstoft et al., 2006a, 2008; Stehly et al., 2006; Landès et al., 2010; Ruigrok et al., 2011; Stutzmann et al., 2012).

The very long-period band (< 0.03 Hz) is controlled by infragravity waves (e.g. Webb, 1998). In the range 0.002-0.007 Hz, the Earth's continuous free oscillation is identified as *Earth's hum*; this hum is generated by the interaction between atmosphere, ocean and sea-bed probably through the conversion of storm energy to oceanic infragravity waves, that interact with ocean sea-floor (Rhie and Romanowicz, 2004; Webb, 2007).

It is well known that microseism spectra have two peaks, one at the frequency of the generating ocean waves, and the other at twice that frequency (e.g. Haubrich et al., 1963; Kibblewhite and Wu, 1991). These peaks are then identified as primary and secondary (or double-frequency) microseisms. The secondary microseism contains more energy, and the peak is between

0.13-0.2 Hz; on the other hand the weaker primary microseism has a peak between 0.05-0.08 Hz. These microseism peaks are evident in spectra from any site, even far from the coast; this close similarity is a consequence of the efficient propagation of Rayleigh waves at periods larger than few seconds (Webb, 1998). In figure 1.2 are shown some microseism spectra recorded by

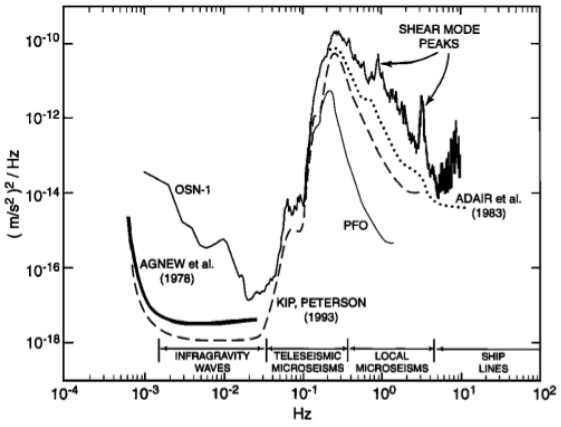

Figure 1.2: Examples of vertical acceleration microseism spectra recorded worldwide: from south of Hawaii (OSN-1), from Kipapa,Hawaii (Peterson, 1993), from a quiet site in California (PFO) and from the same site the long-period spectrum (Agnew and Berger, 1978). The more energetic peak is the secondary microseism peak at about 0.2 Hz. After Webb (1998).

vertical accelerometers in various sites in the world; the similarities between each other are clear, and the two microseism peaks are evident.

If the storms generating the swell are distant, the arrivals are more affected by dispersion in deep water. This results in a shifting of the wave spectral peak from low to high frequencies (Munk et al., 1959). Thanks to this dispersion effect, it is possible to determine the distance of the source and the origin time from the temporal evolution of the peak frequency (Haubrich et al., 1963).

The generating mechanisms of the microseisms have been largely explored;so far, it is well established that primary and secondary microseisms have different genesis (e.g. Cessaro, 1994; Friedrich et al., 1998; Stehly et al., 2006), which are described in the following subsections of this chapter.

1.1 Primary Microseisms (PM)

Within the seismic ambient noise spectrum, primary microseisms (PMs) are characterized by a moderate peak spanning the 0.05-0.08 Hz frequency band. PMs are thought to originate in the linear coupling of ocean waves energy into the sea floor; hence, PM have the same frequencies as the ocean gravity waves that produce them. PM originate in shallow-water, more likely on sloping sea-floor, where the amplitude of progressive waves does not decay exponentially with depth and the energy transmission to the seafloor occurs at the same frequency of the ocean waves (e.g. Friedrich et al., 1998; Haubrich et al., 1963; Hasselmann, 1963). PM have shown a seasonal variability (e.g. Stehly et al., 2006): for the Northern Hemisphere the sources are mainly located in the northern Oceans during winter, and southern Oceans during summer.

1.2 Secondary Microseisms (SM)

Secondary microseisms (SMs) are more energetic than primary ones. SMs energy is concentrated within the 0.13-0.2 Hz frequency band, and it dominates the spectra of both ocean bottom and continental sites. They are also called *double-frequency* microseisms because their peak frequency doubles the one of the ocean surface waves that generate them (e.g. Kibblewhite and Wu, 1991; Orcutt et al., 1993; Webb, 2007; Tanimoto, 2007).

It is known that the ocean waves spectrum peaks depends on the fetch [2] and the wind speed (e.g. Munk et al., 1959; Hasselmann, 1974). The ocean wave's height increases until the phase velocity equals that of the wind, and the spectrum of the ocean wave follows the evolution of that of the generating wind. As a consequence, the spectrum of the ocean surface gravity waves mantains a narrow band-width shape under increasing wind, evolving toward lower frequencies. Pierson and Moskowitz (Pierson and Moskowitz, 1964),

[2]The fetch is the effective width of the storm, and the waves that propagate out of this region no longer evolve. Inside this sea-surface area, the wind direction and intensity are considered constant. For basin scale wind fields, the fetch can equate the basin area (Webb, 1998).

showed the wave height spectrum for a fully developed sea, that Hasselmann completed for regions with limited fetch (Hasselmann et al., 1973). This response of the ocean waves to the wind velocities allows correlations with the excitation of microseisms. This model is characterized by an inverse power

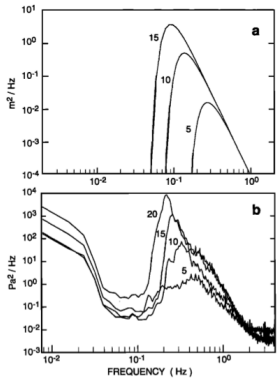

Figure 1.3: Up: the Pierson-Moskwitz Pierson and Moskowitz (1964) wave height spectrum for a fully developed sea under wind velocities of 5,10,15,20 m/s. Below: evolution of a seafloor pressure spectrum under a storm. The microseism peak frequency roughly doubles the wind wave spectrum peak. After Babcock et al. (1994).

law of the spectral amplitudes, that terminates abruptly at low frequencies, around the wind peak frequency, and at higher frequencies remains almost unchanged, saturated, for different wind speeds; this feature is also observed in the microseism spectrum, at frequencies that roughly double that of the ocean wave spectrum (see figure 1.3). As a consequence, double frequency peak varies rapidly in amplitude and frequency, being affected by seasonal variability as the primary one (e.g. Stutzmann et al., 2009, 2000; Aster and Bromirski, 2008). The generation mechanism of this type of seismic ambient noise has been first formally investigated by Miche (1944), then by Longuet-Higgins (1950) and Hasselmann (1963). It has been shown that ocean gravity waves of similar frequency and wavelength (i.e. similar wave-number) traveling in opposite directions, can interact in a non-linear sum, that doubles the frequencies of the waves and sums opposing wave-numbers into a nearly zero wave-number, i.e. producing an unattenuated high phase-velocity acoustic wave that can propagate efficiently to large depth below the water wave

base (the depth at which the ocean wave is able to move water) (e.g. Orcutt et al., 1993; Babcock et al., 1994). Such pressure variation couples with the sea-floor producing surface-waves, at a frequency which is the double of the original ocean gravity waves.

Let us consider a fluid defined as incompressible, irrotational and not having viscosity, with particle velocity $\mathbf{u} = \{u,\ w\}$, with u and w the horizontal and vertical components respectively. Then the Navier-Stokes' equation, that describes the motion, can be written as to the Bernoulli's equation (Longuet-Higgins, 1950; Kundu et al., 2012):

$$\frac{p - p_s}{\rho} - gz = \frac{\partial \Phi}{\partial t} - \frac{1}{2}(u^2 + w^2) + \theta(t) \tag{1.1}$$

where p represent the pressure term, p_s is the pressure at the free surface (constant), ρ is the fluid density, g is acceleration gravity and Φ is the potential of the velocity; $\theta(t)$ is the pressure variation in time, at a given depth. In deep water approximation Φ, u, w decrease esponentially as the water depth z increases (Longuet-Higgins, 1950); considering the total forces acting on an element volume of the fluid, it is derived that at the seafloor depth $z = h$ the equation 1.1 is (Kundu et al., 2012):

$$\frac{p_h - p_s}{\rho} - gh = \theta_h(t) = \frac{1}{\lambda}\frac{\partial^2}{\partial t^2}\int_0^\lambda \frac{1}{2}\xi(x,t)^2\, dx \tag{1.2}$$

where λ is the wavelength of the fluid, and $\xi(x,t)$ is the fluid surface elevation that fluctuates in space and time. Therefore, the term $\theta_h(t)$ is the pressure variation at the seafloor, that depends on a second-order function of the amplitude of the fluid waves $\xi(x,t)$.

If two ocean waves travel in opposite direction with the same frequency and wavelength but different amplitudes, a_1 and a_2 ($\xi(x,t) = a_1\cos(kx - \omega t) + a_2\cos(kx + \omega t)$), then the equation defining θ_h in 1.2 is

$$\theta_h(t) = -2a_1a_2\omega^2\cos(2\omega t) \tag{1.3}$$

In this special case, the pressure fluctuation is no more dependent on the

depth, but only on time. From equation 1.2:

$$\frac{p_h - p_s}{\rho} - gh = -2a_1 a_2 \omega^2 \cos(2\omega t) \tag{1.4}$$

The amplitude of the generated fluctuation, consequently transmitted to the seafloor, is proportional to the product of the amplitudes of the two colliding waves, a_1 and a_2, while the frequency is 2ω, twice the frequency of the ocean waves, thus justifying the *double frequency* peak of secondary microseisms, generated in this manner.

In the case of a single progressive fluid-wave, its amplitude will not decay exponentially with depth only in shallow water, for which the velocity field at the sea-floor is not null. In this situation, there is an energy transmission at the seafloor at the same frequency of the ocean waves, i.e. the primary microseims presented in section 1.1.

Bromirski et al. (2005) differentiated the SM into *low period double frequency* (LPDF) at about 0.16 Hz, and *short period double frequency* (SPDF) at about 0.2 Hz. These authors showed that the SPDF are related to wind-generated wave trains that do not propagate far away the storm, because of their frequency content.

Tanimoto (2007) studied the non-linear normal-mode excitation theory, and asserted that the secondary microseism peaks could be generated only in shallow (less than 3 Km depth) ocean/sea. When double frequency microseism peaks exist, a necessary condition is the existence in the source region of double frequency ocean wave spectra; comparing Californian microseism data with Pacific buoy spectra, he found that the aforementioned condition was satisfied only once accounting for sources close to coast, and shallow waters. Finally, Tanimoto (2007) showed the difficulty in precisely estimating the SM source excitation location. Nonetheless, the precise location and spectral evolution of microseisms' sources represent an active area of research.

Stable sources of SM have been recognized by means of array analysis and comparison with sea-state data (both observed and modeled (e.g. Friedrich et al., 1998; Essen et al., 1999; Chevrot et al., 2007; Ardhuin et al., 2011)).

The stability of the sources, apart from storm activity, is linked to the generating mechanism, where the importance of the coast and bathimetry has to be considered (e.g. Essen et al., 2003; Schulte-Pelkum et al., 2004; Bromirski et al., 2005; Gerstoft and Tanimoto, 2007; Traer et al., 2008). Furthermore, in the works of Bromirski and Duennebier (2002) and Chevrot et al. (2007) SM production areas have been found preferentially in steep coasts, where the swell hits at close-to-normal incidence.

Actually, the non-linear interaction of ocean waves, could occur in three different environmental sea-states (Longuet-Higgins, 1950; Ardhuin et al., 2011, 2012; Gualtieri et al., 2013). The first class acts within a storm with a wide angular distribution, with ocean waves coming from many different directions; this class is related to double-frequency peaks, at high frequencies, $\geq$ 0.5 Hz. The second class involves generating areas close to the coasts, where incident waves from a storm collide with the waves reflected at the coast.In the third class, an interaction between waves generated by different storms occurs, even if the storms are far away; this is the case in which the most energetic SM are produced. In figure 1.4 there is a scheme of these three classes (after Ardhuin et al. (2012)). Ardhuin et al. (2011) proposed the first comprehensive numerical model of microseismic generation by random ocean waves. This numerical model contradicts the exclusivity of shallow water SM sources supported by Tanimoto (2007). Ardhuin et al. (2012) showed that Rayleigh waves could be occasionally generated even in deep water, occurring at the same time as the largest outliers in the correlation of wave heights and seismic noise levels. Evidences of deep water SM sources have been found in works that used seismic array methods, as triangulation of propagation azimuths, derived from f-k analysis of SM approaching three different arrays in Alaska, Montana and Norway (Cessaro, 1994). Other studies used frequency-slowness analysis of array data, polarization and amplitude analysis at individual stations for locating SM in western Europe (Chevrot et al., 2007). Kedar et al. (2008) explored the correspondence between observed and modeled SM for North America, Greenland and Iceland, succeeding in the prediction of generated SM in deep ocean, also considering the importance of strong storms, topographic effects on wind patterns and

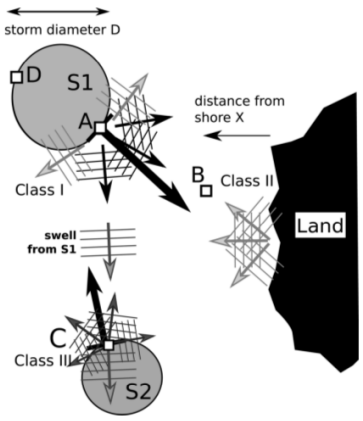

Figure 1.4: Scheme of the three classes of double frequency micrseisms generating sea-state. Thick arrows are the local wind directions and the small arrows are the wave trains. At point A, the storm contains energy in opposite wave-trains, even at angles greater than 90° from the wind direction (class 1). At point B, there is the interaction between incident and reflected wave-trains (class2). At point C, the swells from the storm S1 collide with the local wind-driven waves generated by the storm S2 (class 3). After Ardhuin et al. (2012).

local bathymetry. Obrebski et al. (2012) found deep ocean SM sources, using ambient noise polarization analysis applied to data recorded at several stations around Eastern Pacific Ocean; then they triangulated the resluting back-azimuths to constrain source location, then compared with numerical model.

All the aforementioned studies highlight the complexity of the SM generation mechanism, and evidence the difficulty in assessing precise and univocal location of SM sources.

Chapter 2

Array Methods for Locating Secondary Microseism sources

This chapter presents the array methods that I used for locating the secondary microseism sources. The study of microseism incoming directions, and the location of their sources (where it is possible), must be considered mandatory for the extraction of Greeen's Functions from the ambient noise signals, as it will be detailed in the next chapter (3).

Techniques that exploit the seismic ambient noise for imaging of the Earth's interior (see chapter 3) are based upon the assumption of a stochastic noise wavefield which is stationary in time and space.

Due to its nature, however, the SM wavefield is only approximatively diffusive, depending on the frequency range of interest, the scattering properties of the medium, the distance and number of the active sources. Any attempt of Green's Function retrieval using a stochastic approach must therefore be preceded by a spectral characterization of the SM and a statistical analysis about the location of its sources. These steps, in fact, allow the identification of the minimum time span for which the aforementioned hypotheses of homogeneity and stationarity are respected.

By the same token, the time-frequency variability of SM is clearly reflected by their spectrograms. The spectrogram is composed by a concatenation of

power-spectral densities evaluated over subsequent time windows; from this representation, it is possible to determine the microseism spectral features, and to relate them to storms' evolution, the distance between storms and microseisms source areas, the microseisms origin time.

These techniques are heavily influenced by the seismic array location and they do not allow for separating the contribution of the source from propagation effects. This is the reason why, for an univocal identification of SM sources, it is needed an integration with sea-state data.

The following sections present a more detailed introduction to the beamforming technique and to the spectrogram analysis.

2.1 Array Beamforming

For a stationary random process, the frequency-wavenumber ($\omega - \mathbf{k}$, with ω angular frequency) power spectral density function provides information about the power of the incoming waves as a function of frequency and wavenumber (Capon, 1969). In this thesis, the horizontal slowness ($\mathbf{p}$, reciprocal of apparent velocity) has been used instead of the wavenumber, as it provides a direct information about the phase velocity at a given frequency. The relationship relating the slowness to the wavenumber is $\mathbf{k} = \mathbf{p}\omega$.

The beamforming technique is substantially based on the frequency-slowness analysis for a plane-wave model. If a plane wave, defined by its slowness $\mathbf{p}$, crosses an array composed by N receivers, the time-shifts (phase delays) between the signals recorded by individual channels will depend on the velocity vector of the incoming wave, and the position vector of the different sensors. Considering only the two horizontal components of the slowness, (i.e. neglecting sensors' elevation), one can perform a grid search over the slowness plane looking for that slowness that best fits the observed phase delays (e.g. Kennett et al., 2003; Landès et al., 2010).

For a plane-wave propagating with slowness $\mathbf{s}$, the theoretical array beam power at the generic trial slowness $\mathbf{p}$ is thus defined as:

$$S(\mathbf{p}, \mathbf{s}, \omega) = \left| \frac{1}{\sqrt{N}} \sum_{j=1}^{N} exp\{i\omega(\Delta\mathbf{s} \cdot \mathbf{x_j})\} \right|^2 \tag{2.1}$$

where $\Delta\mathbf{s}$ is $\mathbf{p} - \mathbf{s}$, and $\mathbf{x_j}$ is the position vector of the j-th sensor with respect to a reference point. $S(\mathbf{p}, \mathbf{s}, \omega)$ attains a maximum when $\mathbf{s} = \mathbf{p}$.

Often eq. 2.1 is simplified by considering a vertically-inciding plane wave (with both components of $\mathbf{s}$ equal to zero), thus obtaining the so-called *Beam-Pattern*:

$$R(\omega, \mathbf{p}) = \left| \frac{1}{\sqrt{N}} \sum_{j=1}^{N} exp\{i\omega\mathbf{p} \cdot \mathbf{x_j}\} \right|^2 \tag{2.2}$$

For a given frequency ω and array geometry, the beam-pattern gives information about the resolution of slowness estimates and the possible presence of secondary peaks associated with spatial aliasing effects.

Step and size of the slowness grid, the frequency band and the length of the time-windows are key factors influencing the beamforming performances. If a too fine slowness grid is chosen, a waste of computing resources will occur. If the slowness space is too large, aliasing effects might contaminate the final result. Spatial aliasing effects arise when the mean inter-station distance is of the same order of magnitude of the dominant signal's wavelength, and it manifests as multiple secondary lobes in the power spectral estimates, making ambiguous the determination of the correct slowness vector. As a general rule, a given array geometry is appropriate for analysing signals over a particular frequency when the corresponding beam-pattern does not exhibit aliased peaks and the main lobe is fairly circular.

In figure 2.1 there are two examples of beam-patterns (fig.s 2.1c,2.1d), obtained at the frequency of 0.2 Hz, for two array geometries, different for the number of sensors and arrangement (fig.s 2.1a, 2.1b). A general law is that the grid step should be given by the size of the central lobe of the beam-pattern plot. The size of the central lobe (in s/Km), at a frequency f, is controlled by the inverse of the maximum aperture of the array (in Km) divided by f. On the other hand, two limitations have to be considered once

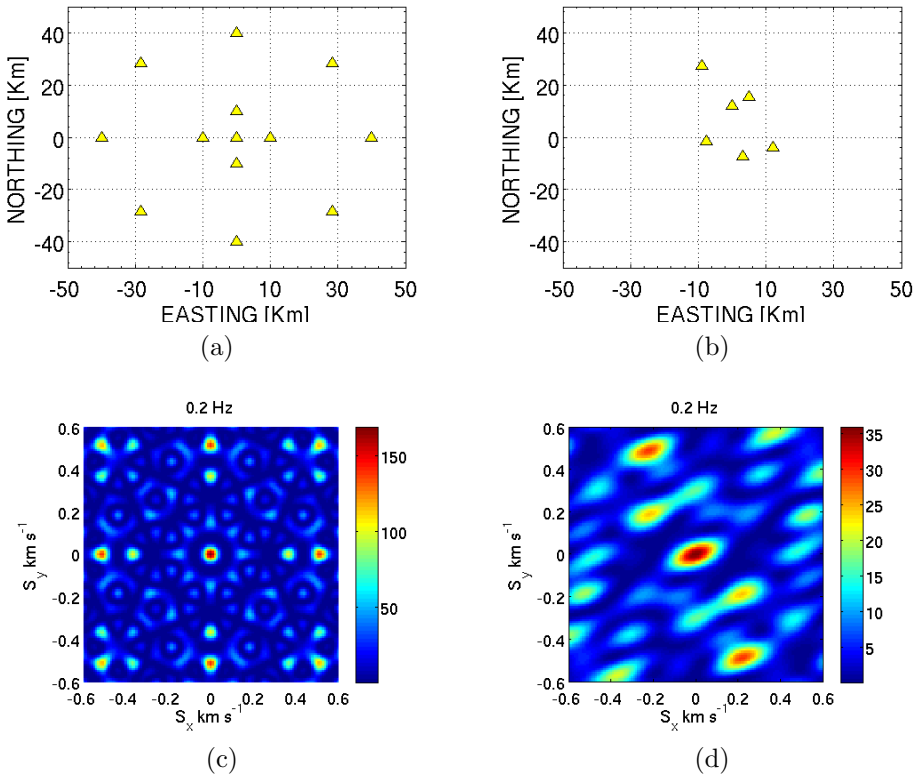

Figure 2.1: Examples of 2 simulations of array configurations (top) and their respective beam-pattern computed at 0.2 Hz (bottom). (*left*) In 2.1a a densely and homogeneous array configuration is presented; the beam-pattern (2.1c) has a very sharp (radius of about $0.1s/Km$) main circular lobe and the first alias is at $0.55s/Km$: this means that the array at 0.2 Hz can resolve plane waves colliding the array at any azimuth, with a precision of $0.1s/Km$ in slowness. (*right*) In 2.1b the array is more sparse and with fewer elements not uniformely deployed; the resulting beam-pattern, in 2.1d, is strongly aliased and the main lobe is large and non-circular (the minimum radius is about $0.12s/Km$ and the maximum radius is about $0.18s/Km$), meaning that a better sampling in the slowness space is in the NW-SE direction, where the stations have been more densely deployed.

deciding the size of the slowness grid. The first, is dictated by the minimum expected wave speed; The second, is related to aliasing side lobes in the beam-pattern, as discussed above. The general law for choosing a good slowness-grid-size is to evaluate it from the ratio between the inverse of the minimum inter-sensors distance and f (e.g. Lacoss et al., 1969).

2.1.1 Inversion in The Polar Formulation

In this thesis, I conducted beamforming analysys using a polar formulation (e.g., (Abrahamson and Bolt, 1987; Maresca et al., 2006)). In this formulation, the array response depends on the propagation azimuth θ_s, on the modulus of s, and on the distance of the j-th sensor from a reference point (d_j), as:

$$A_j(\theta_s, s, \omega) = \frac{1}{\sqrt{N}} exp\{i\omega(d_j)\ s\ cos(\theta_s - \theta_j)\} \tag{2.3}$$

Where θ_j is the azimuth of the vector connecting the j-th sensor to the reference point of the array.

In order to perform the inversion, i.e. to find the slowness vector best fitting the inter-station phase shifts, the frequency-smoothed cross-spectral matrix is first computed:

$$C_{j,k}(\omega) = \sum_{m=-NF}^{NF} a_m \hat{Y}_j^L \left(\omega + \frac{2\pi m}{L}\right) \hat{Y}_k^{L*} \left(\omega + \frac{2\pi m}{L}\right) \tag{2.4}$$

Where NF is the number of discrete smoothing frequencies, a_m are the weights used in the smoothing procedure, $\hat{Y}_j^L$ are the Fourier transforms of the normalized time series of length L, and the $*$ indicates the complex conjugate.

The beam-power is then expressed as:

$$M(\theta_s, s, \omega) = \frac{1}{N} \mathbf{A}^T(\theta_s, s, \omega) \mathbf{C}(\omega) \mathbf{A}(\theta_s, s, \omega) \tag{2.5}$$

For a given frequency ω, the coordinates of the peak value of M are the

solutions of the problem, providing the propagation direction θ_s^{MAX} and the velocity (reciprocal of s^{MAX}) of the plane wave impinging at the array.

2.2 Spectrogram Analysis

The spectral features of microseisms are the expression of the spectral characteristics of the storms that generate them. If several storms are active at the same time, their different power spectral evolution in time (as the generating surface winds develop, arise, move and dissipate) can be followed in the microseism spectrogram. Furthermore, it is possible to recognize separately all the active storms and their time history from the microseism spectrogram, if there is no storm more powerful that obscurates the specral signature of the others (e.g. ToksöZ and Lacoss, 1968; Lacoss et al., 1969; Capon, 1972; Cessaro, 1994). However, as observed by Chevrot et al. (2007), most of the times the temporal evolution of the dominant frequency in the spectrogam is not clear, and the most robust beamforming is preferred.

When the dominant frequency of SM changes in time, it can be explained by the dispersion of the sea-waves generated by distant storms (e.g. Haubrich et al., 1963). The water waves are dispersive, and this feature is:

$$\omega = \sqrt{g\, k \tanh(k\mathrm{H})}$$

where g is the gravity acceleration, k the wavenumber, and H is the depth of the water column. If the water depth is much smaller than the wavelength, than shallow water approximation holds, and no dispersion occurs ($c = \sqrt{gH}$) since $tanh(kH) \approx kH$. On the other hand, in the deep water case (i.e., when H is greater than 1/3 the wavelength), then the term $tanh(kH)$ is approximated with 1, and dispersion occurs ($c = \sqrt{g/k}$). Consequently, high-frequency waves propagate slower than low-frequency ones.

Considering that the group velocity of sea-waves is half of their phase velocity, then group velocity is linearly related to frequency by the expression:

$$U = \frac{r}{t} = \frac{g}{4\pi f} \Rightarrow f = t\frac{g}{4\pi r} \tag{2.6}$$

where r is the travelled distance from the storm, t the time variable, and f the frequency.

Considering a specular evolution even the microseisms, in the frequency-time plot of a spectrogram, when it is possible to recognize a linear trend in the microseism peak frequency, the intercept in time represents the origin time of the storm, and the slope varies inversely with the distance r between the storm and the microseism generating area.

Usually the information retrieved with this method are crossed with metereological data (surface pressure maps, maps of the ocean storms, sea-state spectra), and beamforming incoming direction results, in order to provide more robust estimates.

Chapter 3

Extraction of the Green's Functions from Microseism signals

In this chapter I introduce the techniques specifically designed for extracting the Green's Functions from the correlation functions of a diffuse wave-field. After presenting the assumptions and limitations of these methods, I proceed with describing the two algorithms (namely: Time-Domain Noise Correlation Function (NCF) and Spatial Auto-Correlation (SPAC)) that I used in this thesis.

For a pair of arbitrary points in a given propagation medium, the Green's function (GF) in between the two points represents the signal one would observe at one of the two sites once a point, impulsive source acts at the other site. In other words, for a given source-observer pair, the GF is the causal solution of the wave equation when the source is a Dirac impulse in both time and space. It has been demonstrated, both theoretically and experimentally, that it is possible to retrieve the Green's function between two receivers by cross-correlating passively recorded diffuse and uncorrelated wave-field (such as noise) without the use of controlled sources (e.g. Lobkis and Weaver, 2001; Larose et al., 2004; Wapenaar and Fokkema, 2006; Shapiro

et al., 2005; Sánchez-Sesma and Campillo, 2006). The principle is that the cross-correlation of a diffuse, uncorrelated wave-field only maintains the coherent signal traveling from one receiver to the other, and it corresponds to the impulse response of the medium for a delta-like source acting at one of the two sites. Since seismic observations are normally conducted at or close to the Earth's surface, the noise correlation functions are generally dominated by surface waves. The GFs, thus derived, can then be used to estimate group and phase velocity dispersion curves, whose inversion allows to constrain the average elastic properties of the medium beneath the two sensors used for correlation estimates.

3.1 State of the art

Aki (1957); ToksöZ and Lacoss (1968); Claerbout (1968) were the first to attempt the reconstruction of the GF from the diffuse noise field, till then considered as a disturbance. Similar efforts have been attempted in different fields of physics, such as ultrasonics (e.g. Lobkis and Weaver, 2001; Weaver and Lobkis, 2001), acoustics (e.g Roux et al., 2003, 2004a; Sabra et al., 2005c), electromagnetism (e.g. Slob and Wapenaar, 2007), Earth seismology (e.g. Weaver and Lobkis, 2005; Campillo and Paul, 2003; Sabra et al., 2005a), helioseismology (Duvall et al., 1993; Rickett and Claerbout, 1999), Lunar seismology (Larose et al., 2005). About this topic, an overview of the state of art is found in the work by Wapenaar et al. (2008), with a major attention to seismic exploration applications.

A diffuse wave-field implies that the wave-field consists of waves characterized by all the possible polarizations and propagation directions, with equal weight in average. If one considers a wave-field propagating in a finite elastic body, it can be represented as a sum of all the possible modes:

$$u(\mathbf{x},t) = \sum_n \mathrm{a}_n \Psi_n(\mathbf{x}) \exp i\omega_n t \tag{3.1}$$

where the Ψ_n are the eigenfunctions (i.e. the real orthonormal mode

shapes), ω_n are the eigen-frequencies and a_n are the complex modal amplitudes that only depend on the source. The different vibrational modes result from a perturbation applied to the reference elastic model. After a sufficient time (greater than the *break time* $\Delta T = 1/\Delta\omega$, i.e. the characteristic frequency difference between modes), the field becomes equipartitioned, diffuse, and the a_n coefficients become random functions of time (e.g Paul et al., 2005; Larose et al., 2006). The equipartition means that, in the phase space, the energy is distributed homogeneously in average among all the possible modes vibrations.

The equipartition causes the amplitudes of the different modes to be random and uncorrelated, so that the cross-spectral energy density $F(\omega)$ of two different modes, in a narrow frequency band $[\omega + \delta\omega, \omega - \delta\omega]$, is zero: $\langle a_n a_m^* \rangle = \delta_{nm} F(\omega_n)$, where the brackets represent the time/frequency average and δ_{nm} is the Kronecker delta (Lobkis and Weaver, 2001; Paul et al., 2005). If one considers a series of sources randomly distributed in space, the average is performed in space and the coefficients a_n are function of the location of the sources. Considering two locations, x and y, the averaged correlation between the wave-fields observed in x and y is:

$$\langle u(x,t)u(y,t+\tau)\rangle = \langle C(x,y,\tau)\rangle = \frac{1}{2}\Re\sum_n F(\omega_n)\Psi_n(x)\Psi_n(y)\exp i\omega_n\tau \quad (3.2)$$

where Ψ_n are the eigenfunctions, and $\Re$ stands for the *real part of*.

If F is constant, the equation in 3.2 is similar to the time derivative of $G_{x,y}$, i.e. the GF describing the propagation between x and y:

$$G_{xy}(\tau) = \textstyle\sum_n \Psi_n(x)\Psi_n(y)\frac{\sin(\omega_n\tau)}{\omega_n} \quad \text{for } \tau > 0 \quad (3.3)$$

The equation 3.2 differs from equation in 3.3 for i) having a factor $F/2$ modifying the spectrum, and for ii) the fact that the correlation supports negative times τ.

The first authors to present detailed arguments, supporting the equivalence between the correlation of a diffuse wave-field and the GF of the medium, are Lobkis and Weaver (2001) who also performed ultrasonic tests to confirm their findings.

What Lobkis and Weaver (2001) observed is that at least the arrival times of the direct Rayleigh wave and a reflected P-wave have been detected from the correlation method, confirming that the GF is present in the correlations of a diffuse field. However, Lobkis and Weaver (2001) considered the deconvolution for the source function in their experiment, so information about the source is needed.

Derode et al. (2003) studied the GF recovering from the correlations of ultrasonic wave-field in an open scattering medium; in the case of a closed cavity, they found the same result as Lobkis and Weaver (2001), but when applying absorbing boundary condition, the argument remains valid providing that several distributed sources are used instead of a single point one.

With the *mirror-experiment* Derode et al. (2003) showed how to recover GF from correlation of a diffuse wave-field in a open medium without invoking a source deconvolution, but provided that the sources are distributed almost homogeneously in the medium, thus to constitute a perfect time-reversal device. Similar results have been demonstrated for a volume-averaging of the source (e.g. Roux et al., 2004b).

The equipartition requirement could not be valid for the surface waves, because the fundamental Love and Rayleigh wave modes usually carry more energy than the sum of all higher modes. After these considerations, Snieder (2004) presented an alternative derivation of GF from correlations no more based on normal modes. In his demonstration, the energy equipartition among the modes is substituted by the requirement that scattered waves propagate on average isotropically near the receivers, implying that the net energy flux of the scattered waves is small. Since the scatterers act as secondary sources, he demonstrated that the main contribution to the wave-field at two receivers comes from scatterers located close to the line connecting

the receivers, after averaging over time, and possibly over different source events, under the stationary phase approximation.

The acoustic and elastodynamic representations of GF in terms of cross-correlations of wave- fields recorded at two receivers has been exactly derived by Wapenaar and Fokkema (2006) and Wapenaar (2006), for a lossless arbitrary inhomogeneous medium without the diffusivity assumption. Wapenaar (2006) considered a one-sided illumination for a inhomogeneous medium. In this case, the inhomogeneous medium acts as a mirror, with complex phase behavior, for the sources (all located continuously along an arbitrary open surface); all the energy emitted by these sources are eventually reflected by the complex mirror, thus compensating for the absence of sources from other directions. This conclusion could be interesting for seismological applications, where the sources are not uniformly distributed neither in the volume nor on a closed surface. But also aspects that may limit the accuracy of the retrieved GF in practice have been highlighted: 1) an-elastic losses, 2) finite source distribution on a surface, 3) finite recording times, 4) mutual correlation and irregular source distribution.

More generalized situations, and theoretical results have been demonstrated i) for cases in which the sources of the wave-field were arbitrarily distributed on a surface of lossless fluid (e.g. Godin, 2006), ii) for attenuating, inhomogeneous and moving media (e.g. Godin, 2010).

An unified representation of Green's functions in terms of cross correlations, proposed as summary general demonstration has been proposed in the complex work of Wapenaar et al. (2006). They demonstrated the validity of the method for applications to diffusion phenomena, acoustic waves in flowing attenuating media, electromagnetic diffusion and wave phenomena, elastodynamic waves in anisotropic solids and electrokinetic waves in poroelastic or piezoelectric media.

Summarizing, the necessary condition of a diffusive wave-field is expressed, in the case of elastic waves, by the energy equipartition of the different component of the elastic wave-field (e.g. Sánchez-Sesma and Campillo, 2006; Sánchez-Sesma et al., 2008; Gouedard et al., 2008). This condition is achieved, in real seismological cases (e.g. Campillo, 2006; Larose et al., 2006), when

either temporal or spatial averaging produces a randomization of the wave-field, thus accounting for the contribution of: 1) random spatial distribution of noise sources and/or by 2) multiple scattering phenomena occurring in heterogeneous media.

In evaluating the amount of averaging necessary for the GF to emerge in the cross- correlation, a theoretical estimate can be made if the sources are random and uniformly distributed and/or in the case of equipartitioned waves. In these cases, the convergence follows the square root of the length of the data window used for computing the averaged cross- correlation functions; the signal-to-noise ratio (SNR) of these latter ones is the quantitative estimate of the convergence (e.g. Larose et al., 2004; Sabra et al., 2005c).

In passive seismology, experiments with cross-correlation methods have been conducted using either earthquakes' coda and seismic ambient noise.

Among the two types of signal, seismic noise presents anyhow the net advantage that it can be recorded continuously in any location. However, it has been noted that the ambient noise technique is sensitive to the azimuthal distribution of sources and to their distance from the recording stations (e.g. Pedersen and Krüger, 2007).
In subsequent studies, numerical simulations with smooth distribution of noise sources (Yang and Ritzwoller, 2008), and comparison between dispersion curves estimated from noise cross-correlation and earthquake data (Bao et al., 2014), showed that the non-homogeneity distribution of the noise sources is not an obstacle for the Green's function (GF) retrieval, if 1) the SNR, in the noise cross-correlation functions, is sufficiently high, and 2) the correlation functions are averaged over long time spans. Nonetheless, the inhomogeneity of noise sources could still affect the measurements for station-pairs whose separation is small once compared to the dominant wavelengths, because for those scales the first Fresnel zone is broader and the noise wave-field is likely to be less diffuse; under that circumstance, averaging over even longer time intervals is required (Yao and Van Der Hilst, 2009).

In parallel to the above studies, over the past ten years numerous researches addressed the extraction of the GF and the subsequent estimation

of the surface waves dispersion curves from the correlation of seismic ambient noise.

Shapiro and Campillo (2004) cross-correlated noise in the lower microseism frequency band (< 0.1 Hz) for a sparse network of broadband stations in the USA, then recovering the fundamental-mode dispersion curve of Rayleigh wave and opening the way toward seismic ambient noise tomography.
In a subsequent work, Shapiro et al. (2005) cross-correlated long sequences of seismic ambient noise both in the primary and secondary microseism frequency band to derive maps of the Rayleigh-waves group velocities which allowed imaging the crustal structure beneath California down to depths of about 20 Km.

Other results for California using the microseism frequency band $0.05-0.2$ Hz are those by Gerstoft et al. (2006b), Zhang and Gerstoft (2014), Ma et al. (2008), and Sabra et al. (2005b). In particular, this latter work outlined the importance of the station-pair orientation when the noise sources are directional, as it is the case for California where secondary microseism sources are mostly aligned along the coast line.

The method has been further applied to a variety of geological/geographical contexts and scales, including the deep structure of the Yellowstone caldera (Stachnik et al., 2008; Seats et al., 2012), the Cascadia subduction zone (Calkins et al., 2011), the northern Baltic Shield (Poli et al., 2012), the South-East Tibet (Yao et al., 2006, 2008), Southern China (Zhou et al., 2012; Bao et al., 2014), the Canterbury Plains in New Zealand (Savage et al., 2013), the Soultz-sous-Forêts geothermal basin (Calò et al., 2013), the near-surface Vahall oil field in Norway (Mordret et al., 2013), Central Europe (Verbeke et al., 2012) and the Italian peninsula (Li et al., 2010).

The time-domain Green's Functions (GFs) obtained from the Noise Correlation Function (NCF) are usually dominated by Rayleigh waves, as the latter ones represent the main component of the seismic ambient noise (see chapter 1). Subsequent time-frequency processing of the GFs yields esti-

mates of the group velocities; phase velocities are less considered, since the emergence of the initial phase in the NCF is not fully understood.

Information about the phase velocities can be achieved with a different approach, that is based upon a formal relationship between phase velocities and frequency-domain correlation coefficients. This latter method, named Spatial Auto-Correlation technique (SPAC), was originally formulated by Aki (1957), and further developed / modified in a plethora of subsequent studies (e.g. Asten, 2006; Chávez-García et al., 2005; Ekström et al., 2009).

In this thesis I adopted both NCF and SPAC methods, whose algorithms and assumptions are detailed in the following sections 3.2 and 3.3.

3.2 Time-Domain Noise Cross-Correlation Function (NCF) technique

For evaluating the broad-band cross-correlation functions (NCF) of ambient noise and subsequent group velocity dispersion curve, I followed the procedures suggested by Bensen et al. (2007). The calculation is subdivided into 4 steps: 1) single station data preparation (pre- processing), 2) cross-correlation and temporal stacking, 3) measurements of group velocity dispersion curves (GVDC), 4) quality control.

3.2.1 Noise Data pre-processing

In a preliminary phase, data from each station are de-meaned, de-trended, corrected for the instrument response and band-pass filtered in the frequency band of interest (in the case of this work, in the secondary microseism band $0.1 - 1$ Hz). Usually this pre-processing is conducted over daily time-series. The next step consists in removing, from the ambient noise records, the signals of earthquakes, non-stationary noise and instrument disturbances which could bias significantly the estimate of the NCFs. This procedure has to be data-adaptive, since the signals that one wants to remove occur randomly. Among the different techniques accomplishing this goal, a popular one is the

one-bit normalization, that preserves only the sign of the waveform (Larose et al., 2004; Shapiro et al., 2006). After several tests, however, I decided to adopt a different procedure, namely the running- absolute-mean (RAM) normalization as described in Bensen et al. (2007). The RAM normalization computes the running-average of the absolute value of the time series d_j within subsequent time windows of fixed length, and weight the waveform at the center of the window by the inverse of the average.
Let the length of the normalization window be $L = 2N + 1$, corresponding to the half of the maximum period of the pass-band filter (Bensen et al., 2007); then, the normalization weight for the generic $n - th$ time sample is:

$$w_n = \frac{1}{2N+1} \sum_{j=n-N}^{n+N} |d_j| \tag{3.4}$$

The normalized signal at the $n - th$ time sample is thus $\widetilde{d}_n = d_n/w_n$. The width L of the normalization window represents the amount of the amplitude information that the user wants to preserve. If it is set to $L = 1$, then the RAM will be equivalent to the one-bit normalization.

After time-domain normalization, spectral normalization (whitening) is applied. The spectral normalization is aimed at equalize individual frequencies thus producing a broad-band signal. Whitening consists of weighting the complex spectrum by a smoothed version of the amplitude spectrum, thus broadening the band of ambient noise and contrasting the effects of possible persistent monochromatic sources.

3.2.2 Cross-correlation and Temporal Stacking

Once the noise waveforms are pre-processed, the next step of the NCF technique consists in cross-correlating all the available $n(n-1)/2$ pairs of stations, where n is the number of stations. This process is extended over the entire observational time span. The cross-correlations are performed over non-overlapping time windows, whose length must be longer than the expected travel-times for surface waves propagating from one site to the other.

For this work, I adopted a window length of 600 seconds. Cross-correlations are computed in the frequency domain, through multiplication of the complex spectrum of one station by the conjugate spectrum of the other station of the pair. Then, the resulting spectrum is transformed back to the time domain.

Individual cross-correlations are then stacked on a daily base, and further stacked over the entire observational period.

The result is a two sided time-series, defined for both positive *causal* and negative *acausal* time lags. These two portions represent the waves that propagate from station A to station B or vice-versa; if the wave-field is diffuse (as theory would require) the two NCF segments should be symmetric. Actually, an asymmetry in the amplitude and frequency content is often observed.

The stacking procedure increases the SNR of the NCFs: the longer the length of the stacking period, the higher the SNR.

The Signal-to-noise ratio (SNR) of the NCF is measured to quantify the emergence of the Green's functions and to evaluate errors in the subsequent estimates of the group velocity dispersion curves (GVDC). For this work, I referred to Sabra et al. (2005a) definition of SNR, which is computed by dividing the maximum amplitude of the envelope of the NCF, in a 50 seconds window centered around the main arrival, by the root-mean-square (RMS) of the noise time window of equal length trailing the end of the NCF. The trailing noise is preferred instead of the leading one, because the former is less signal-dependent than the latter one (Bensen et al., 2007; Garus and Wegler, 2011). The SNR of the GFs is proportional to the square root of the stacking time. This fact has been demonstrated experimentally (Roux et al., 2004a; Sabra et al., 2005a; Gerstoft et al., 2006b; Garus and Wegler, 2011), numerically (Larose et al., 2006), and through theoretical analysis (Snieder, 2004). The SNR value is also a measure of the reliability of the subsequent dispersion measurements. Therefore, the computation of the SNR as a function of frequency is useful to quantify the emergence of the GFs in different frequency bands. The value of the SNR for different frequency bands is called *spectral SNR*, and it is computed by first applying narrow band-pass

filters to the stacked NCFs and then computing the SNR for each band-pass filtered correlation functions.

3.2.3 Measurements of Group-Velocity Dispersion Curves

The time-stacked NCF represents an estimate of the GF, which is then used to measure the group velocity dispersion curve (GVDC) for each station-pair. This task is accomplished through frequency-time analysis (FTAN) (e.g. Dziewonski et al., 1969; Levshin et al., 1992; Levshin and Ritzwoller, 2001; Bensen et al., 2007).

In the implementation of FTAN, the first step consists in the compression of the two sides of stacked NCF, i.e. in the averaging of the causal and acausal parts to produce a one- sided signal which is referred to as the *symmetric* signal.

In the second step, the analytic signal $w_a(t)$, of the one-sided NCFs $w(t)$, is calculated as follows:

$$w_a(t) = w(t) + iH(t) = |A(t)|e^{i\phi(t)} \tag{3.5}$$

where $H(t)$ indicates the Hilbert transform of $w(t)$.

The third step consists in transforming the $w_a(t)$ into the frequency domain, and band-pass filtering using narrow Gaussian filters spanning the whole frequency band of interest ($0.1 - 1$ Hz in the present case). For a reference frequency ω_0, the corresponding Gaussian filter has the form (Dziewonski et al., 1969):

$$G(\omega) = \exp\left\{-\alpha\left(\frac{\omega - \omega_0}{\omega_0}\right)^2\right\} \tag{3.6}$$

The parameter α controls the width of the filter, and it is commonly selected as a function of the inter-station distance (Levshin, 1989).

After inverse transformation back to the time-domain, the set of narrow-

bandpassed analytic signals allows deriving the 2-D envelope function as a function of time and frequency: $A(t, \omega_0) = |w_a(t, \omega_0)|^2$. For each frequency, the maxima of that function occur at the arrival time $\tau(\omega_0)$ of the monochromatic wave-packet, from which an estimate of the group velocity is obtained as $U(\omega_0) = r/\tau(\omega_0)$, where r is the inter-station distance.

3.2.4 Quality Control and Selection Criteria

The inter-station distance is the key-factor conditioning the frequency range where the dispersion of surface wave can be correctly measured. Given a frequency f, when the inter-station distance r is less than 2 (e.g. Shapiro et al., 2005) or 3 (e.g. Lin et al., 2007) times the dominant wavelength λ at that frequency, the NCF tends to degenerate in an autocorrelation, thus preventing any information to be retrieved. This because of the interference between the signals at positive and negative lags and the spurious precursory arrivals at long periods. As a consequence, there is a low-frequency bound to be taken into account, below which degradation of dispersion measurements are observed: $f_{min} = 3c/r$, where c is phase velocity.

Another key factor is represented by the temporal repeatability of the NCF measurements. The sources of microseisms change in time, thus providing different conditions for the measurements; therefore the repeatability of a measurement indicates its reliability. It is, therefore, useful to quantify the seasonal variability of each measurement and then to equate this with the measurement uncertainty (Yang et al., 2007; Lin et al., 2007; Bensen et al., 2007).

To compute seasonal variability, the NCFs, for a given station-pair, are stacked over 3-month-long time windows shifted by 1 month (for example January-February-March, February-March-April, etc.) spanning the entire data set. For each three-month NCF block, the spectral SNR is computed and the dispersion curve is estimated.

For any given frequency, the velocity measurement is accepted if there are more than $1+N_m/2$ (N_m is the half-length of the dataset in months) 3-month stacks whose SNR exceeds a threshold which is usually between 10 and 20 dB.

For dispersion measurements that meet this condition, the standard deviation of the group velocities using the 3-month blocks is computed. Finally, the measurements with standard deviation of the group velocity higher than a threshold value (depending on the precision sought) are discarded.

Following the aforementioned selection criteria, it is possible to identify the more reliable frequency bands for the dispersion measurements, and to obtain a quantitative estimate of the associated errors.

3.3 The Spatial Auto-Correlation (SPAC) Method

The estimation of the phase velocity dispersion curves from cross-correlated seismic ambient noise is usually operated with the spectral approach known as SPatial Auto-Correlation (SPAC) technique (Aki, 1957). This approach is able to resolve velocities at inter-station distances shorter than one wavelength.

The SPAC method was first introduced by Aki (1957, 1965), who described the theoretical background for different propagation cases (stationary waves with constant velocity, dispersive waves having a single or multiple velocity for each frequency, polarized waves, isotropic and plane waves) and describing the result of applications to the cultural seismic noise recorded at Tokyo. The core of the technique is to record seismic ambient noise at an array of stations, and then compute the cross-correlation functions between all the different pairs of stations at the same offset, thus sampling different azimuths. Under the assumption that the wave-field is stationary and stochastic in space and time, Aki (1957) demonstrated that the ratio of the azimuthally-averaged spatial correlation function and the autocorrelation function at a reference station is related to the zero-order first-kind Bessel function by the simple relationship:

$$\overline{\rho}(r,\omega_0) = J_0\left(\frac{\omega_0}{c(\omega_0)}r\right) \tag{3.7}$$

where $\overline{\rho}(r,\omega_0)$ is the azimuthal average of the normalized zero-lag correlation coefficients evaluated at the frequency ω_0 between a set of receivers

separated by the same distance r.

The above equation 3.7 is the key formula for SPAC method; it shows that the dispersion curve $c(\omega_0)$ can be obtained directly from the measurement of $\overline{\rho}(r, \omega_0)$ at various frequencies ω_0. The azimuthal average has to be practically interpreted as the averaging of the autocorrelation coefficients for station-pairs with equal distances but oriented at different azimuths.

The SPAC method, in its original formulation and further extensions, has been applied to many different contexts and scales; among the numerous studies, I recall the applications to volcanic edifices (e.g. Stromboli, Chouet et al. (1998); Kilauea, Ferrazzini et al. (1991)), urban environments (Morioka city in Japan, Yamamoto (2000); Grenoble sedimentary basin, Bettig et al. (2001); Brussels is Belgium Wathelet et al. (2004); Thessaloniki city in Greece Apostolidis et al. (2004); Beijing in China, Wang et al. (2014)), alluvial valleys (Chávez-García et al. (2006)); Köhler et al. (2007)), the subduction zone of Western Washington (Calkins et al., 2011).

3.3.1 SPAC Implementation

Henstridge (1979) established the frequency range of validity of the SPAC method, stating that the product between the inter-station distance and the wavenumber $rk = r(\omega/c(\omega))$ must lie in the range $0.4 - 3.2$. This condition can alternatively be expressed in terms of the wavelength λ as:

$$2 \leq \frac{\lambda}{r} \leq 15.7 \tag{3.8}$$

because the errors in $J_0(rk)$ are greatly magnified outside this range. The upper limit in 3.8, expressed also as $r \geq \lambda/15.7$, indicates that wavelengths that are too large, once compared to the inter-station distance, cannot be properly resolved. On the other hand, the lower limit, $r \leq \lambda/2$, represents the spatial Nyquist limitation, bounding the validity at higher frequencies.

The first application of the methods involved circular arrays with a reference station at the center (e.g. Aki, 1957). Okada (2006) found that isosceles triangular array is the most efficient geometry, with the upper frequency

limit corresponding to the frequency at which the SPAC curve takes its first minimum. Up to this limit (wavenumber or frequency), the error, due to the non-continuous spatial sampling of the real array, is comparable to that associated with an infinite number of stations as stated by the theory.

Subsequently, other regular array geometries have been used, for instance the semi-circular (e.g. Saccorotti et al., 2003) and hexagonal ones (e.g. Roberts and Asten, 2004). Bettig et al. (2001) developed the modified-SPAC method which allows arbitrary array layouts; he computed the average of the spatial autocorrelation coefficient on rings of discrete thickness in the plane (r, ψ) (polar coordinates), thus dividing the array into several equivalent semicircular sub-arrays defined by the pairs of stations whose distance is included in the discrete thickness of a ring. An application of this modified-SPAC, made for the 3-components data, can be found in the work of Köhler et al. (2007).

Of particular relevance is the work by Chávez-García et al. (2006), who showed that it is possible to get reliable results using in-line array configuration, provided the wave-field propagates with almost equal power in different directions. Under this hypothesis, long-enough records are assumed to sample all the different directions, thus allowing the substitution of the azimuthal average of the spatial autocorrelation coefficients with a temporal average.

A note must be made on the imaginary part of the SPAC-coefficients, that should ideally be zero for a sufficiently dense, circular array and/or a sufficiently isotropic wave-field. These two situations are difficult to encounter in practical cases. Thus, the non-zero imaginary part of the SPAC-coefficients provides a quality-control indicator (Asten, 2006) about:1) an indication of insufficient spatial averaging, 2) an empirical measure of the level of the error in SPAC, 3) an indication of a azimuthally non-uniform power of the seismic noise wave-field (Cox, 1973).

3.3.2 SPAC and the Green's Functions

This section presents the relationship linking the autocorrelation coefficients and the GFs.

The application of the SPAC is based upon the assumption that the wave-field is stationary both in time and space.

Under these conditions, the azimuthally-averaged autocorrelation function can be replaced by the averaged autocorrelation function taken for a single stations-pair. As a consequence, SPAC is expected to work also when applied to a sufficiently long noise window recorded at a single pair of stations (e.g Chávez-García et al., 2005; Ekström et al., 2009; Calkins et al., 2011), thus becoming the spectral equivalent of the NCF technique (e.g. Chávez-García and Rodríguez, 2007). Thus, if $u_x(\omega)$ is the spectrum of the wave-field recorded at a x-position, the time averaged cross-spectrum (corresponding to a cross-correlation in time domain) between the sites A and B, separated by the distance r, at the angular frequency ω_0, can be represented by:

$$\langle u_A(\omega_0) u_B^*(\omega_0) \rangle = P(\omega) J_0 \left(\frac{\omega_0}{c(\omega_0)} r \right) \tag{3.9}$$

where the $*$ is the complex conjugate symbol, $P(\omega)$ is power spectral density of the wave-field and the brackets $\langle \cdot \rangle$ represent the ensemble average.

Let us consider the Green's function $G_{AB}(\omega)$ in the frequency domain for the two stations in A and B, for the Rayleigh waves (Morse and Feshbach, 1953; Sánchez-Sesma and Campillo, 2006; Prieto et al., 2009):

$$G_{AB}(\omega) = -\frac{1}{4} \mu [Y_0(kr) + i J_0(kr)] \tag{3.10}$$

where Y_0 and J_0 are respectively the the second kind and the first kind Bessel functions of zero order, and μ is the shear modulus. It is shown, that normalizing the left term in equation 3.9 by the common power spectral density, $P(\omega)$, should give the imaginary part of the GF, as also found by Gouedard et al. (2008). In real observations the ambient noise wave-field spectral power is not a-priori known, but it can be approximated by the spectral average observed at the two sites. This choice of approximation lead

to the definition of the complex coherence $\gamma_{AB}(\omega)$ (Yokoi and Margaryan, 2008; Prieto et al., 2009) as:

$$\gamma_{AB}(\omega) = \left\langle \frac{u_A(\omega)u_B^*(\omega)}{\langle|u_A\omega|\rangle\langle|u_B\omega|\rangle} \right\rangle \propto J_0\left(\frac{\omega}{c(\omega)}r\right) \tag{3.11}$$

The complex coherence corresponds to the Fourier transform of noise cross-correlation function (NCF), in time domain, of the pre-whitened waveforms (Prieto et al., 2011).

In the ideal case of an uniform and equipartitioned wave-field, the NCF is symmetric (see section 3.1) and the imaginary part of its Fourier transform (or the complex coherence) is zero for all frequencies; as a consequence, the non-zero imaginary part of the complex coherence can be seen as a quality control of the method, as discussed at the end of the section 3.3.1

One crucial difference between the modified SPAC and the NCF is the wavelength scale, that for the former is ruled by the Henstridge (1979) criterion in 3.8 and should be longer than the inter-stations distance, while for the NCF should be shorter than the inter-stations distance, as seen in section 3.2.4.

Once computed the SPAC-coefficients for all the available station-pairs of the array, it is possible to measure the phase-velocity dispersion curve (PVDC) using the key-SPAC-formula 3.7, or the 3.11 formula when the time-averaged version with complex coherence is preferred.

In this thesis I applied the modified-SPAC method to an arbitrary-shaped array, using the complex coherence. The processing of the data has been the same as for the NCF technique, described in the section 3.2.1. The inversion for the PVDC has been performed following two different approaches, that allow the estimate:

1. an average PVDC for the array-area (detailed in section 3.3.3),

2. PVDCs for each single station-pair profile (detailed in section 3.3.3).

3.3.3 SPAC-Inversion for Array-Average

The inversion procedure, described here, leads to the estimation of an average phase-velocity dispersion curve (PVDC) corresponding to the underground structure considered constant under the entire array of seismic stations.

The concept is to minimize the difference between the SPAC-coefficients and the function $J_0\left(\frac{\omega}{c(\omega)}r\right)$, in order to find the best estimate of the PVDC $c(\omega)$.

The problem can be rewritten in the standard notation form $\mathbf{d}_0 = g(\mathbf{p})$, where $\mathbf{d}_0$ is the data vector of the SPAC-coefficients, $\mathbf{p}$ the vector of the model parameters to be found ($c(\omega)$) and $g(\cdot)$ is the function relating $\mathbf{d}_0$ and $\mathbf{p}$, that is the zero-order Bessel function of the first kind $J_0(\cdot)$. The vector $\mathbf{d}_0$ has dimension $Nf * Nr \times 1$, where Nf is the number of frequencies and Nr is the number of the pairs of stations. The vector $\mathbf{p}$ has dimension $Nf \times 1$. The solution for this non-linear problem is found using the following iterative algorithm (Tarantola and Valette, 1982; Bettig et al., 2001; Chávez-García et al., 2005):

$$\mathbf{p}_{k+1} = \mathbf{p}_0 + \mathbf{C}_{p_0p_0}\mathbf{G}_k^T(\mathbf{C}_{d_0d_0} + \mathbf{G}_k\mathbf{C}_{p_0p_0}\mathbf{G}_k^T)^{-1}[\mathbf{d}_0 - g(\mathbf{p}_k) + \mathbf{G}_k(\mathbf{p}_k - \mathbf{p}_0)] \quad (3.12)$$

where k is the iteration-step index and the superscript T means the transpose of a matrix. The starting point ($k = 0$) is to chose an a-priori model parameters $\mathbf{p}_0$, that can be a known PVDC for the area or a theoretical curve sufficiently close to reality. The estimate of the $\mathbf{p}$ at the $k+1$ step is obtained by considering:

- the covariance matrix of the parameters ($\mathbf{C}_{p_0p_0}$),
- the covariance matrix of the data ($\mathbf{C}_{d_0d_0}$),
- the $g(\cdot)$, i.e. $J_0(\cdot)$, computed for the preceding step parameters $\mathbf{p}_k$,
- the matrix $\mathbf{G}_k$ containing the partial derivatives of the model function ($g(\mathbf{p})$) with respect to the parameters $\mathbf{p}_k$.

For the cases considered in this work (expressed by equations 3.7 or the 3.11),

the matrix G is:

$$G = \frac{\partial g(p)}{\partial p} = \frac{\omega r}{c^2(\omega)} J_1 \left(\frac{\omega r}{c(\omega)} \right) \tag{3.13}$$

The dimension of G is $(Nf * Nr) \times Nf$. In order to guarantee the smoothness of the final PVDC, and thus the most likely solution, the covariance matrix of the parameters has this expression, proposed by Tarantola and Valette (1982):

$$C_{p_0 p_0}(\omega, \omega\prime) = \sigma^2 \exp \left[\frac{-(\omega - \omega\prime)^2}{2\Delta^2} \right] \tag{3.14}$$

This expression indicates a smoothing in frequency of the matrix $\mathbf{C}_{p_0 p_0}$ at the frequency $\omega\prime$, controlled by the frequency smoothing window Δ and a maximum accepted change σ of each parameter $p = c(\omega)$ between two iterations. This filter privileges neighboring frequencies, instead of distant ones.

The variances resulting from the measurements of the SPAC-coefficients are collected in the $\mathbf{C}_{d_0 d_0}$ matrix.

Finally, the a-posteriori covariance matrix $\mathbf{C}_{pp}$ is computed to estimate the errors on the parameters (Tarantola and Valette, 1982; Bettig et al., 2001; Chávez-García et al., 2005):

$$\mathbf{C}_{pp} = \mathbf{C}_{p_0 p_0} - \mathbf{C}_{p_0 p_0} \mathbf{G}^T (\mathbf{C}_{d_0 d_0} + \mathbf{G} \mathbf{C}_{p_0 p_0} \mathbf{G}^T)^{-1} \mathbf{G} \mathbf{C}_{p_0 p_0} \tag{3.15}$$

3.3.4 SPAC-Inversion for Individual Profiles

The algorithm for the determination of the PVDCs related to individual station-pair profiles is based on Ekström et al. (2009), except for the preprocessing of data, that is the one described in section 3.2.1. For this inversion, data are represented by complex coherence estimates.

First, the complex cross-spectrum of a couple of stations (equation 3.11) is computed. The inversion for $c(\omega)$ is performed by equating the zero-crossing of the real spectrum of the SPAC-coefficients to the zero-crossings z_n of the Bessel function $J_0 \left(\frac{\omega_0}{c(\omega_0)} r \right)$. This directly yields the estimate of phase velocity as:

$$c(\omega_n) = \frac{\omega_n r}{z_n} \tag{3.16}$$

The recognition of the actual zero-crossing in the observed SPAC-coefficients can be challenging, causing missed or extra zeros. As a consequence, Ekström et al. (2009) suggests to estimate a number $|m|$ of PVDCs, in order to account for extra $m > 0$ or missed $m < 0$ zeros crossing, z_{n+2m}. The evaluated $c(\omega_n)$ can be divided into two curves, one for the negative-to-positive zero-crossings and the other for the positive-to-negative. The criteria for evaluating the validity of the measurements of the dispersion curves are: i) the smoothness, ii) the continuity and iii) an acceptable velocity values Ekström et al. (2009). Furthermore, the distance between up-going and down-going zeros at each frequency is used as a selection criterion.

Chapter 4

Secondary Microseism at the Larderello-Travale Geothermal Field (LTGF): characterization and variability

This chapter describes the experimental data used for this thesis. First, I present an overview of the area where the experiment was conducted, that is the Larderello-Travale geothermal field (LTGF; Tuscany, Italy). Then, I detail the data-collection procedures, and the subsequent archiving procedures. Last, the main characteristics of the observed secondary microseisms are reported.

4.1 Geological-Geophysical Frame of the LTGF

The Larderello-Travale Geothermal Field (LTGF) is located in southern Tuscany, on a structural high within the northern pre-Apennine belt. The LTGF is the most ancient exploited geothermal field in the world (e.g. Lund, 2004). The first industrial exploitation began in 1818 with the extraction of boric acid from geothermal vents, and geothermal electricity (250 kW geothermo-

electric unit) was first commercialized in 1913 (Arias et al., 2010). Thus far, the reservoir is exclusively exploited by ENEL (the former Italian governmental power company) using more than 200 wells, reaching a maximum depth of about 4 km below the surface.

From the geological point of view (see figure 4.1a), 3 regional tectonostratigraphic elements outcrop and overlie the metamorphic substratum (Batini et al., 2003). In reverse chronological order, these are:

1. continental to marine sediments filling up the extensional tectonic depressions (Late Miocene to Pliocene and Quaternary);

2. the Ligurian Complex, that was thrust eastwards over the Tuscan Domain (Late Oligocene-Early Miocene). The Ligurian Complex is composed by: Ligurian Units and Sub-Ligurian Unit. The Ligurian Units are composed of Jurassic oceanic basement and its pelagic sedimentary cover. The Sub-Ligurian Unit is composed by limestones and clays belonging to a paleogeographical domain interposed between the Ligurian Domain and the Tuscan one.

3. the Tuscan Nappe, that is related to the sedimentary cover of the Adria continental paleomargin (Late Triassic-Early Miocene) detached along the Triassic evaporites and thrust over the paleogeographical domains during the Late Oligocene-Early Miocene.

The Tuscan metamorphic complex is the substratum of the LTGF. It is composed of 2 metamorphic units:

1. the Upper Monticiano-Roccastrada Unit, composed by:

   (a) The Verrucano Group: phyllites and metacarbonates (Upper Triassic) related to marine litoral facies, and continental quartzites and quartz conglomerates (Middle-Early Triassic); this group is imbricated in duplex structure;

   (b) The Phyllites-Quartzite Group: phyllite and quartzite (Paleozoic) affected by greenschist metamorphism;

(c) The Micaschist Group: micaschists and quartzites with amphibolite zones (Paleozoic) affected by Hercyan metamorphism.

2. the lower Gneiss Complex: gneiss and paragneiss with intercalation of amphibolites and orthogneiss not affect by any orogenetic metamorphism.

Contact aureoles have been created by dykes emplaced (Pliocene) in the metamorphic substratum. These dykes have been reached by deep borehole exploration (e.g. Bertani et al., 2005).

Figure 4.1b illustrates the stratigraphic-tectonic setting of the LTGF, after Bertini et al. (2006).

The LTGF is a superheated-steam geothermal system, where the reservoir is filled with dry vapour, and whose pressure is much lower than the hydrostatic gradient. The total area is about $70 \times 70\text{Km}^2$ with a production of total steam flow rate over 4700 t/h (Arias et al., 2010). The produced geothermal fluids have temperatures ranging between 150-260℃ and pressure between 2–15 bar (high enthalpy). The composition of these fluids are mainly superheated water steam and minor gases (max 15 % by weight) essentially made up of CO_2 and H_2S (e.g Minissale, 1991; Batini et al., 2003). According to Cameli et al. (1993, 1998), the micro-fracturing associated with the continuous microseismic activity of the area overwhelms fracture enclosure caused by the deposition of hydrothermal minerals, thus guaranteeing perduration of the permeability.

There are two recognized and exploited geothermal reservoirs in the LTGF. The superficial reservoir (0.5-1.5 Km depth, and 250℃) is located between the Late Triassic evaporites and the Jurassic carbonatic formations; the cover of this reservoir is represented by the Tuscan Nappe, the Ligurian Units and Miocene-Pliocene sediments (e.g. Batini et al., 2003). The superficial reservoir experienced a decline in production in the '70s, so that the exploration was directed toward the deepest reservoir (De Matteis et al., 2008). The presence of such deep reservoir, at 3-4 Km depth, was then confirmed through several wells (Sesta_6bis, Travale Sud_1 and Montieri_4 [1]), exhibit-

[1] for the location of the exploration wells see figure 4.4

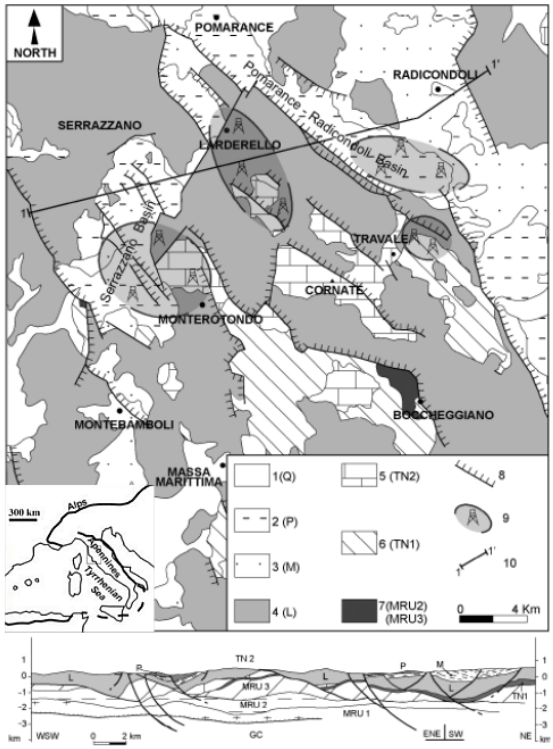

(a)

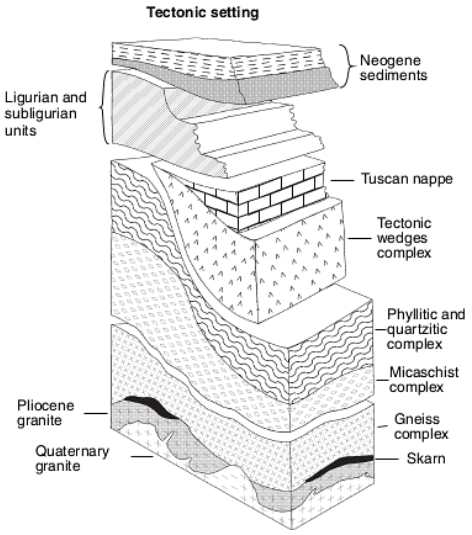

(b)

Figure 4.1: *Geological settings of the Larderello-Travale Geothermal Field (Tuscany, Italy). Figure 4.1a: 1—Quaternary continental sediments; 2—Pliocene marine sediments; 3—Miocene continental and marine sediments; 4—Ligurian units l.s. (Jurassic- Eocene); 5—Tuscan Nappe: Late Triassic- Early Miocene sedimentary sequence; 6—Tuscan Nappe: Late Triassic basal evaporite (Burano Fm.); 7—Palaeozoic Phyllite- Quartzite Group (MRU 2) and Triassic Verrucano Group (MRU 3); 8—Normal faults; 9—Main geothermal fields; 10—Trace of geological cross-section. (MRU 1)—Palaeozoic Micaschist Group; (GC)–Gneiss Complex, after Batini et al. (2003). Figure 4.1b: stratigraphic-tectonic setting of the LTGF, after Bertini et al. (2006).*

ing pressures up to 70 bar and temperatures ranging between 300 and 350 ℃(Barelli et al., 1995, 2000). This reservoir is located within the metamorphic basement, in correspondence of a wide contact metamorphic aureole. The extension of the deep reservoir toward South-West was verified by the deep-exploratory well (4.379 Km) PZ_2, located at $\sim$ 5 Km South-East of Larderello (Bertani et al., 2005).

The metamorphic basement and the overlying calcareous-anhydrite formations represent a structural high (Bertini et al., 1994) constituted by high-density rocks (about 2.7g/cm^3), but characterized by a wide negative gravimetric anomaly; that anomaly has been interpreted in terms of a partially-molten, low-density body with temperatures up to 800℃ (Baldi et al., 1995). The top of the negative anomaly is located at depths ranging between 3 km (below the central sector of the LTGF (Cameli et al., 1998)) to 8 Km, and it correlates well with the K-horizon, a seismic marker appearing as a rather-continuous reflector of high amplitude and frequency, which separates a poorly reflective upper-crust from a highly–reflective mid-lower crust (Cameli et al., 1993; Brogi et al., 2003). This reflector presents bright spots and a sharp decrease in acoustic impedance (Batini and Villa, 1985; Liotta and Ranalli, 1999). The reason for this high reflectivity is still debated. Some authors (e.g. Batini and Villa, 1985; Brogi et al., 2003) assert that it represents the seismic signature of a fractured zone containing fluids under pressure, associated with a brittle/ductile transition zone of the rocks caused by the high temperature gradient.

Another significant reflector (the H-horizon) is found at 2-4 Km depth, with amplitude features which are similar to those of the K-horizon. The H-marker corresponds to the contact aureole of the Pliocene granites. The wells that reach this marker show temperatures between 300–350 °C and superheated steam entries with flow rates of more than 50 ton/h (Bertini et al., 2006). The H-marker is explained as a fossil K-horizon (e.g. Calcagnile and Panza, 1980; Baldi et al., 1995; Bertini et al., 2006); since it has associated the most voluminous steam storage systems, it represents the current target of geothermal exploration.

Figure 4.2 illustrates the K- and H-horizons as evidenced by a seismic profile crossing the LTGF.

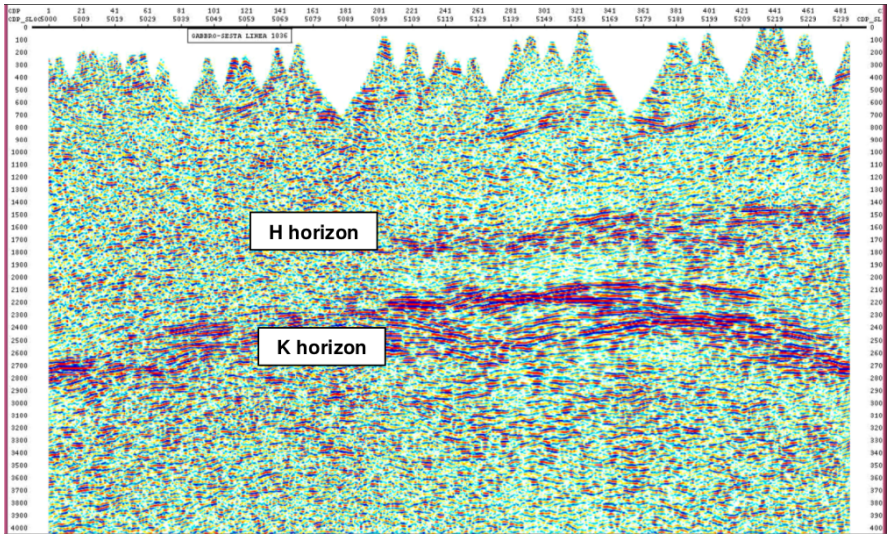

Figure 4.2: *Example of one seismic stack section of LTGF, relative to a seismic survey conducted in 2003 and published by Cappetti et al. (2005). Here both the K and H horizons are marked.*

4.1.1 Seismological Studies

The seismicity of geothermal areas often exhibits a different behaviour from the surrounding regions (Foulger, 1982), likely representing crustal sectors where regional stresses are released at a different rate. This consideration well applies to LTGF, whose seismicity is significantly higher than that observed in the adjoining areas. The two most significant ($M > 5$) historical earthquakes occurred in 1414 and 1724, with equivalent magnitudes of 5.6 and 5.4, respectively (see http://emidius.mi.ingv.it/DBMI11/).

During the 70's, ENEL began a program of instrumental monitoring of the exploration and production cycles. These data report low- to moderate-intensity earthquakes ($M< 4$) widespread throughout the geothermal area; hypocentral depths are rather shallow (< 10 km), and they do generally follow the K-horizon, though shallower clusters of seismicity are reported for the southernmost part of the geothermal field (e.g. Batini et al., 1985; Con-

sole and Rosini, 1998; Saccorotti et al., 2013).

Since the late 70's, the reinjection of waste water into the production wells has caused a significant increase of the general seismicity rate, and a clear correlation between volume of water injected and event count was observed. Nonetheless, no change in the frequency of occurrence for events of magnitude ML $\geq$ 2.0 was evident (Batini et al., 1985).

In addition to the results from active reflection and/or refraction seismic surveys (Cappetti et al., 2005; Casini et al., 2009)), the seismic imaging of the LTGF has been improved by several passive 3-D tomographic studies. A deep structure, with P-wave velocity 6-6.5 Km/s, with a convex shape dipping towards N-E and S-E was recovered by Vanorio et al. (2004). By analyzing V_p/V_s, $V_p \times V_s$ together with earthquake clusters, these authors found evidences for an overpressure zone at 5-6 Km depth around the Travale well, for which the higher porosity at depth is supported by pore fluid pressure (De Matteis et al., 2008). Fractured steam-bearing formations have been inferred under Lago and the Miniera Padule-Travale areas, at depths ranging from 2 to 5 Km. These formations were evidenced by low value of P-wave velocity (3.5-5.2 Km/s) (Vanorio et al., 2004) causing low V_p/V_s. De Matteis et al. (2008) also found higher but less frequent V_p/V_s anomalies at shallow depths, due to the higher V_p and low V_s. These latter anomalies were interpreted in terms of condensation zones and/or zones affected by water recharge.

4.2 The GAPSS Experiment

The data used in this thesis have been collected in the frame of GAPSS (Geothermal Area Passive Seismic Sources) project, conducted by the Italian Istituto Nazionale di Geofisica e Vulcanologia (INGV). The GAPSS project started on early May, 2012, and was decommissioned in late October, 2013.

The experiment was mostly aimed at testing robustness and feasibility of passive seismological techniques to the evaluation of the geothermal potential, using a test area for which the subsurface rock properties are already

constrained through the existing geological and geophysical information.

During the time interval that I accounted for, the GAPSS experiment consisted of a large- aperture seismic array of 11 temporary stations, complemented by two permanent stations (Trifonti-TRIF and Frosini-FROS) pertaining to INGV's National Seismic Network (RSN). The total area spanned by the depolyment is about 50×50 Km, and the average station spacing is on the order of 10 km. A map of the GAPSS array is reported in figure 4.3.

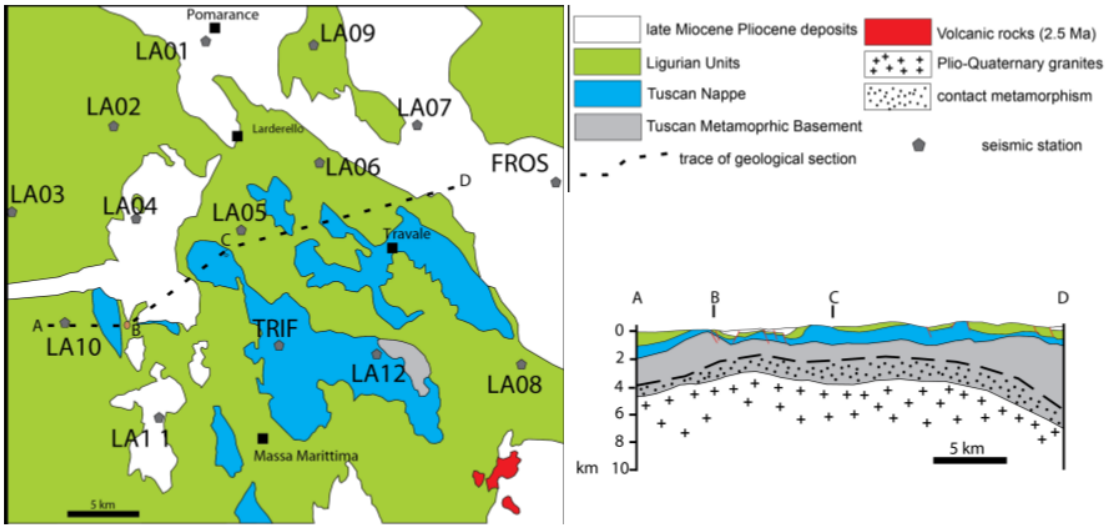

Figure 4.3: *Map of the GAPSS broad-band seismic stations array at the LTGF. The indicated lithologies are referred to the ones described in the section 4.1. After Piccinini et al. (2013).*

During the late part of the experiment (April - October 2013), 10 additional stations were added, but they were not used for the analyses conducted in this thesis.

All the temporary stations were equipped with Reftek RT-130 digitizers connected to either broadband (Trillium-compact-120s; TR120) or intermediate-period (Lennartz LE3D-5s;LE5) seismometers (figure 4.5). The 2 RSN stations consisted instead of GAIA2 digitizer equipped with broadband, Nanometrics Trillium-40s (TR40) seismometer. Details for all the seismic stations are reported in table 4.1. All the temporary stations were provided by the RE.MO. (Mobile Seismic Network) facility at INGV-CNT (Centro Nazionale

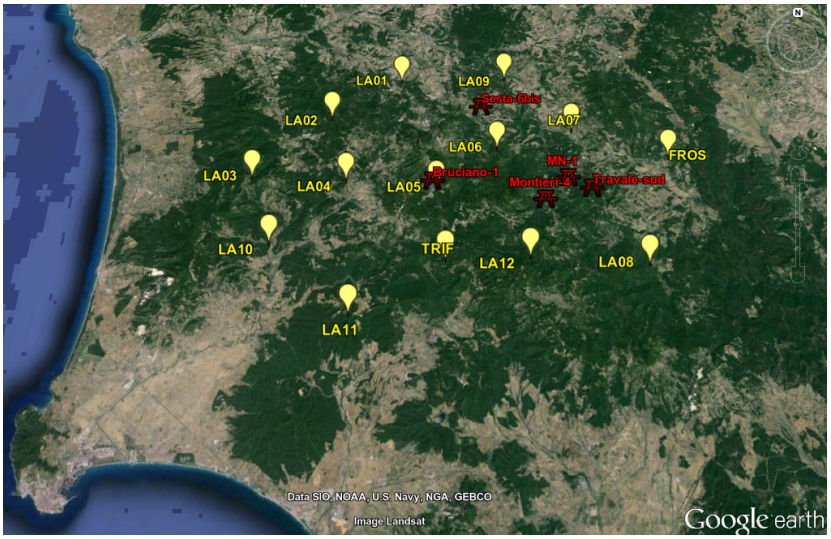

Figure 4.4: *Map of the Larderello-Travale area, showing the location of the exploration wells (red symbols) considered in this thesis with respect of the location of the seismic stations of the GAPSS array (yellow symbols).*

Terremoti).

(a) (b)

Figure 4.5: *Examples of sensor installation: 4.5a Nanometrics Trillium-Compact-120s; 4.5b) Lennartz 3D-5s*

Name	Site	Latitude[°]	Longitude[°]	Elevation [m]	Sensor
LA01	Pomarance (PI)	43.28513	10.85864	231.0	TR120
LA03	Monteverdi Marittimo (PI)	43.18781	10.69112	455.0	TR120
LA04	Lustignano (PI)	43.18554	10.79517	377.0	LE5
LA05	Castelnuovo Val di Cecina (PI)	43.17688	10.89395	688.0	LE5
LA06	Solaio (SI)	43.21674	10.96401	477.0	TR120
LA07	Serracona di Sopra (SI)	43.23494	11.05047	436.0	TR120
LA08	Luriano (SI)	43.11203	11.11735	428.0	TR120
LA09	Montesastelli (PI)	43.28821	10.96067	355.0	TR120
LA10	Sassetta (LI)	43.12902	10.71486	139.0	TR120
LA11	Montebamboli (GR)	43.06939	10.80181	340.0	TR120
LA12	Montieri (GR)	43.11705	10.99232	699.0	TR120
FROS	Frosini (SI)	43.20972	11.15622	432.0	TR40
TRIF	Trifonti (GR)	43.11478	10.90265	596.0	TR40

Table 4.1: *Table of GAPSS array stations with name, location, coordinates and the sensor type*

4.3 Data Collection and Organization

All the temporary stations worked in stand-alone mode, storing data on internal compact flash disks which were substituted approximately every 45 days.

Figure 4.6 shows the chronogram of the array's operation throughout the period analysed in this thesis (May 2012-March 2013). The major failures occurred during June-July 2012 period, because of the high temperatures reached by the instruments at many sites, such as LA01, LA04, LA06 and LA10 (figure 4.7). On November, 2012, 3 sensors were flooded (LA06, LA07, LA09), thus forcing a relocation of the stations. Heavy rain, and the consequent loss of soil rigidity, also caused tilting of a few other sensors. Additional failures include the theft of the digitizer at site LA08, and the unknown-origin fire of the digitizer at site LA02.

The preparation of the data archive proceeded according to the following steps:

1. conversion from the Reftek to the SAC©(Seismological Analysis Code) format (Goldstein et al., 2003; Goldstein, 2005);

2. for each station and channel, merging of individual data streams into day-long SAC©data files;

3. deconvolution for the instrument response (the characteristics of the different sensors and digitizers are shown in tables 4.2 and 4.3, respectively).

4. trend and mean removal;

5. anti-alias filtering (2 poles zero-phase Butterworth filter, with corner frequencies 0.008-1.5 Hz);

6. data decimation from the original sampling rate of 125 sps to 5 sps (sps = samples per second).

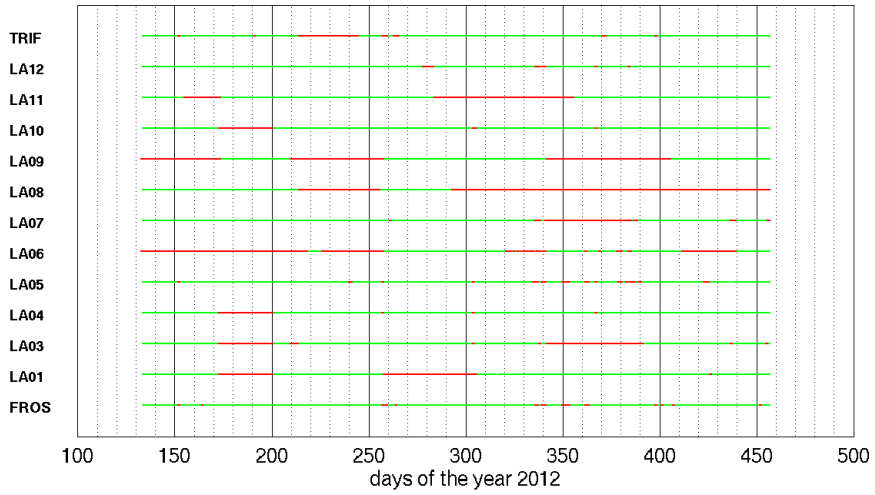

Figure 4.6: *Chronograph of operativity of the GAPSS stations from 11 May 2012 to 31 March 2013. The red dots correspond to the missing data.*

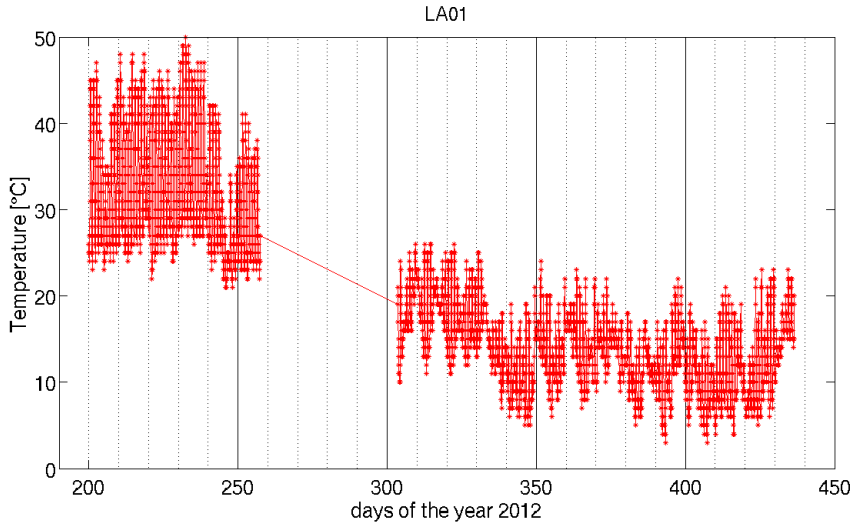

Figure 4.7: *Graph of the temperature of the LA01 station, for the period 18 July 2012- 11 March 2013.*

Instrument	Poles	Zeros	Ground Motion Sensitivity[Vsm^{-1}]
Nanometrics Trillium 120SP	-3.691e-02±i3.712e-02 -371.2 -373.9±i475.5 -588.4±i1508	0.0 0.0 -434.1	750
Nanometrics Trillium 40	-0.1111±i0.1111 -172.7±i262.37	0.0 0.0	1553
Lennartz LE3D-5s	-0.888+i0.887 -0.888-i0.888 -0.290+i0.000	0.0 0.0 0.0	400

Table 4.2: *Parameters of sensors used at the GAPSS stations.*

Instrument	Bit weight [V/counts]
Reftek	1.589x10-6
GAIA2	1.2718x10-6

Table 4.3: *Parameters of digitizers used in the GAPSS stations.*

4.4 The Observed Secondary Microseism

The spectral properties of the ambient seismic noise have been characterised using the power spectral density (PSD). PSD estimates are obtained by (a) calculating the Fast Fourier Transform (FFT) over 600-s-long data windows, sliding along the signal with 50% overlap; (b) averaging individual spectral estimates obtained over time intervals of 1 hour; (c) taking the square of the modulus of such averaged spectrum.

For each station and channel, the variability of the corresponding PSDs is then conveniently expressed in terms of the probability density function (PDF) of the signal's power at each frequency bin. These functions are eventually compared to the Peterson noise curves (Peterson, 1993), referred to as the New Global High- (NHNM) and Low-Noise Models (NLNM). Figure 4.8 shows examples of the PDFs for the PSDs computed for the entire observation timelapse May2012-March2013 at the three-component of stations LA03 and LA07.

On the vertical component of ground motion (figure 4.8a and b), the two microseism peaks previously described (see chapter 1) appear clearly at frequencies of $\sim$ 0.06 Hz and $\sim$ 0.17Hz, respectively. Both peaks are well-defined; the secondary peak has spectral power $\sim$ 10 dB stronger than the primary one. On both horizontal components (figures 4.8c-f), only the secondary peak is well defined, while the primary microseism power is obscured by long-period instrumental noise, which is likely caused by faulty sensor installation and/or thermal insulation. Actually, it is well known (e.g. Wielandt, 2003) that the horizontal long-period seismic data are noisier than the vertical one. If the seismometer undergoes tilt (as it is the case, for instance, of tight ground subsidence) a first order effect (sensitivity tilt) results in the horizontal sensor. Conversely, this effect is of second order for the vertical component, for which its is proportional to the square of the tilt.

The computation of PSDs over the entire data set allows to obtain spectrograms in which it is possible to recognize the microseism features and evidence seasonal variability. Figure 4.9 shows the spectrograms computed for the vertical (Z) component of all the GAPSS stations, over the May 2012 - March 2013 time span. For simplicity, the day-of-the-year (DOY) for the year 2013 are summed-up to those relative to 2012, i.e. with numbers > 365. Dark blue horizontal stripes correspond to missing data. Thin horizontal red lines, stretched along the frequency axis, correspond to earthquakes signals, as for example the Emilia Earthquake on the 29 May 2012 (doy 150), and other smaller local earthquakes, as the one visible at day 239.

As described in section 4.2, stations LA04 and LA05 were equipped with intermediate-period sensors (eigenperiod 5 seconds), thus in their spectrograms the frequencies below 0.1 Hz are contaminated by self-noise. At station LA09, from day 316 to 340 the spectrogram shows the effect of the flooding of the sensor, caused by heavy rains (http://www.sir.toscana.it/), after which the seismometer has been substituted. A similar flooding effect is observed at station LA07, on day 332.

In figure 4.9 the SM can be easily followed around frequency 0.2 Hz, as an almost continuous signal oscillating of few tenth of Hz depending on

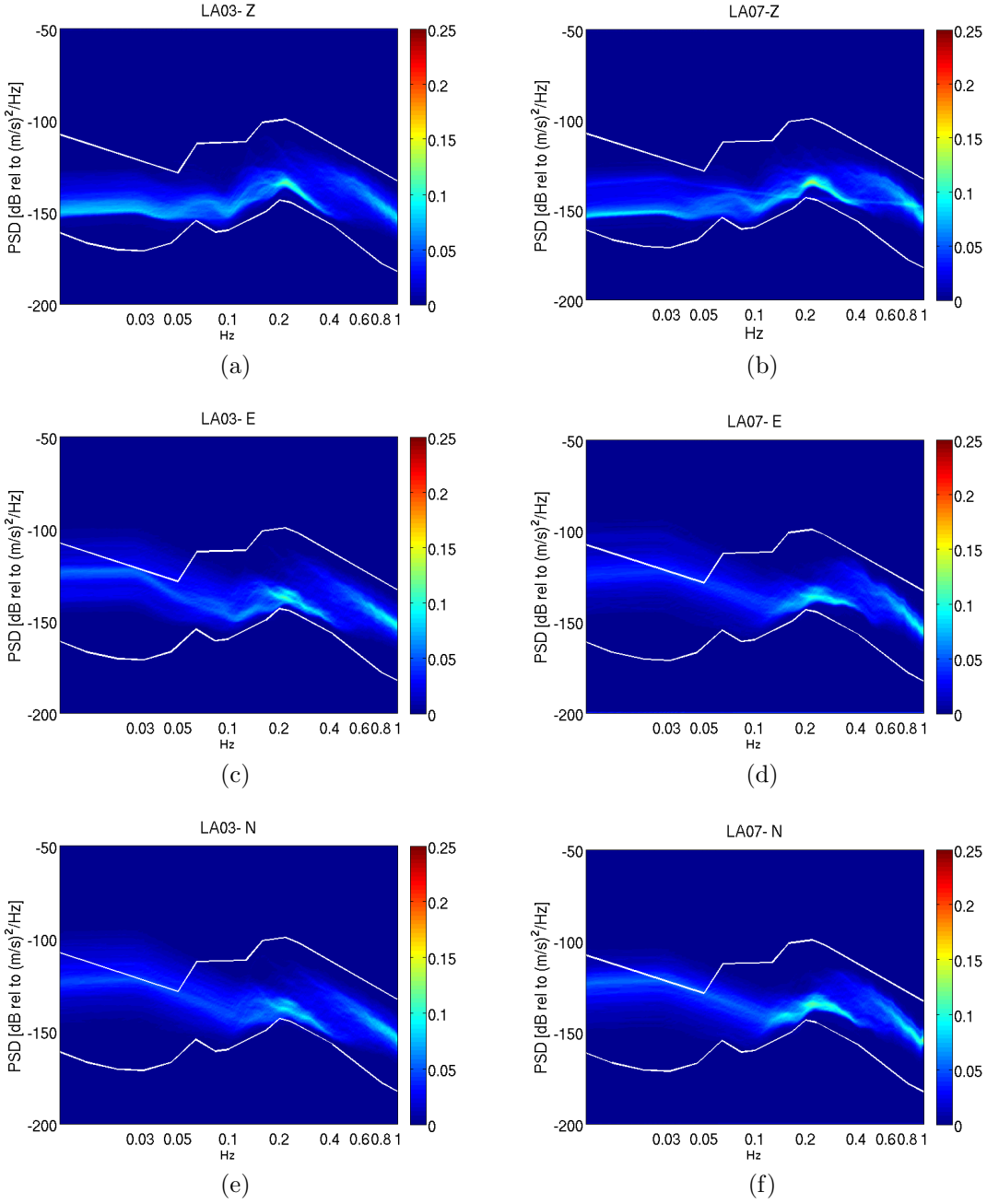

Figure 4.8: *Examples of the Microseisms PSD probability density function computed for the GAPSS stations LA03 (left) and LA07 (right), for the observation timelapse May2012-March2013. From top to bottom there are the 3 components: Z, E, N. At both stations, the two microseism peaks are evident on the vertical component; the PM peak is around the frequency 0.07 Hz, the SM peak is stable around 0.2 Hz. On the horizontal components, the PM peak is blurred by the instrumental noise, while the SM is still well resolved. Both stations show noise levels closer to the NLNM-curve.*

the storms evolution. The PM is less continuous, and it is stronger during autumn-winter time. The seasonal variability of microseisms is evident in the spectrograms in terms of varying power, which increases from summer to autumn days. The flame shaped signals, at frequencies > 0.2 Hz, are expression of local storms (see chapter 1), and their number increases in autumn-winter time. The spectrogram feature evidencing a migration of the power maxima, from higher frequencies to lower ones with consequently growing power levels, is known to correspond to the increasing speed of the wind and wave heights at the outbreak of the storm (Babcock et al., 1994). This effect can be often found in the spectrograms of figure 4.9, as for example throghout DOY 370-400.

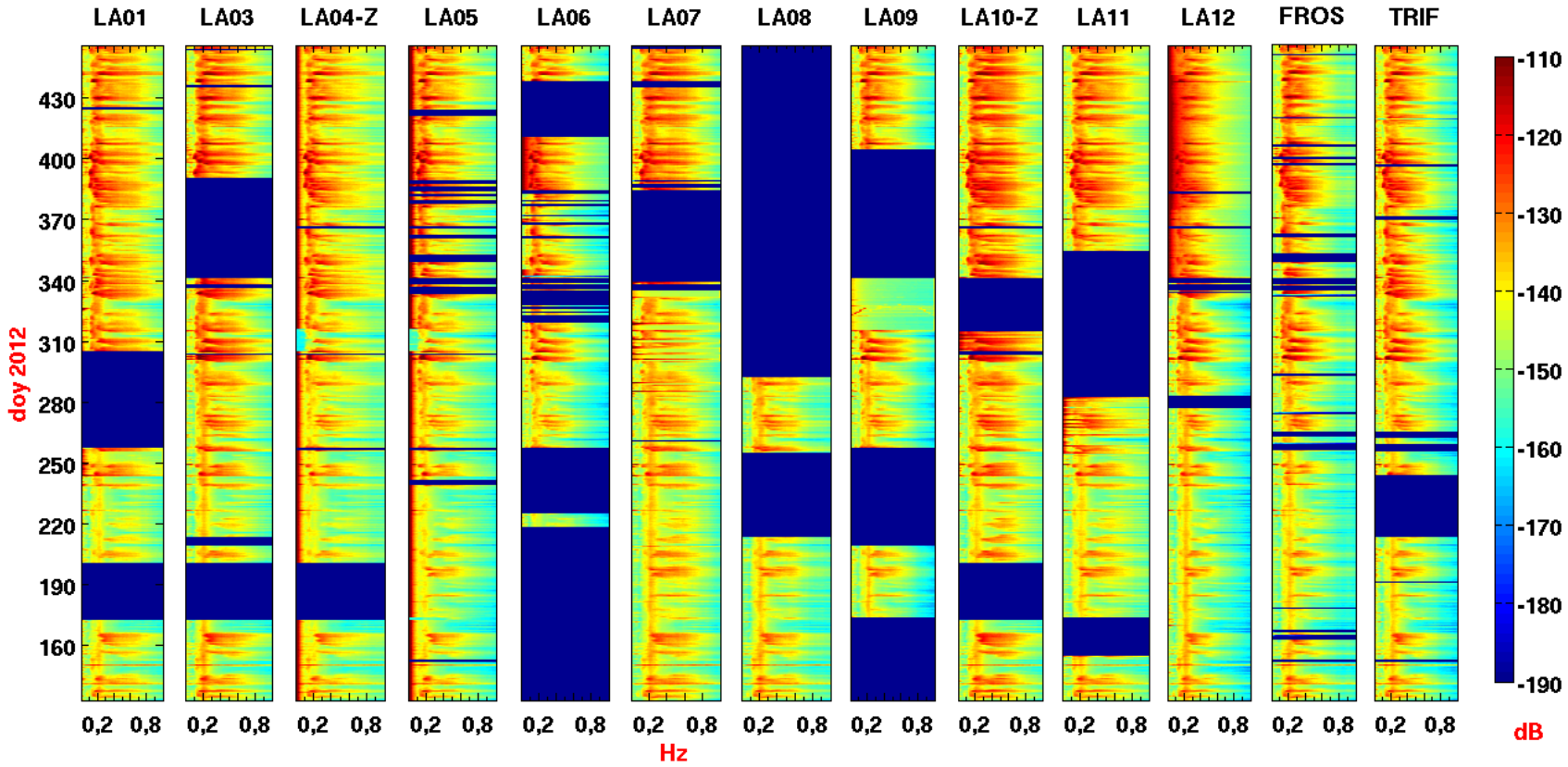

Figure 4.9: *Microseisms spectrograms covering the time span May-2012 to March-2013, for all the GAPSS stations. the abscissa axis are frequencies from 0 to 1 Hz. The ordinates axis is the time, in days of the year 2012. Dark blue horizontal bars are lost data.*

Chapter 5

Locating The Sources of Secondary Microseisms at LTGF

In this chapter I present the results about the identification of the sources of the secondary microseisms recorded at LTGF, using the deterministic array method (beamforming) described in chapter 2.

The first step toward the determination of the kinematic properties of the noise wavefield consisted in the choice of the most appropriate parameters for the calculation of the frequency-slowness spectra. In particular, the most critical parameters is the length of the time window that, in the context of SM, must guarantee an appropriate spatial sampling of the lowest frequency (0.1 Hz), and at the same time avoiding as much as possible the interferences of multiple signals. After numerous tests, I found that time blocks of 600 seconds, overlapping by 50% of their length, represented a good compromise between the former two requirements. The number of discrete smoothing frequencies for the computation of the cross-spectral matrix was set to 15, corresponding to 0.025 Hz.

The beamforming analysis is a time-expensive computing procedure. In order to extend the analysis to the entire timespan (May2012-March2013), by the same time meeting the exigence of good quality results at the minimum

time cost, I applied the following selection criteria to each time window:

- Inspection of the array beam-pattern, that is not constant from day to day, because of the discontinuous functioning of the different stations. As an example, figure 5.1 reports two examples of GAPSS sub-array geometries and the respective beam-patterns at 0.2 and 0.5 Hz. Because of the GAPSS geometry, even in the best possible condition (all the stations are operative), the slowness precision at 0.2 Hz is on the order of 0.1 s/Km; if a higher frequency is considered, the precision is better, at expenses, however, of the accuracy. Bearing in mind these considerations, I thus discarded those days for which less than 6 stations were operative;

- I discarded the time-windows including earthquakes signals, as recognized by parallel studies (Saccorotti et al., 2014);

- for each time-window, I conducted the slowness grid-search necessary to the computation of the beampower only for that frequency at which the spectral coherence was maximum.

Figure 5.2 shows the temporal evolution of the propagation parameters derived from beamforming analysis, throughout the entire period of observation (May2012- March2013), and computed for the entire SM band, i.e. 0.1-1 Hz. Each circle represents the average over 1-hour of data (11 measurements); the radius is proportional to the beam-power and the color indicates the spectral coherence multiplied by 100, according to the color bars at the right. Most of the retrieved frequencies span the 0.1-0.3 Hz frequency band. The highest spectral coherence and beam-power values emerge during the late-Spring/Summer time; these results are also characterized by low horizontal slownesses (< 0.3 s/km), indicating waves which impinge at the array with steep incidence angles. According to several previous studies, this observation can be interpreted in terms of converted P-phases (Gerstoft et al., 2008; Ruigrok et al., 2011), associated with SM sources generated by large storms in the austral hemisphere during its Winter (e.g. Webb, 1998; Stutzmann et al., 2009)

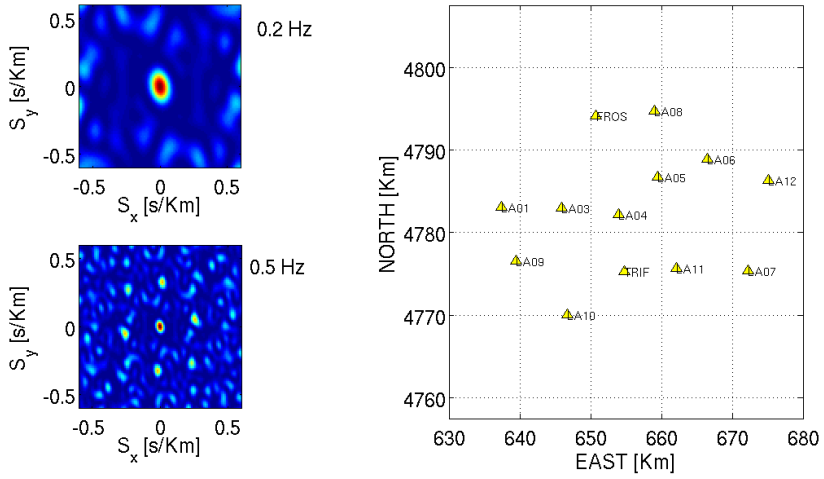

(a)

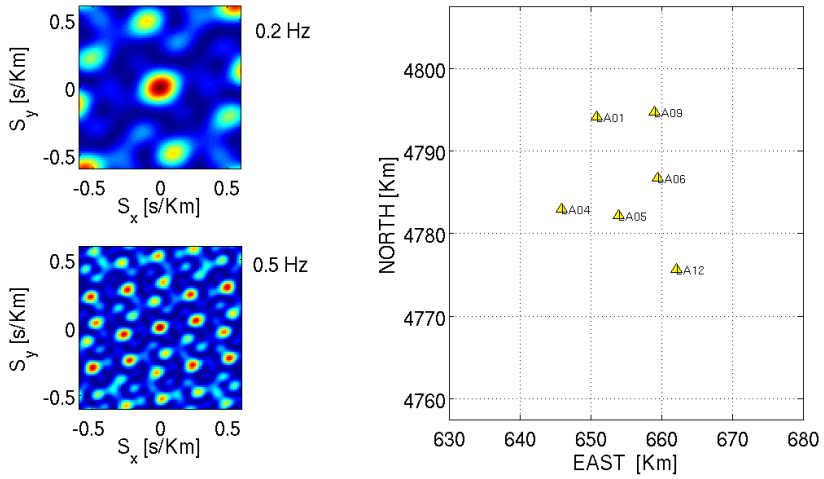

(b)

Figure 5.1: *Comparison of beam-patterns of two sub-arrays of GAPSS. In (a) all the GAPSS stations are operative, while in (b) only 6 stations are involved. Even if for the bigger array (a) the main lobe is more directional, the response is less affected by aliasing than the response of the sub-array (b).*

For the Autumn-Winter time periods, back-azimuths are scattered over a wide angular interval; the corresponding horizontal slownesses are compatible with what expected for surface waves at those frequencies, i.e. velocities generally lower than 3.5 Km/s at frequency ∼0.2 Hz.

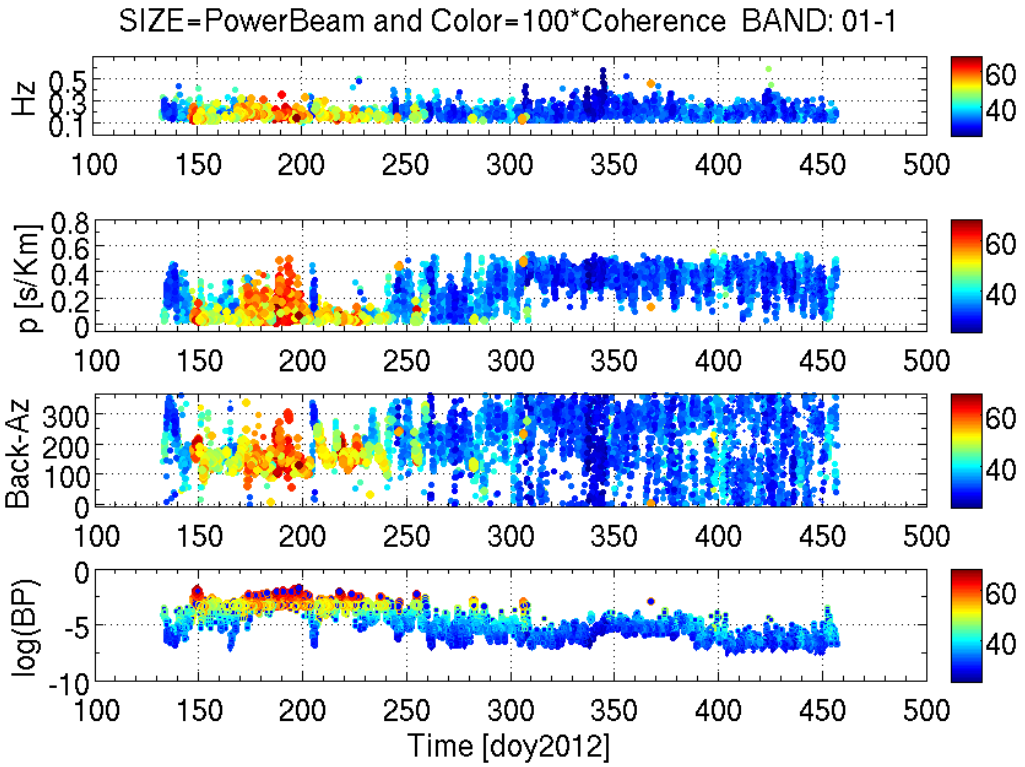

Figure 5.2: *Beamforming results for the frequency band 0.1-1 Hz, spanning 11 months (May 2012- March 2013). Each dot represents the 1-hour average, having radius proportional to the beam-power and color following the spectral coherence multiplied by 100. The abscissa axis is the time (day of the year 2012). The ordinate axis are, from top through bottom: frequency peak, horizontal slowness, back-azimuth and the logarithm of the beam-power.*

Figure 5.3 reports the 2-dimensional polar histograms summarizing the entirety of the results obtained over the 11 months of measurements. The two panels report the number of measurements as function of back-azimuth/slowness and back-azimuth/frequency, thus providing an immediate view about the mutual relationships between these quantities. For the 0.1-1 Hz frequency band, the most coherent microseisms have a peak frequency centered around 0.2 Hz, and are associated with sources in the South-East and North-West

quadrants. The microseisms coming from the mean direction 150°N are associated mostly to a very low slowness values (< 0.12 s/Km), and have been retrieved during the northern-hemisphere summer.

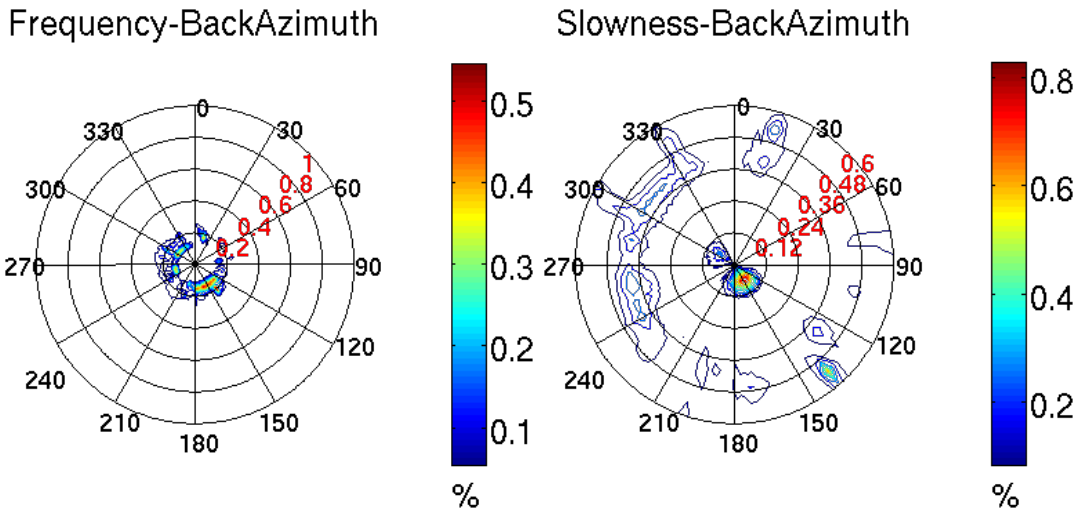

(a) (b)

Figure 5.3: *Polar histograms of the beamforming results of 11 months in the band 0.1-1 Hz. In figure (a) there is the frequency-backazimuth plot. In figure (b) there is the slowness-backazimuth plot.*

In figure 5.4 the polar histograms of the slowness-backazimuth results are illustrated separately for the 4 seasons. The color maps are different, in order to evidence the variations within individual diagrams. Active sources from $\sim$ 150°N, having high apparent velocity, are confirmed during Spring-Summer (fig.s 5.4a- b); during Autumn (fig. 5.4c) the most represented incoming direction is $\sim$ 140°N; during Winter (fig. 5.4d) the SM sources are more scattered, as a consequence of more local sources linked to the Winter-storms in the northern-hemisphere.

Because of the selection criteria used in the beamforming analysis, the results associated with individual time windows are always relative to the most coherent signal. As a consequence, the lowest-frequency waves tend to be over-represented as they generally exhibit the largest coherence, thus hindering other possible, higher-frequency signals. For this reason I repeated the analysis over the following 4 frequency sub-bands: 0.1-0.3 Hz (I); 0.3-

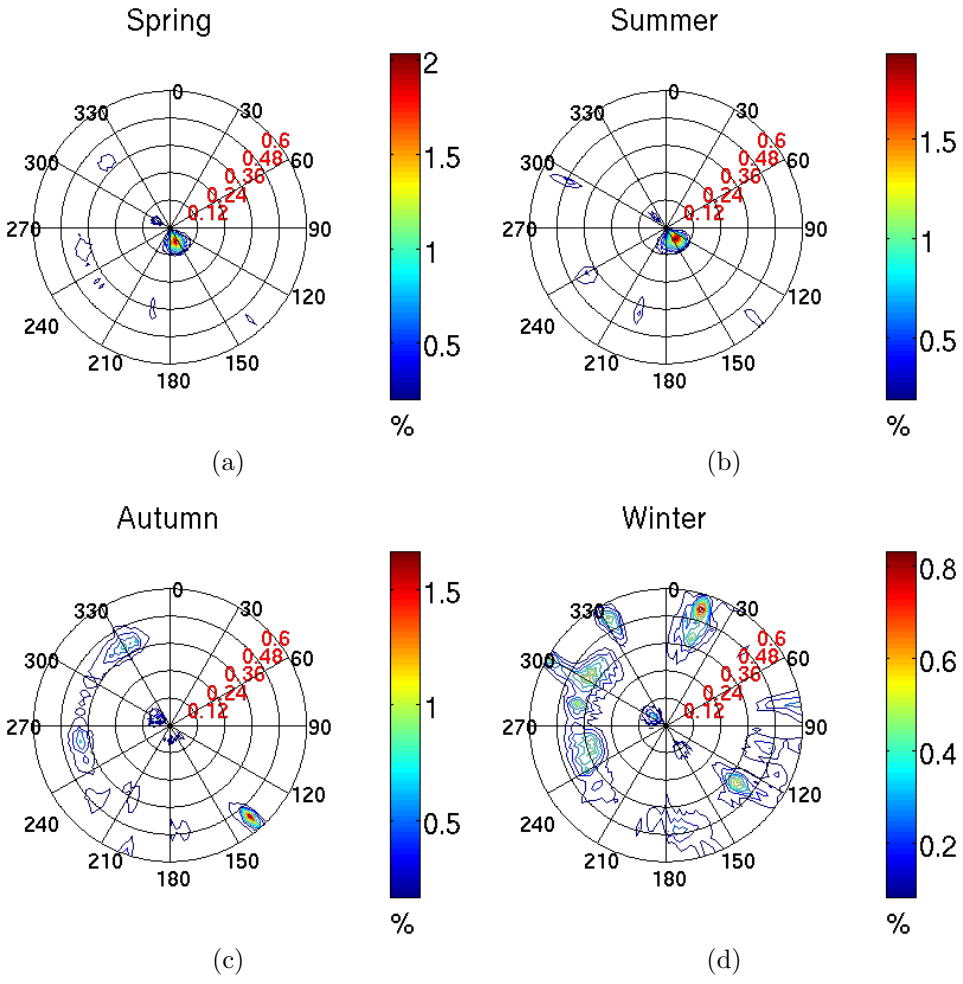

Figure 5.4: *Seasonal polar histograms of the slowness-backazimuth beamforming results of microseisms in the band 0.1-1 Hz. From (a) to (d) there are: Spring, Summer, Autumn and Winter.*

0.5 Hz (II); 0.5-0.7 Hz (III); 0.7-0.9 Hz (IV). The polar histograms of the slowness-backazimuth are presented in figure 5.5. As expected, the slowness-

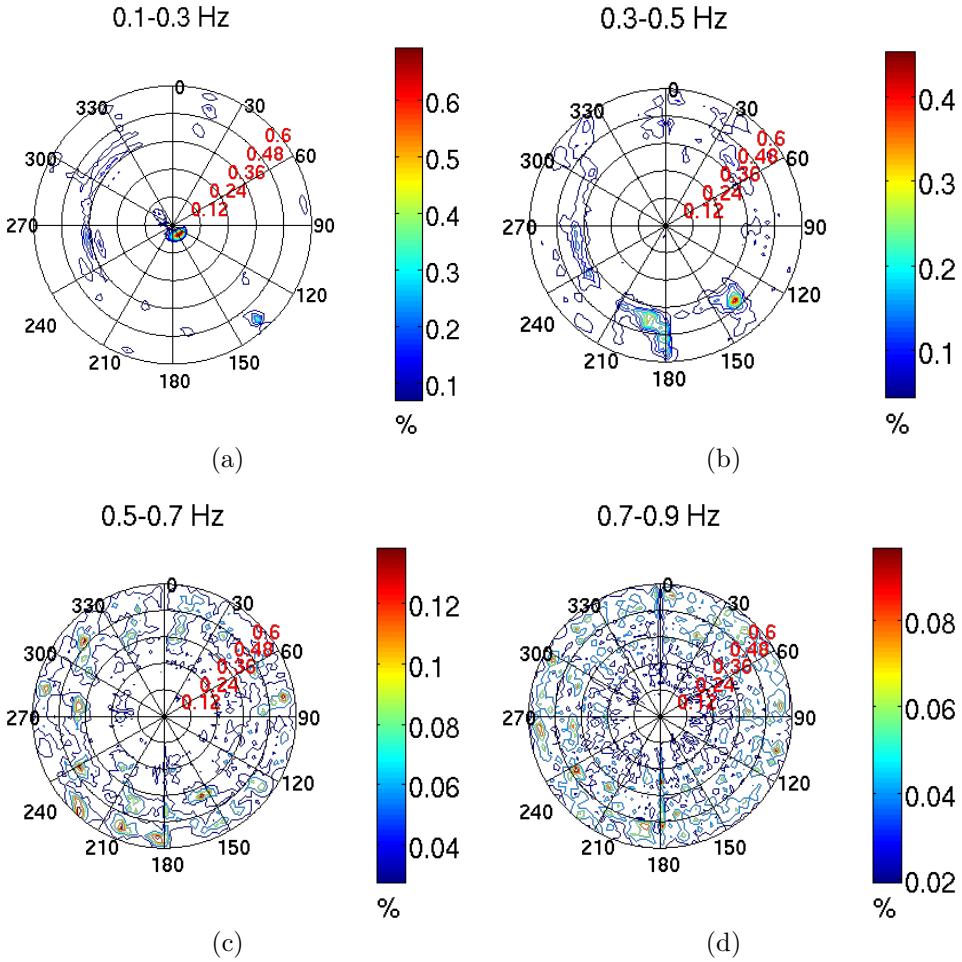

Figure 5.5: *Polar histograms of the slowness-backazimuth beamforming results of SM, computed for 4 different sub-bands. The frequency band is noted on the top of each diagram.*

backazimuth results in the band I (0.1-0.3 Hz) are common to those computed for the entire SM band (figure 5.3b), because it represents the most coherent band of the SM. When the frequency band increases, a scattering of the results is observed, with peak-slowness moving toward higher values. This analysis confirms that the observed waves have velocities compatible with those of Rayleigh surface waves. In the band II (0.3-0.5 Hz) there is a little

prevalence of the back-azimuth 130°N and 190°N, but the results are quite spread in particular when surface-waves slowness is considered (i.e. > 0.3 s/Km). For both the bands III (0.5-0.7 Hz) and IV (0.7-0.9 Hz), the incoming directions are very scattered.

One note should be made on the slowness-grid limit. As explained in chapter 2, the size of the slowness-grid should be selected as a function of the array response at the frequency of analysis, in order to avoid spurious peaks due to spatial aliasing. For the GAPSS array, the slowness-grid size for both the bands III and IV is on the order of ~ 0.2 s/km. For these frequency bands, caution must therefore be taken once considering results which exhibits slownesses greater than the above limit.

Considering the set of measured back-azimuths, it is possible to infer the most probable local/regional sources areas generating the observed SM signals.

Let us consider the measured incoming-directions associated to surface-waves slowness (values > 0.27 s/Km); then overlying the polar histogram of these backazimuths on the map of Europe (see figure 5.6), 8 main areas can be recognized, each associable to a possible source in the Mediterranean area:

- the Balearic Sea-the Marseille Gulf-the coasts of Corsica (1),
- the Genoa Gulf (2),
- the Trieste Gulf (4),
- the coasts of Croatia (5),
- the Gargano promontory-Aegean Sea-the Ionian coasts of Greece (6),
- the South-Eastern Tyrrhenian Sea (7),
- the Sardinia Channel (8).

Following the same directions, the possible generating areas outside the Mediterranean Sea could be:

- the coasts of Galicia-Northern Portugal (1),
- the coasts of Bretagne-South-Western coasts of Ireland (2),
- the Western coasts of Scotland (3);
- the Northern coasts of Scandinavia (4).

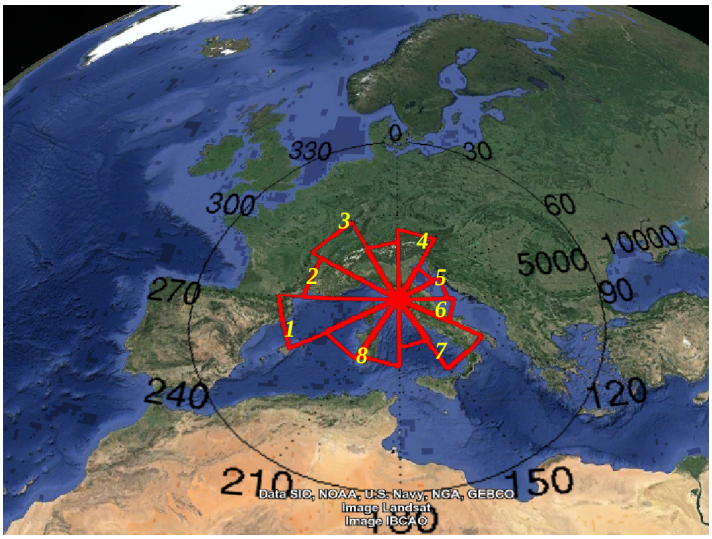

Figure 5.6: *Polar histogram of the main incoming directions associated to surface-wave slowness (> 0.27 s/Km), considering 11 months (May2012-March2013) of observations. The Number are associated to the possible source location listed in the text.*

The main incoming directions of figure 5.6 are then compared to the results from previous studies on SM sources as measured at different sites within Europe. Figure 5.7 (after Marzorati and Bindi (2008)) resumes the results found by early studies (Marzorati and Bindi, 2008; Friedrich et al., 1998; Pedersen and Krüger, 2007). The North Galicia, Menorca and Ireland has been recognized as SM sources by Chevrot et al. (2007), as well. In the study of SM recorded at Hamburg, Essen et al. (1999) also found that preferential generation areas of SM are the coasts of southern Norway and the Atlantic coasts of Scotland and Ireland.

Once compared to these previous studies, the present results allow the identification of a larger number of possible sources, likely resulting from the

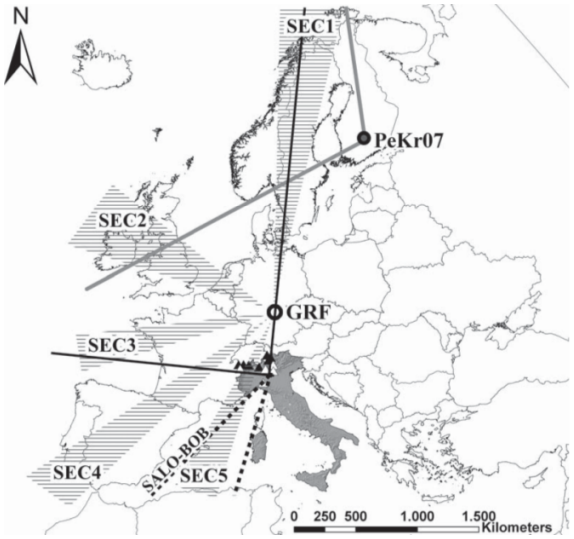

Figure 5.7: *Back-azimuths of main source areas for microseisms recorded in Europe. GRF: SM recorded at Gräfenberg array (Friedrich et al., 1998); PeKr07: SM recorded in southern Finland (Pedersen and Krüger, 2007); dashed and solid black lines: main incoming directions detected from stations in the Alps and Po Plain (Marzorati and Bindi, 2008). After Marzorati and Bindi (2008).*

central position of the GAPSS array with respect to the Mediterranean sea. For instance, the backazimuths reported in figure 5.6 are also suggestive of sources located in the Southern Ionian Sea, in agreement with Brzak et al. (2009) who identified the area of the Gargano promontory as a persistent microseism source.

Summarizing, the SM recorded at the GAPSS array are affected by the seasonal variability of their sources; a further variability is also observed once accounting for different frequency bands. During the Winter-time, backazimuths of the 0.1-0.3 Hz SM are generally more dispersed than those observed during other seasons. At frequencies higher than 0.3 Hz, the SM sources are very scattered, and they are likely related to local storms in the Mediterranean Sea. Following these considerations, it turns out that the stochastic techniques for the analysis of the ambient noise should produce more reliable results once accounting for frequencies higher than 0.3 Hz.

The exact location of the most likely sources of SM excitation is a difficult task, because of i) the continuous variation of ocean wave spectra, ii) the possibility of the source region to be spatially extended, iii) the likely, contemporaneous action of multiple sources (e.g. Longuet-Higgins, 1950; Kedar et al., 2008).

To solve these issues, it greatly helps integrating the seismological observations with punctual sea-state information. The following section thus presents an attempt of location of distinct microseism sources based on the comparison of beamforming results with numerical wave models.

5.1 Example of Source Identification

In this section I present an example of SM source location by comparing the seismic directional data with results from WaveWatch III®(WWIII) numerical models of the Mediterranean sea state. The selected time interval spans the days from March 16, 2013 through March 19, 2013. During that period, the GAPSS recordings exhibited considerable amplitude in the microseism frequency band.

Figure 5.8 shows the vertical-component seismogram and the corresponding spectrogram observed at station TRIF. The SM action is clearly evident as a spindle-shaped amplitude variation lasting almost three days. The beamforming results for the 0.1-1 Hz frequency band are compared to the results of the numerical simulations made available by the Hellenic center for Marine Reasearch Poseidon (http://www.poseidon.hcmr.gr/). In figures 5.11-5.14, the rose diagrams collecting the backazimuths derived from beamforming are compared to the significant wave height predicted by the numerical simulations. Each snapshot is relative to 3 hours of observation/simulation. Overall, the SM backazimuths exhibit a good concordance with the location of the most relevant sources which, during the considered time interval, were mostly located in the southern Mediterranean sea.

Several discrepancies are however observed, and these concern (1) the poor detection of sources located in the Tyrrhenian Sea, and (2) the persistent detection of sources located to the North, which cannot be directly associated

with any Mediterranean source.

These discrepancies can be explained in terms of (i) prediction errors of the numerical simulations, or (ii) interference of waves propagating from different directions, as it is clearly observed in all the snapshots spanning the late portions of day 17 and the whole day 18.

Figure 5.9a illustrates an example of the hourly 2D spectra of the WWIII®, computed for a virtual buoy in Livorno (10.28 E, 43.56 N, see figure 5.9b). The spectrum is relative to the March 19, 2013, at 02:00 UTC time. In this polar diagram the spectral energy density is plotted as a function of the incoming direction and the peak frequency of waves. Data were provided by the Consorzio LAMMA-Regione Toscana.

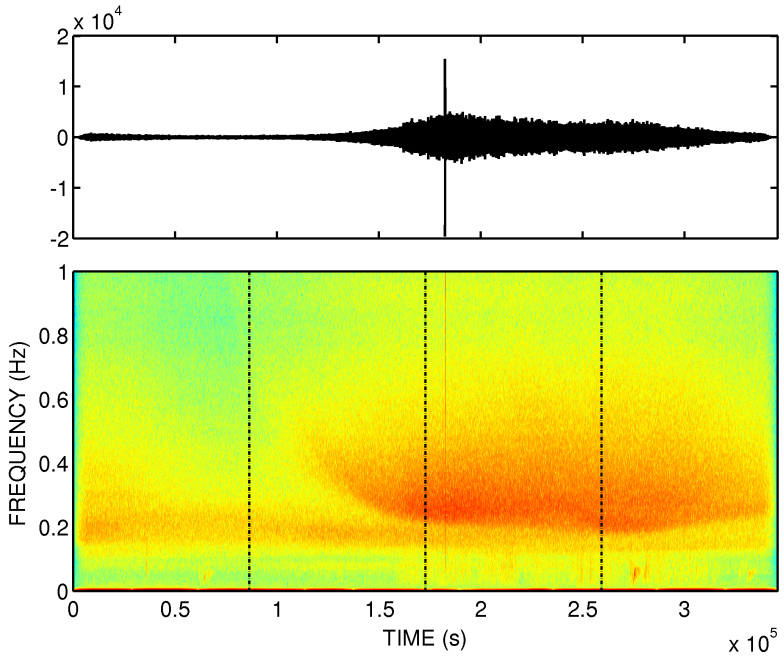

Figure 5.8: *Vertical-component seismogram and the corresponding spectrogram observed at station TRIF for the days 16-19 March 2013.*

Figure 5.10 illustrates a detail of the vertical component spectrograms at stations TRIF (figure 5.10a) and LA03 (figure 5.10b), compared to the significant wave heights, direction and frequency predicted by the WWIII®

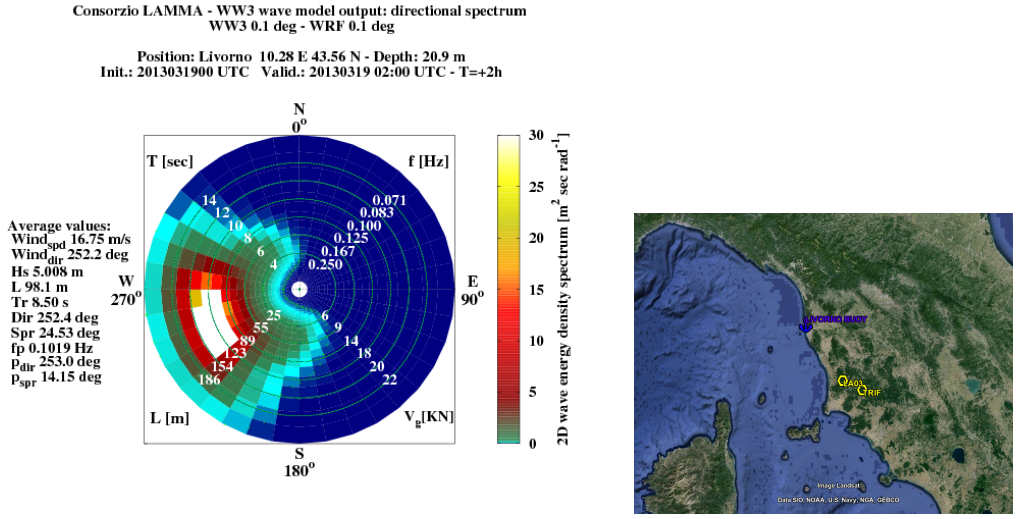

(a) (b)

Figure 5.9: *WWIII® models for the day 19 March 2013. (a): WWIII® 2D spectrum computed for the Livorno-buoy at 02:00 UTC (provided by Consorzio LAMMA-Regione Toscana); (b) : map of the positions of the Livorno-buoy and the GAPSS stations TRIF and LA03; .*

simulations.

The black dots on the spectrogram (figure 5.10) are the maxima for each time window, while the blue solid line is the linear interpolation of them.

The values of the predicted wave peak frequency have been first doubled and then plotted on the spectrogram, as a green solid line. A good agreement is found between the spectrogram maxima and the doubled peak frequency of the waves, at least in the first third part of the day. This is in rough agreement with the beamforming results, whose backazimuths distribution point to energetic sources in the Tyrrhenian sea, at least for the first 6 hours of the day.

This simple example provided a pictorial view about the previously-stated properties of the SM wavefield observed at GAPSS. In addition, it also highlighted the complexity of SM signals, which results from a combination of distant and local sources acting contemporaneously. The quantitative location of these sources for deriving seismic-based information on the wave climate would thus require the use of multiple arrays, and incorporation of

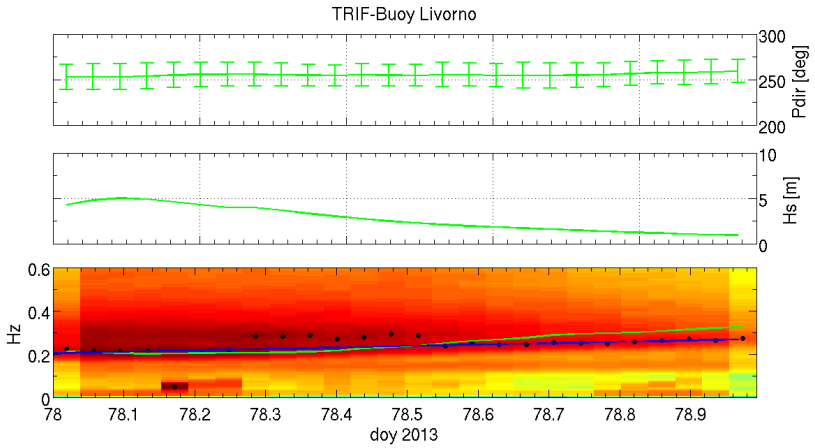

(a)

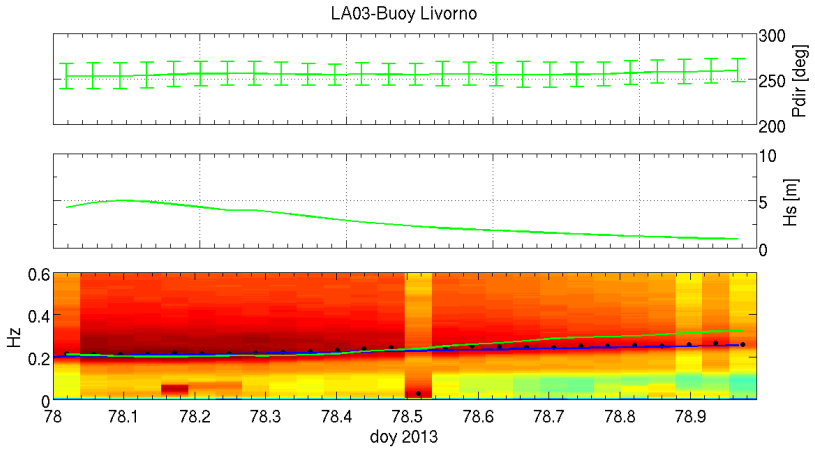

(b)

Figure 5.10: *Comparison between vertical component spectrogram of stations TRIF (a) and LA03 (b) and the hourly-mean WWIII® outputs computed for the Livorno-buoy position, for the day 19 March 2013. The WWIII® outputs are green solid curves, representing the mean direction of the peak-energy waves (Pdir, top charts), the mean significant wave height (Hs, middle charts), and the doubled peak frequency of the waves (plotted on the spectrograms). The black dots on the spectrograms are the maxima for each time window, and the blue solid line is the linear interpolation of them.*

amplitude decays from distributed network. These efforts should provide enough constraints to separate the contributions of these sources of similar frequency which radiate energy simultaneously.

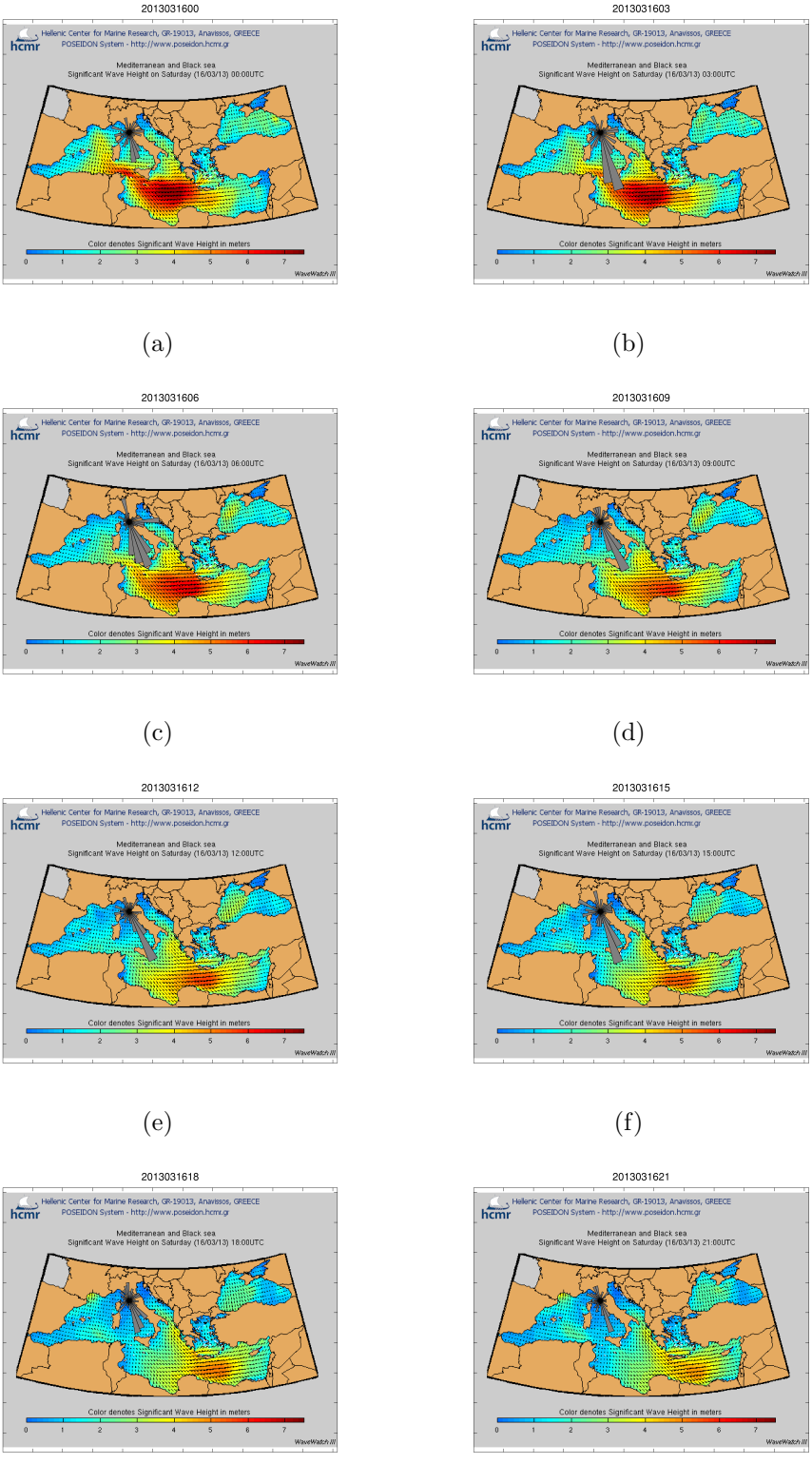

(a) (b)

(c) (d)

(e) (f)

(g) (h)

Figure 5.11: *Rose-diagram of backazimuths retrieved from beamforming compared with WWIII-significant wave height (Hs) Mediterranean maps (from poseidon.hcmr.gr), for the day March 16, 2013. The time interval between subsequent diagrams is 3 hours.*

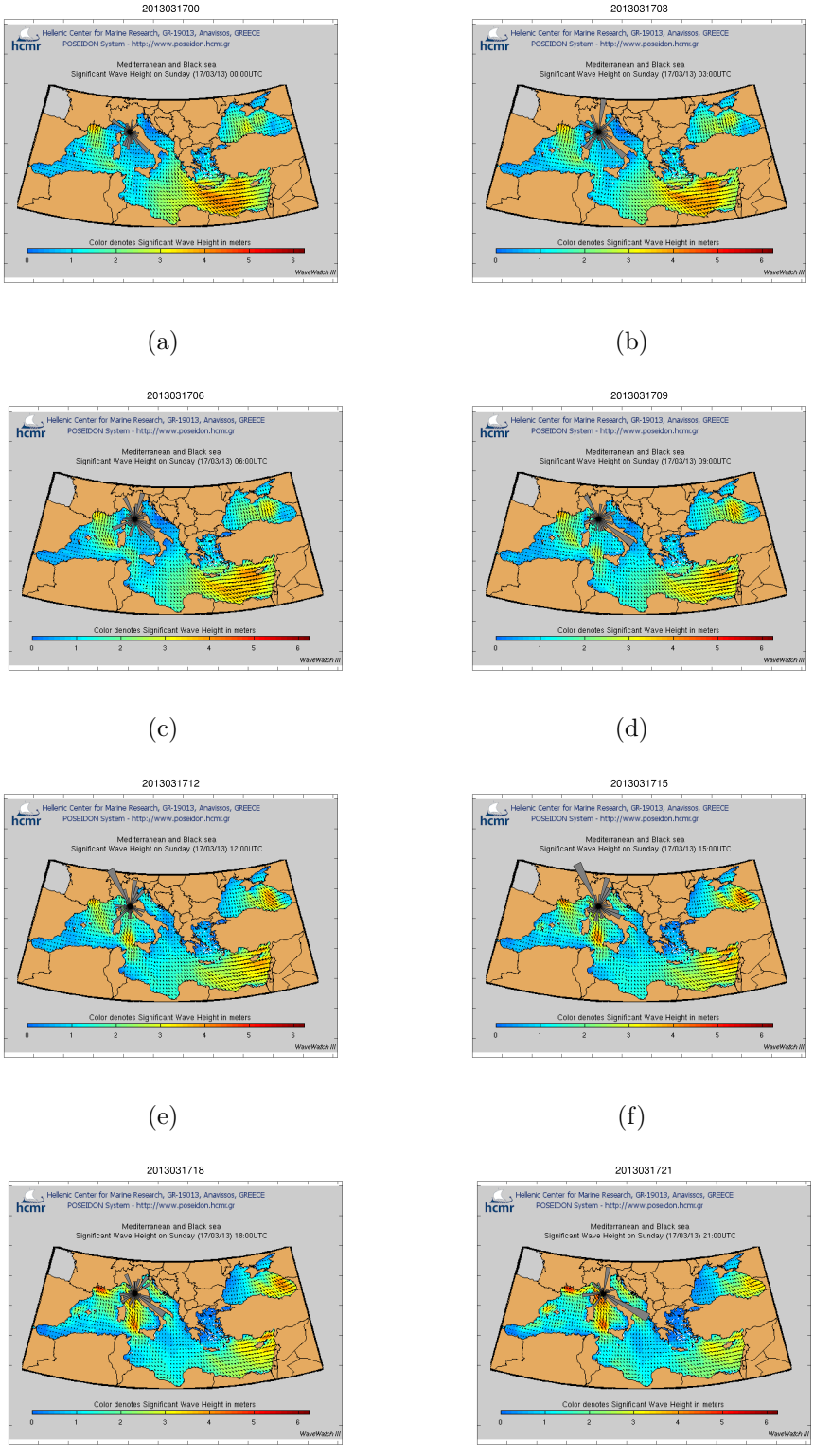

(a) (b)

(c) (d)

(e) (f)

(g) (h)

Figure 5.12: *Rose-diagram of backazimuths retrieved from beamforming compared with WWIII-significant wave height (Hs) Mediterranean maps (from poseidon.hcmr.gr), for the day March 17, 2013. The time interval between subsequent diagrams is 3 hours.*

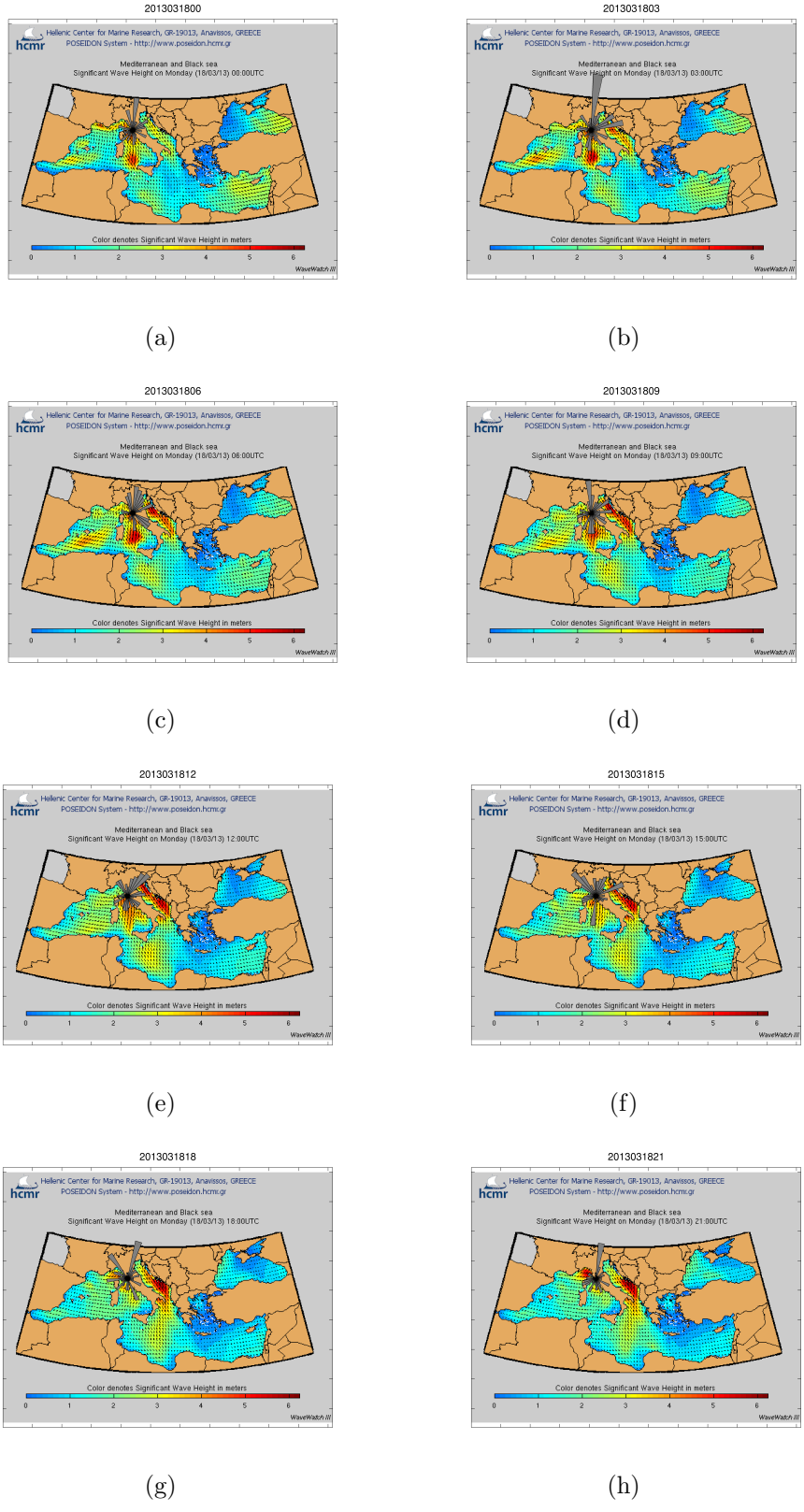

(a) (b)

(c) (d)

(e) (f)

(g) (h)

Figure 5.13: *Rose-diagram of backazimuths retrieved from beamforming compared with WWIII-significant wave height (Hs) Mediterranean maps (from poseidon.hcmr.gr), for the day March 18, 2013. The time interval between subsequent diagrams is 3 hours.*

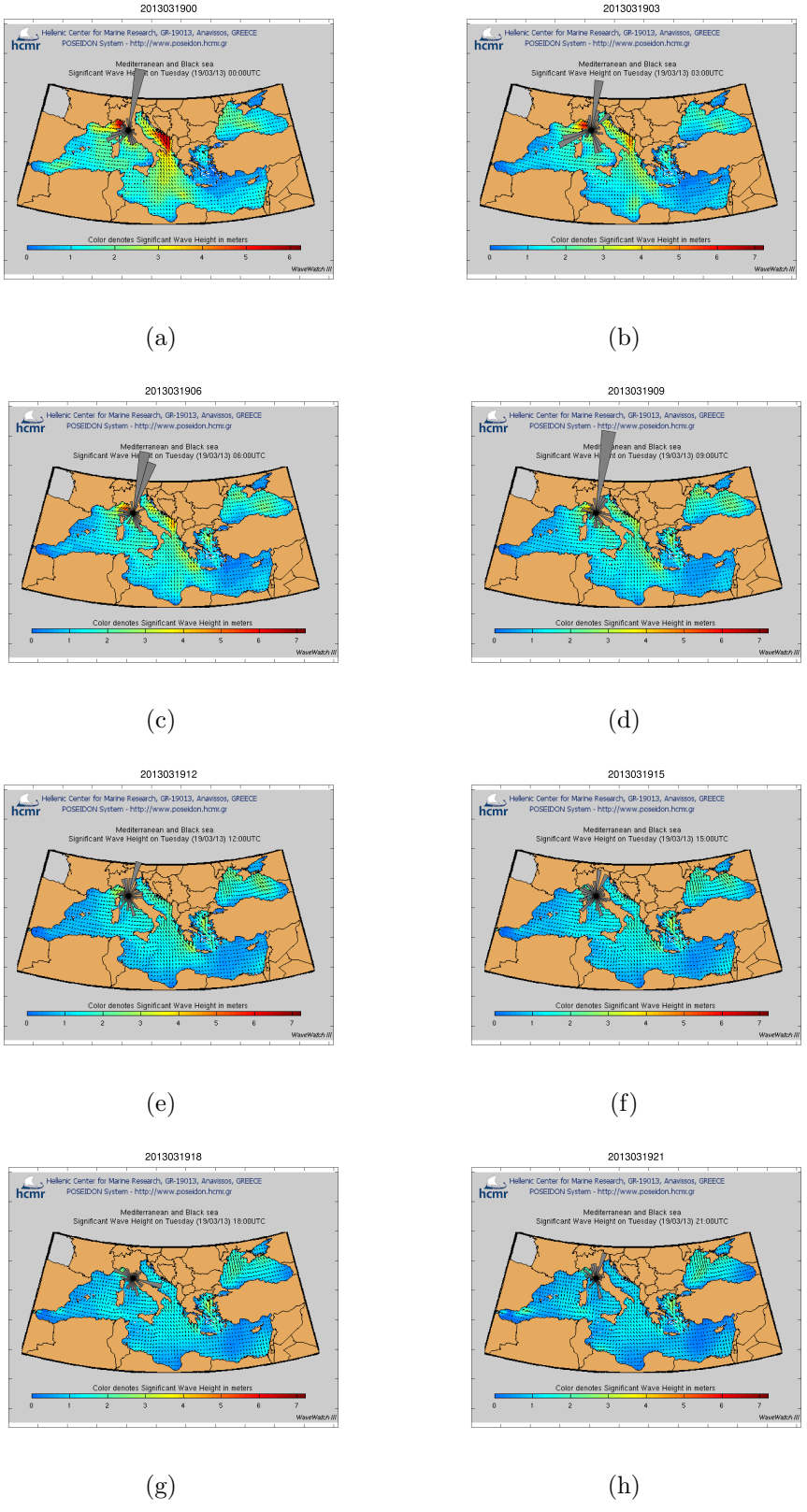

(a) (b)

(c) (d)

(e) (f)

(g) (h)

Figure 5.14: *Rose-diagram of backazimuths retrieved from beamforming compared with WWIII-significant wave height (Hs) Mediterranean maps (from poseidon.hcmr.gr), for the day March 19, 2013. The time interval between subsequent diagrams is 3 hours.*

Chapter 6

Green's Function and S-wave Profiles from Secondary Microseisms at the LTGF

In this chapter I present the results from application of the seismic ambient noise stochastic techniques at LTGF. I show the empirical Green's functions retrieved in time domain using the NCF, and compare the measured velocity dispersion curves with those obtained with SPAC. Then, I show examples of S-wave velocity profiles derived from the inversion of those dispersion curves, and compare the results with the available, independent data for the study area. A discussion about the ability of the two approaches to resolve the most relevant features terminates the Chapter.

The analyses regarding the location of SM sources, presented in chapter 5, evidence that the wave-field -though exhibiting a broad range of incoming directions- is not fully diffusive. Under that condition, several authors (e.g. Ruigrok et al., 2011; Mordret et al., 2013) suggest to apply a back-azimuth filter prior to the computation of NCF, taking into account only those station pairs which are aligned to the main incoming directions of the noise wavefield. This is done since an heterogeneous distribution of sources may result in biased GF reconstruction (e.g. Stehly et al., 2006). In the case of GAPSS

array, the majority of station-pairs is favourably oriented with respect to the main incoming directions of the microseisms, that are 240-330°N and 120-200°N. Following the arguments reported in the previous chapter, the most reliable results in the stochastic analysis are then expected for the frequency band 0.3-1 Hz.

6.1 NCF: from Green's Functions to Group Velocity Dispersion Curves

The Noise Cross-correlation Function (NCF) technique, as described in details in section 3.2, was applied to all the vertical-component data of the available GAPPS station pairs, for the timespan May2012-March2013. The time window used was 600 seconds long, and all the time windows encompassing recognized earthquakes ((Saccorotti et al., 2014)) were discarded. Prior to overall stacking, individual NCFs were stacked on a daily base to investigate their possible temporal variations.

In figure 6.1 the daily-stacked cross-correlation functions for the station pair LA07-LA12 (oriented $\sim$ 200°N) are arrayed along the ordinates axis, and the top green function is the overall stack (261 days), whose negative time derivative should correspond to the eGF for that specific sites pair. Positive lag times indicate propagation from station LA12 to station LA07, i.e. toward the N20E°direction. The first feature emerging from that figure is the stable arrival at 9.2 seconds. The dispersion of this signal is evidenced in the band-pass filtered overall stack shown in figure 6.2, where it appears as a progressively-delayed wave-packet for the NCF filtered over frequency bands $\geq 0.3 - 0.5$ Hz. Horizontal velocities of this pulse are in between 1.5 and 2 Km/s, thus matching the beaforming results presented in figure 5.5b. Another feature, confirming earlier results about the deterministic analysis, is the main arrival at zero-lag. Though it appears to dominate the broad-band (0.1-1 Hz) NCF, its contribute disappears at frequencies above 0.3 Hz. As also suggested by the beamforming results, the near-zero-lag arrival indicates high apparent velocities, i.e. waves impinging at the array almost vertically.

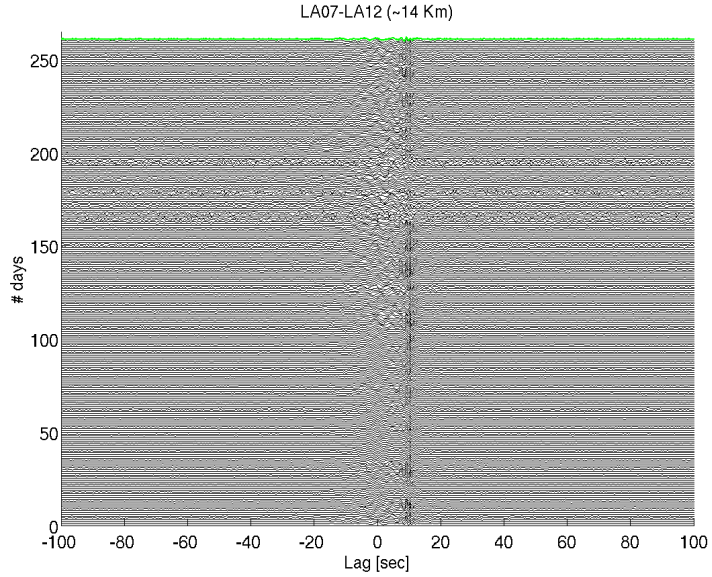

(a)

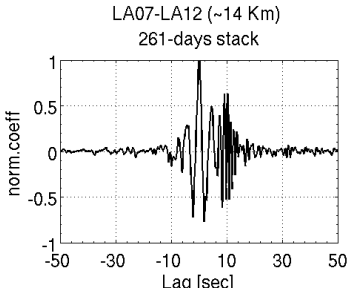

(b)

Figure 6.1: *Daily stacked NCFs spanning May2012-March2013 (261 operative days), for the station-pair LA07-LA12 arrayed vertically (a); the top green function is the stacked function of the 261 days below, and its zoom is in (b). The amplitudes are normalized for each trace.*

Taking into account the information about the incoming directions of the SM waves whose apparent velocity is compatible with that of surface waves (chapter 5), I selected two groups of station-pairs whose azimuths were roughly perpendicular: 240-300°N (AZ1) and 150-210°N (AZ2). For the two groups, I then stacked all the available NCFs, discarding station pairs with less than 30 operative days. After the computation of the eGFs,

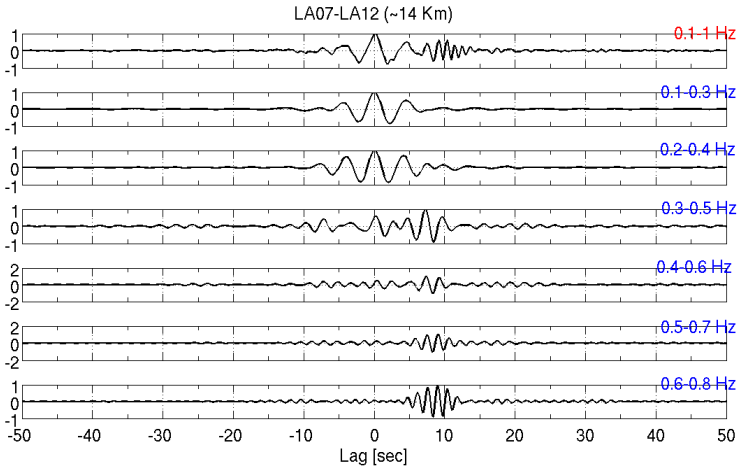

Figure 6.2: *The normalized stacked NCF of figure 6.1b (shown on the top) filtered in 6 frequency-bands encompassing the SM band 0.1-1 Hz. The bands are shown on the right of each filtered trace.*

these were then filtered in two different frequency-bands: 0.1-0.3 Hz(F1) and 0.3-0.5 Hz(F2). The results can be found in figures 6.3 and 6.4 for the AZ1 and AZ2 azimuthal groups, respectively. The auxiliary diagrams (6.3c-d and 6.4c-d) report the inter-station distances plotted against the lag-times associated with the maximum of each individual correlation function. For the F1 frequency band, the near-zero-lag maxima predominate, mostly for the pairs of the group AZ2. The group AZ1 also shows apparent velocities $\sim$ 2.6 Km/s, indicating the contemporaneous incidence of signals with different velocities and hence sources. These features matches the results of beamforming for this frequency band, which were summarized in figure 5.5a. Over the F2 frequency band, all the retrieved eGFs are markedly asymmetric, and their maxima are all at positive lag-times, indicating direction-of-arrivals from the West (AZ1) and South (AZ2) quadrants. The apparent velocities are compatible with surface waves, being $\sim$ 2.5 Km/s for AZ1 and $\sim$ 3 Km/s for AZ2. Again, these results are in agreement with what previously derived from the beamforming analysis.

The minimum number of stacking days, for which one can retrieve reliable eGFs, is an important information for the NCF applications. Following the previously discussed seasonal variability of the microseism wavefield, I then

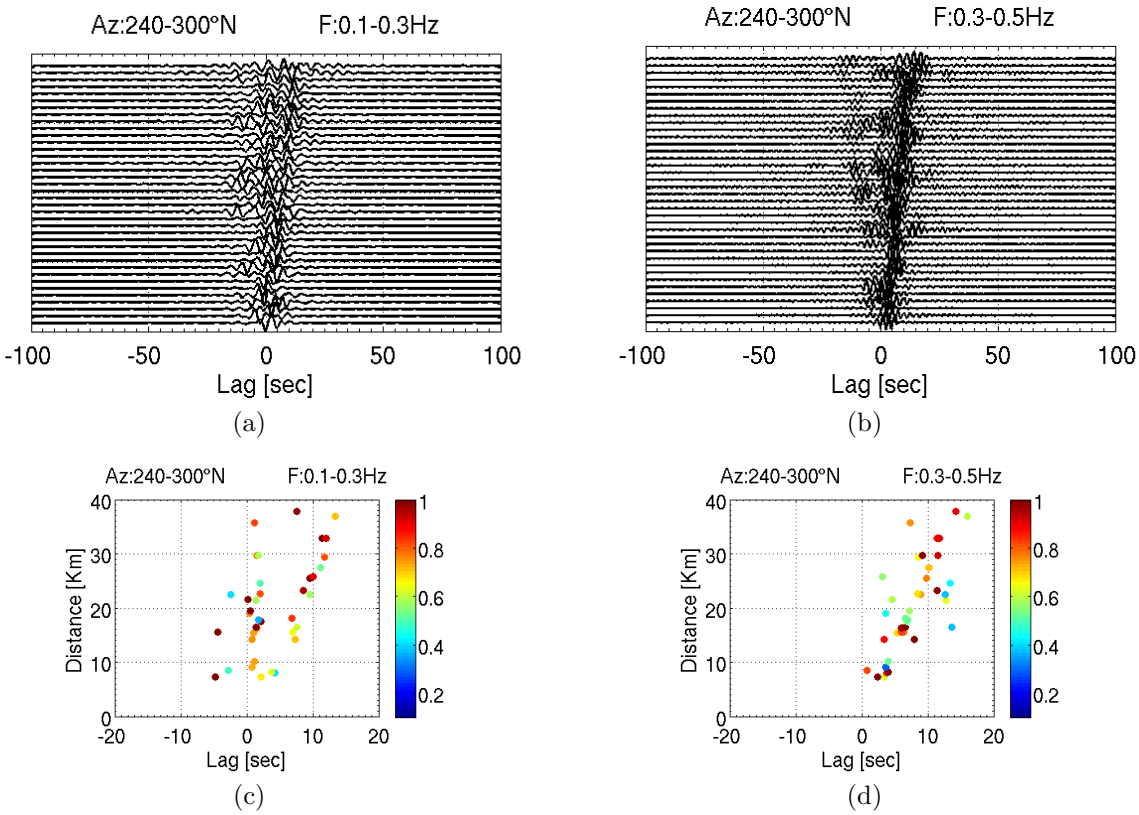

Figure 6.3: *Emprirical GFs for the GAPSS station-pairs oriented 240-300°N (AZ1). The functions are sorted by distance (increasing toward top) and filtered in the band 0.1-0.3 Hz (a) and in the band 0.3-0.5 Hz (b). Diagrams in (c) and (c) are the normalized maxima (for each function) of the eGFs plotted versus lag-time and distance of the pairs.*

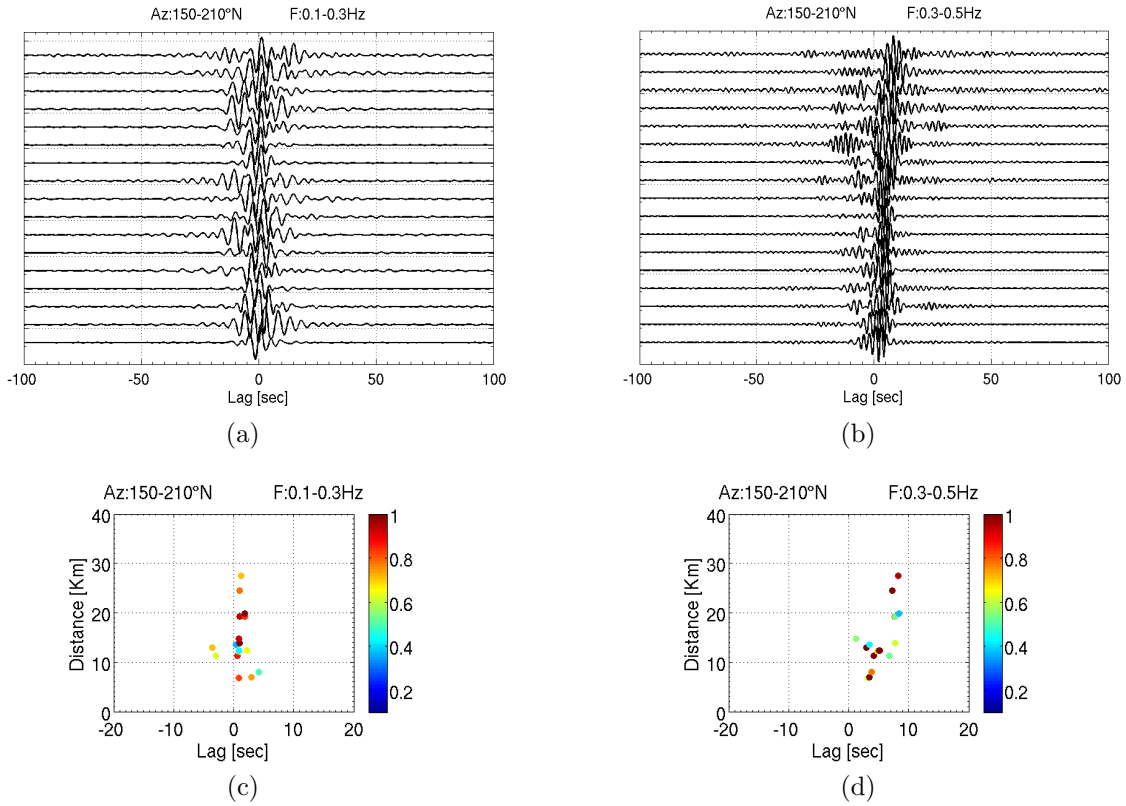

Figure 6.4: *Emprirical GFs for the GAPSS station-pairs oriented 150-210°N (AZ2). The functions are sorted by distance (increasing toward top) and filtered in the band 0.1-0.3 Hz (a) and in the band 0.3-0.5 Hz (b). Diagrams in (c) and (c) are the normalized maxima (for each function) of the eGFs plotted versus lag-time and distance of the pairs.*

examined the differences between sample NCFs calculated over stacking periods of different lengths.

Figure 6.5 provides the correlation values (R) between the 11-months stacked eGF and the eGF stacked over increasing number of days, for two station-pairs chosen to be oriented East-West (FROS-LA03,total operative days: 214) and almost North-South (LA07-TRIF, total operative days: 229). This diagram shows that the 30-days stacked eGF optimally (R¿0.8) reproduces the long-term stacked function, and a great stability is found for pair oriented N-S. However, if one consider the 11-months stack the reference measure, the eGF stabilizes only after 180 stacking days.

In order to investigate whether the seasons influence the eGF reconstruction, figure 6.6 shows the correlation values (R) between the eGF derived from stacking the overall data set, and those obtained after seasonal and 30-random-days stacks. The R value is evaluated for the same station-pairs of figure 6.6. From this diagram, two important observations emerge:

- with the exception of the winter period, the eGF retrieved from 11-months spanning data can be optimally approximated by seasonal stacks,
- a 30-random-days stack provides results very close to those relative to the stack over the entirety of the data set.

The SNR of the NCF is measured to quantify the emergence of the GF as a function of averaging time and inter-stations distance (see section 3.2.2). Figure 6.7 shows the average and standard deviation of SNR among all the GAPSS station-pairs as a function of the day of the year (DOY) 2012 (the days from January to March 2013 are summed to the DOYs of 2012). The first observation is that the SNR is always higher than the threshold (15 dB) considered in literature for accepting an eGF measure (e.g. Bensen et al., 2008). The drop of SNR during the month of November (from DOY 300) is probably due to the malfunctioning of some stations of the array, thus limiting the number of measurements during this month.

Figure 6.8 shows the SNR versus inter-station distances; data are well fitted by the exponential function $y = ae^{bx}$.

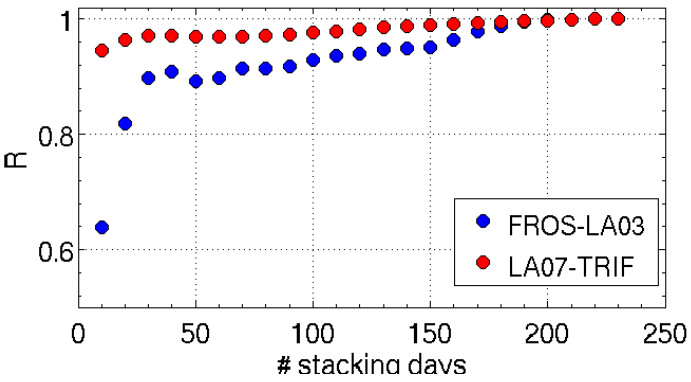

Figure 6.5: *Correlation (R) of the eGF retrieved by 11-months data and eGF provided by stacks of increasing number of days. The value of R was computed for two perpendicular station pairs.*

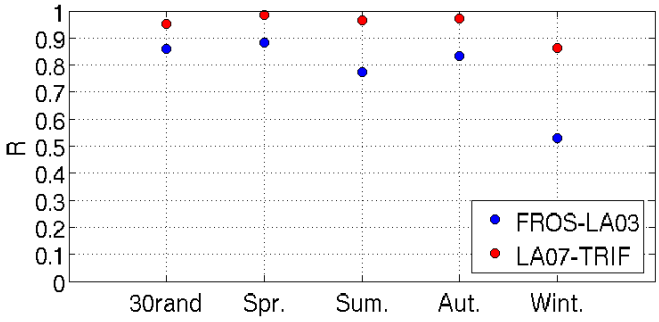

Figure 6.6: *Correlation (R) of the eGF retrieved by 11-months data and eGF provided by 30-random stacking days and seasonal stacks. The value of R was computed for two perpendicular station pairs.*

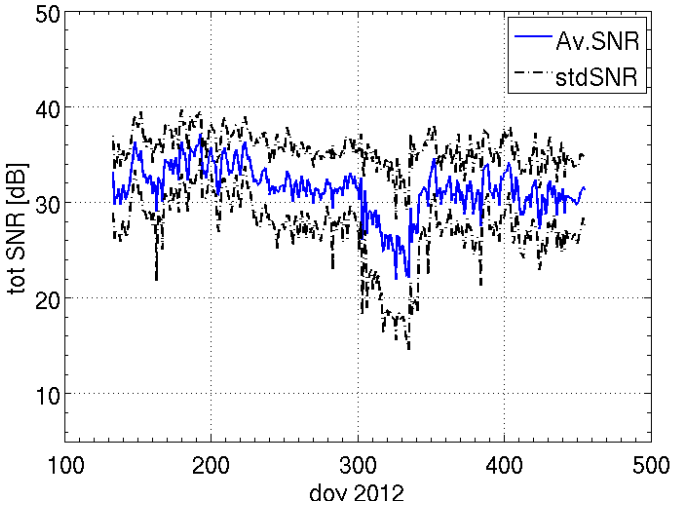

Figure 6.7: *Average, among all the GAPSS station-pairs, and standard deviation of the SNR versus time, spanning 11 months (May2012-March2013). Time is in day of the year 2012, and the days of 2013 are presented as a tail of the 2012.*

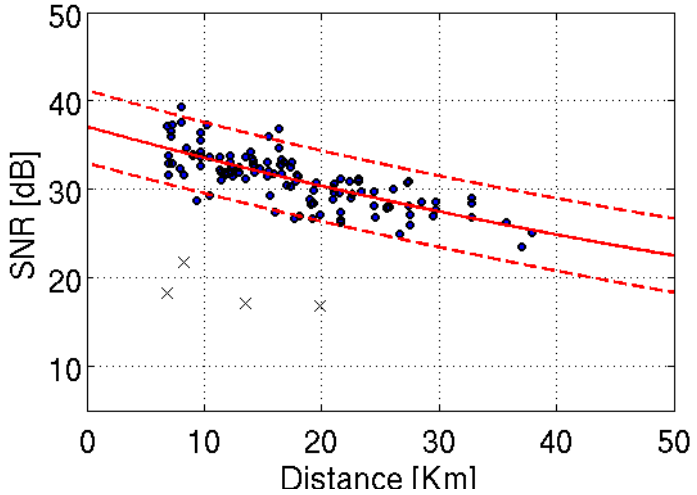

Figure 6.8: *SNR of the eGF spanning 11 months versus inter-station distance. The solid red curve is the fitting function $y = ae^{bx}$, with a=36.8 and b=-0.0097, with a root mean squared error RMSE=0.5865. The dotted red curves are the 95% prediction bounds. The cross symbols are data considered outliers in the fitting.*

Figure 6.9 shows the SNR, averaged among all the GAPSS station-pairs, versus the number of stacking days. Confirming what is shown in figure 6.6, significantly high (> 40 dB) SNR is achieved after just a 30-day-long stacking interval. As the number of stacking days increase, the SNR increases as well, but this trend is slower than that predicted by the squared root function reported in literature (see section 3.2.2). For our data, the fitting function is $y = ax^{1/b}$, with a a root mean squared error RMSE=0.92.

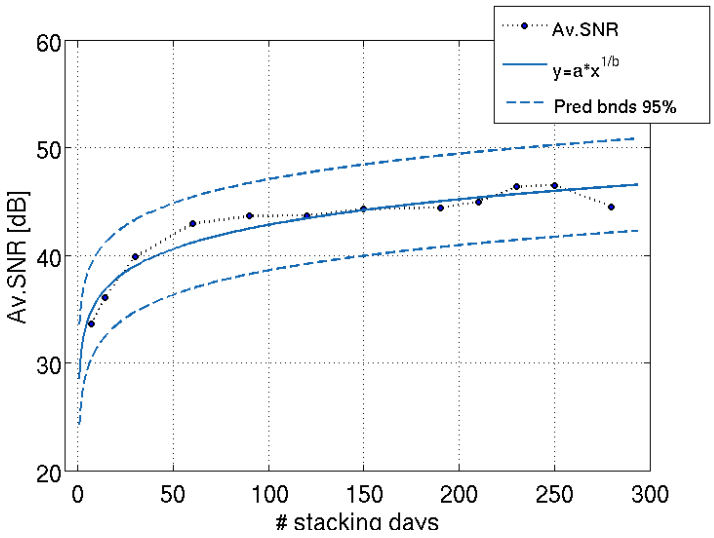

Figure 6.9: *Average SNR, considered as a random variable, as a function of the number of stacking days. The blue curve is the fitting function $y = ax^{1/b}$, with a=29.95 and b=12.89, with a root mean squared error RMSE=0.92. The dotted blue lines are the 95% confidence bounds.*

Once the eGF are retrieved from the stacked cross-correlation functions, the estimate of the group velocity dispersion curve is performed by FTAN analysis (see section 3.2.3). The chosen FTAN parameters for the Gaussian filters were:

- half relative frequency band $HB = 0.3$
- $\alpha = 25.6$

For the dispersion measurements I considered the eGF evaluated from NCFs stacked over the entire time interval; FTAN is performed for all the

available station-pairs, then by means of the error analysis and the selection criteria described in section 3.2.4, only the most reliable measurements are retained.
Figure 6.10 shows examples of FTAN maps for station-pairs at different orientations. For each frequency bin, maxima of the FTAN maps (black diamonds) should correspond to samples of the fundamental mode of the group-velocity dispersion curve. Not all the sampled velocities can be considered valid. First, the minimum reliable frequency is that corresponding to wavelengths larger than 1/3 of the inter-station distance (see section 3.2.4). Second, strong velocity jumps are not realistic (see for instance figures 6.10e and 6.10b at frequencies between 0.9-1 Hz).

Mode mixing can occur when the fundamental mode is contaminated by the overtones, as a consequence of velocity structures characterized by velocity inversions. Such unwanted mode-mixing can lead to marked errors by the time of inverting the dispersion curves for a velocity model; such problem could be overcome by performing a multimodal inversion of surface waves (e.g. Socco et al., 2002; Maraschini et al., 2010). In this thesis the fundamental mode selection was performed, leaving the multimodal inversion for future analysis.

After the selection of the reliable part of the measured group velocities dispersion curves (GVDC), further selection criteria are applied, on the basis of the standard deviation (STD) of the measurements and the SNR. Details about error analysis are reported in section 3.2.4. Those station-pairs that do not respect the STD and SNR conditions are discarded. Figure 6.11 illustrates a summary of the error analysis operated for the GAPSS array data. This figure shows, in their dependence on frequency, (i) the average STD of the group velocity dispersion measurements, (ii) the number of the group velocity measurements that passed the selection criteria, and (iii) the average SNR for all the accepted measurements.

It emerges that:

- no measurements were accepted for frequencies lower than 0.25 Hz, and the largest number of measurements is associated with the 0.5-1 Hz frequency band;

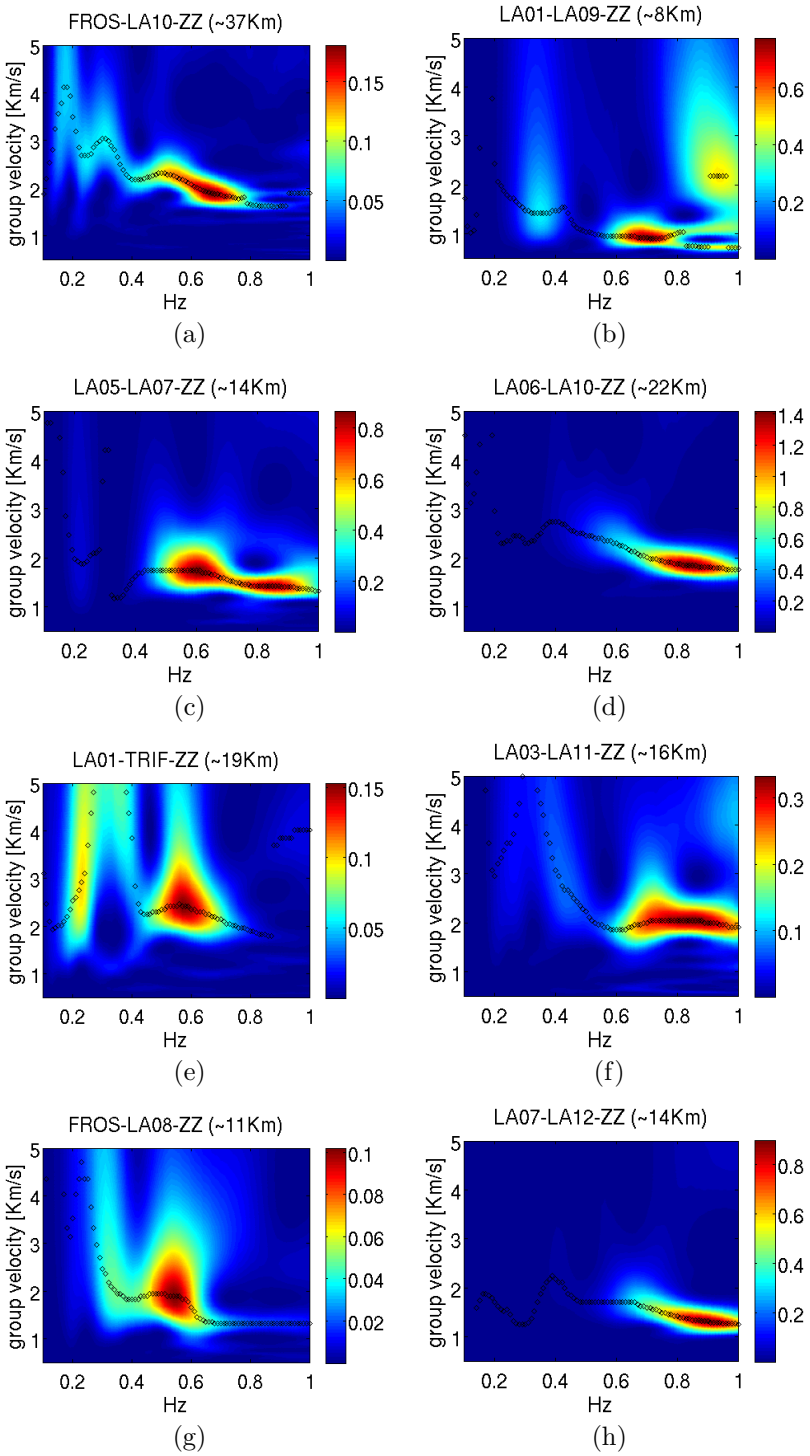

Figure 6.10: *Graphical representation of FTAN applied to station-pairs of the GAPSS array. Each row is relative to different average-orientation of the pairs, which are (from top to bottom): E-W, NE-SW, NW-SE, N-S. For the location of the stations please refer to figure 4.3. The name of the pairs and their range are indicated on the top of each figure. The black diamonds are the maxima of the map at each frequency.*

- the average STD is lower than 100 m/s for frequencies higher than $\sim$ 0.3 Hz,
- the SNR value is always greater than 30 dB for the entire frequency band.

Consequently, the dispersion measurements in the frequency band 0.3-1 Hz result robust. The low number of measurements at frequencies lower than 0.5 Hz is mainly due to the small inter-station distance of the GAPSS array.

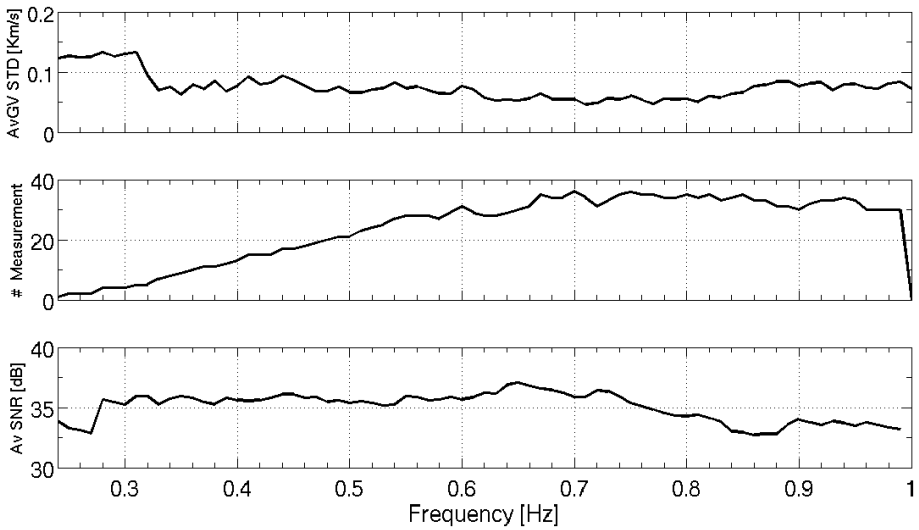

Figure 6.11: *Error analysis of the surface wave group velocity dispersion measurements, showing the averaged values between all station-pairs that passed the selection criteria. All the variables are in function of the frequency. From top to bottom: average STD of the dispersion measurements, number of the accepted measurements, average SNR.*

After application of the selection criteria, 36 GVDC were accepted out of the initial 78.

6.2 SPAC: Phase Velocity Dispersion Curves Selection and Results

This section describes the results from the application of the modified SPAC method to the GAPSS array data. This frequency-domain technique is used

to measure phase velocity dispersion curves (PVDCs), also allowing wavelengths which are longer than the station spacing. The detailed description of the method can be found in section 3.3.

I computed the complex coherence $\gamma(\omega)$ for all the independent station pairs, through multiplication of spectra obtained over 600-seconds-long, non-overlapping time windows. Then, the $\gamma(\omega)$ were stacked throughout the entire timespan having first discarded, as in the case of NCF, all those time-windows encompassing an earthquake. As a consequence, the dataset of $\gamma(\omega)$ is the same used for the NCF, except that the cross-correlation functions are preserved in the frequency domain. For this reason, the discussion about i) stability of the cross-correlation functions, ii) minimum stacking days, and iii) seasonal variability, presented in section 6.1, are still valid.

The last step consists in the inversion for phase velocities $c(\omega)$ of the stacked $\gamma(\omega)$ functions. In a first approach, I used the procedure proposed by Ekström et al. (2009) (section 3.3.4) which consists in equating the zero-crossing of the real part of $\gamma(\omega)$ to the zero-crossings z_n of the zeroth order Bessel function of the first kind $J_0\left(\frac{\omega}{c(\omega)}r\right)$ (r is the inter-station distance). If the difference between phase velocities derived for zeros crossings associated with the up-going and down-going portions of $\gamma(\omega)$ exceeds 300 m/s for more than 3 occurrences, the measurement for that station-pair is discarded. Extra and or missed zeros are allowed, but only the most realistic phase velocity dispersion curve are considered.
Figure 6.12 shows examples of the complex function $\gamma(f)$ (here ω has been substituted by $f = \omega/2\pi$) and the estimated PVDC for station pairs oriented differently.

In this figure, the zero-crossings of the real part of $\gamma(f)$ are marked by red triangles, and the black line connecting them is the estimate of the PVDC. The reference for the phase velocities estimations, is a PVDC obtained from forward computation [1] given a velocity model based on deep wells data crossed by two-way travel time seismic profiles (details in table

[1] The forward computations of dispersion curves (both phase and group) are performed by means of the *gpdc*©software tool of the Geopsy.org software package.

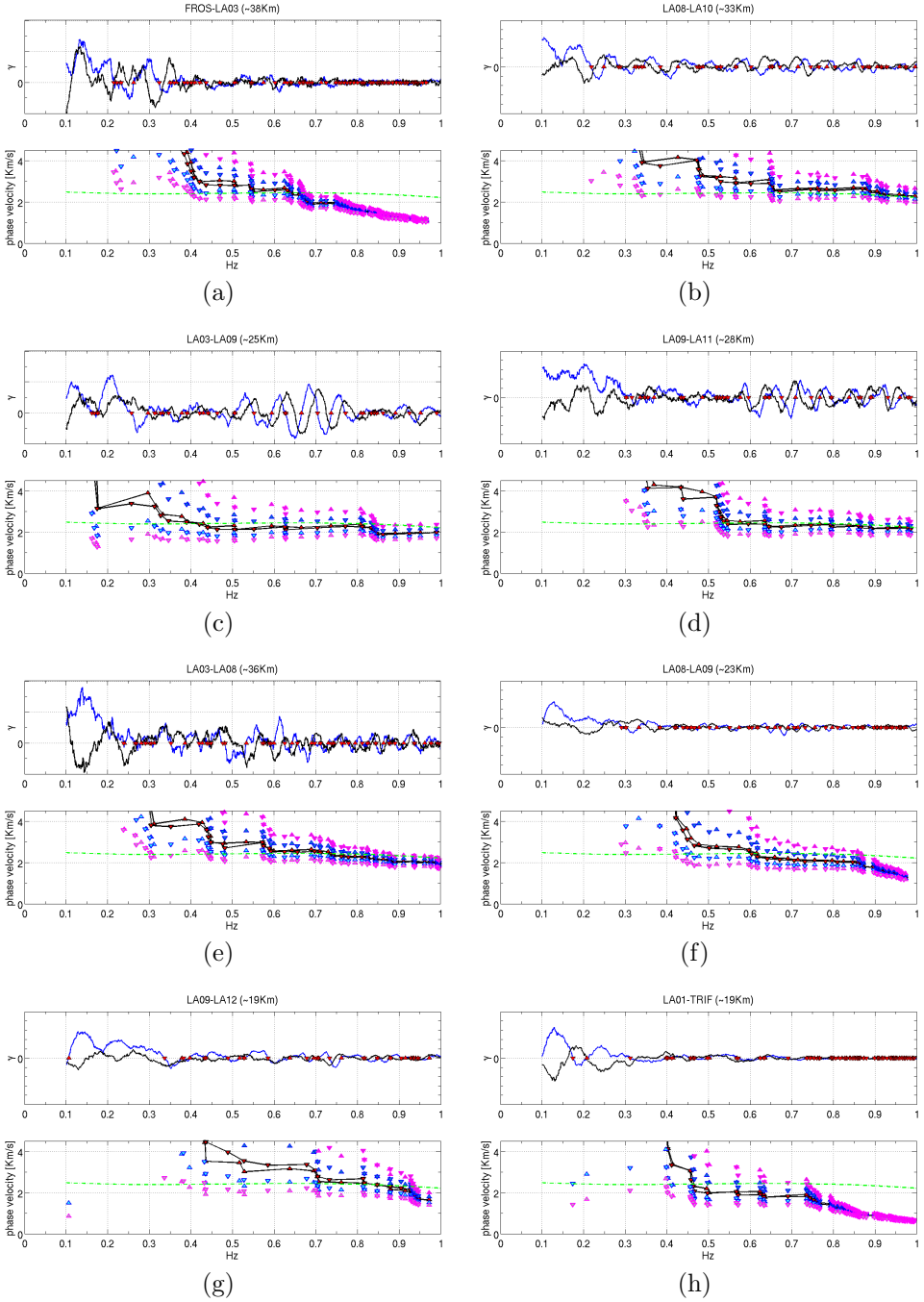

Figure 6.12: *Complex coherence functions $\gamma(f)$ (blues curves are real part, black curves are imaginary part) and phase velocity estimation in frequency domain, applied to station-pairs of the GAPSS array. Each row is relative to different orientations of the pairs, which are (from top to bottom): E-W, NE-SW, NW-SE, N-S. For the location of the stations please refer to figure 4.3. The name of the pairs and their range is indicated on the top of each figure. Dispersion curves are derived from the zeros-crossing of the real part (red triangles connected by black lines). Upward triangles are zeros from negative to positive, downward triangles are zeros from positive to negative. Blue triangles are for 1 missing (light blue) and extra (dark blue) zeros; pink triangles are for 2 missing (light pink) and extra (dark pink) zeros. The dashed green curve is a reference dispersion curve computed from LTGF velocity model based on deep wells data.*

6.1 and figure 6.13).

THICKNESS	**Vp [m/s]**	**Vs [m/s]**	**DENSITY [Kg/m^3]**
100	1600	950	2000
700	3500	2060	2571
1000	6000	3500	2571
300	5700	3350	2571
370	4500	2600	2571
500	3600	2050	2500
∞	4700	2700	2650

Table 6.1: *Layered 1D earth model Model for LTGF. Vp and thickness information is extracted from two-way travel time seismic profiles and deep wells data (Bertani et al., 2005). Density values are considered after Accaino et al. (2005). Vs is computed from Vp considering Vp/Vs average estimates published by De Matteis et al. (2008).*

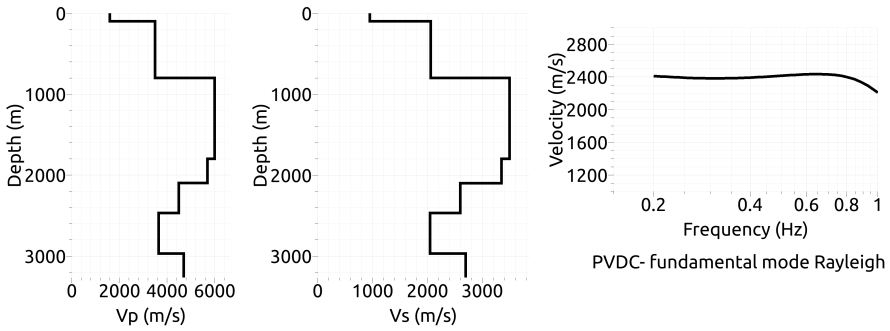

Figure 6.13: *Layered 1D earth model and predicted PVDC for LTGF. Details on the reference velocity model are given in table 6.1.*

The first consideration is that the imaginary part of the complex spectrum is nonzero. This is a consequence of the non-symmetry of the correlation function in time, and therefore of the non-uniformity of the wave-field (e.g. Cox, 1973).

Second, due to the predominance of directional sources at frequencies lower than 0.3 Hz, below that frequency limit the correlation functions exhibit no or scarcely-reliable zero-crossings.

Third, measurements corresponding to low $\gamma(f)$ amplitudes (figure 6.12f and

6.12h mostly at higher frequencies) can be easily biased due to spectral leakage from adjacent frequencies.
Four, the assumption that SPAC techniques can only be used in the range $2 \leq \lambda/r \leq 15.7$ (e.g. Henstridge, 1979) is not respected, but for the selected pairs the measurements can be considered still valid; this derives from the time-averaged approach, replacing the azimuthal-uniformity of the wave-field sampling with the averaging over long time spans (e.g Tsai and Moschetti, 2010). Of course errors arise from this approximation, and they were measured from the standard deviation evaluated on the many different time windows on which the $\gamma(f)$ were computed for each station-pair. Application of the modified-SPAC to large ranges ($r \geq \lambda$) were performed by a number of authors (e.g Ekström et al., 2009; Calkins et al., 2011).
Only 38, of a 78 total possible pairs, PVDC passed the selection.

A second approach is instead based on the compound inversion of $\gamma(\omega, r)$, the correlation function associated with all the available inter-station distances. This yields a single (averaged) velocity dispersion for the array, instead of individual measurements for each receiver pair. This compound inversion is expected to provide more stable results than those obtained for individual station pairs, as the simultaneous utilization of different inter-station distances and azimuths is expected to alleviate the effects of the non-uniform spatial distribution of noise sources (Tsai and Moschetti, 2010).

The minimization of the difference between $\gamma(\omega, r)$ and $J_0(\omega r/c(\omega))$ was conducted using the iterative procedure of Chávez-García et al. (2005), as detailed in equation 3.12 of section 3.3.3.

Figure 6.14 shows the correlation functions as a function of frequency and station separation ($\gamma(\omega, r)$), whose general behavior suggests similarity with the zero-th order Bessel function $J_0(\omega r/c(\omega))$. The constants chosen for the covariance matrix of the parameters (equation 3.14) are $\sigma = 0.4$ (width of the smoothing window in frequency) and $\Delta = 500m/s$ (maximum accepted change of each parameter between two iterations). The covariance matrix of the data is expressed by the variances of $\gamma(\omega, r)$ evaluated over the many different time windows spanning the analyzed time interval. As an *a*

priori model, I tested different phase velocity dispersion curves derived from previous studies at LTGF:

1. PVDC of the fundamental mode Rayleigh waves obtained from 32 regional earthquakes recorded at GAPSS array (Saccorotti et al., 2014);

2. Average of the PVDCs predicted from the 3-D model obtained by the local earthquake tomography of Saccorotti et al. (2014);

3. PVDC predicted from the reference model derived by two-way travel time seismic profiles and deep wells (see table 6.1 and figure 6.13).

In addition, I also used an analytic dispersion curve given by the relationship ($c(f) = Af^{-B}$), which is rather similar to the curves described above.

Figure 6.15 shows the J_0 computed for the frequency and distance ranges as for the experimental data, and the *a priori* model 3.

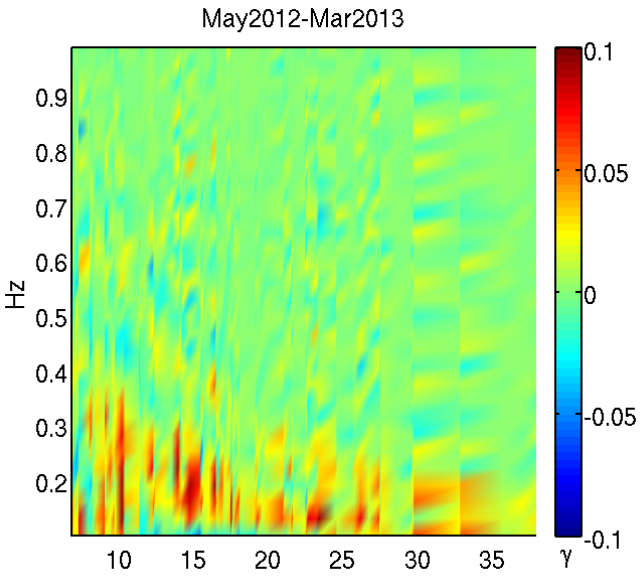

Figure 6.14: *Time-averaged complex coherence $\gamma(\omega, r)$, as a function of frequency and distance.*

The results of the iterative inversion, after 100 runs, are shown in figure 6.16 (lines connecting squares), together with their corresponding *a priori* curves (lines connecting circles). The short frequency span of the curves

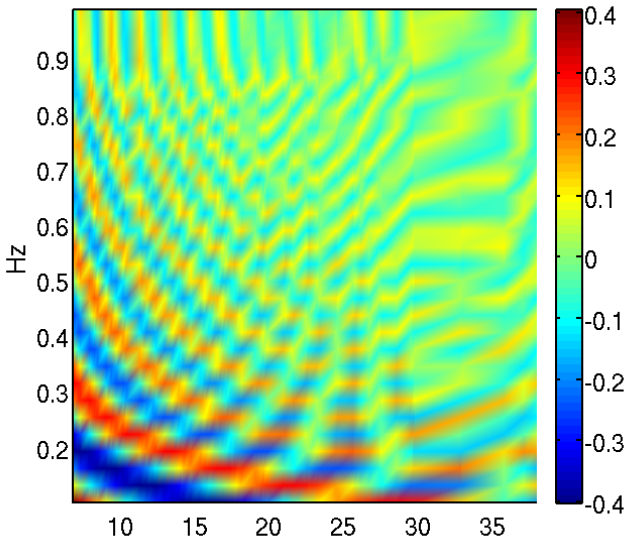

Figure 6.15: *Example of $J_0(\omega r/c(\omega))$, computed for a priori model PVDC 3 ($c(\omega)$), 0.1-1 Hz ($f = \omega/2\pi$) and GAPSS station-pairs distances (r).*

relative to the model 1 is due to the band-limited *a priori* information. A dependence on the *a priori* model can be observed for frequencies lower than 0.3 Hz. above this limit, all the different inversions substantially converge to mutually-consistent results, thus indicating a scarce dependence on the starting model. All the retrieved dispersion curves, however, report velocities which are about 500 m/s slower than those derived from the previous studies.

The errors on the inversion procedure are expressed by the *a posteriori* covariance matrix, whose value are in $(m/s)^2$. Figure 6.17 shows the *a posteriori* covariance matrix for the inversion associated with the *a priori* model 3. The squared root of the diagonal of the matrix is representative of the errors on phase velocity estimates. From figure 6.17 it is clear that the largest uncertainties are for frequencies $>$ 0.8 Hz, where loss of signal coherency affects significantly the reliability of the inversion procedure.

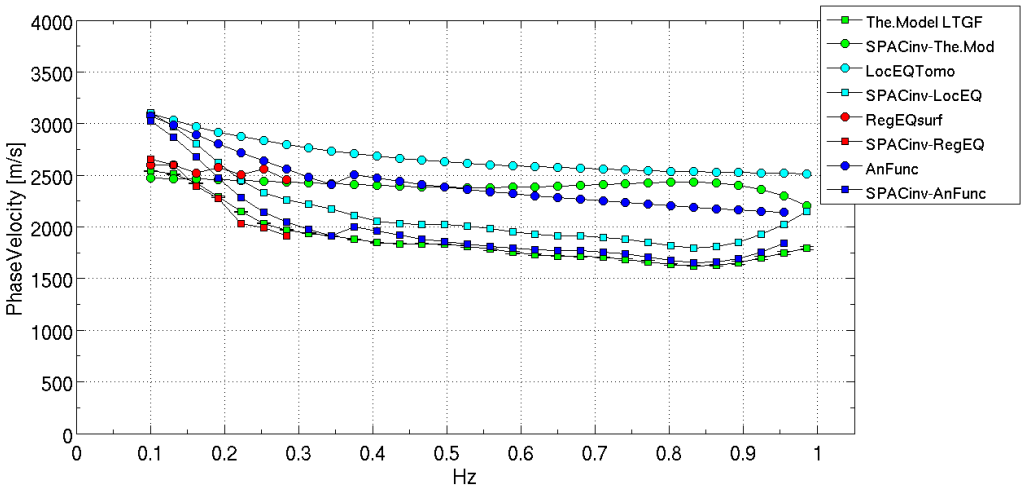

Figure 6.16: *Average PVDCs (curves connecting circles) for the area of LTGF as results of the inversion of the complex coherence matrix, for 4 different a priori models (curves connecting squares). Green curves are for 3 a priori model; light blue curves are for 2 model; red curves are for 1 model; dark blue curves are for the analytic-function model.*

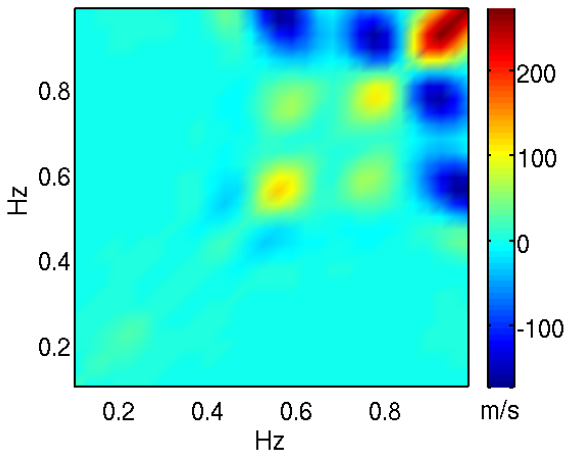

Figure 6.17: *A posteriori covariance matrix of inversion of SPAC as average PVDC, having 3 as a priori model.*

6.3 Discussion about Results of the Ambient Noise Stochastic Techniques

In this section the results derived by NCF and SPAC are compared and discussed in light of the dispersion curves predicted from the *a priori* information for the target area.

A first important result was provided by the iterative inversion of the complex coherence matrix, that yielded stable average PVDC for the entire LTGF (figure 6.16), showing underestimation of velocities of about 500 m/s with respect the reference velocity values.

Due to the variability of the measured dispersion curves and in order to investigate which method is more suitable in a complex geological context, I divided the GAPSS-station-pairs into three groups, in function of three different zones of LTGF crossed by each pair. The 3 groups are: 1) the central area of LTGF, 2) the southern margin of the central area and 3) the N-W sector confining with the central area.

These experimental PVDCs are compared to the range of phase velocities predicted from several velocity structures, namely:

- *AvMOD*, the average velocity model already shown in figure 6.13;
- *MN-1well*, derived from two-way travel times data from the MN-1 well 6.19;
- *BrucianoWell* obtained from a well-seismic-profile and sonic log of the multi- directional Bruciano exploration well (Batini et al., 1994); see figure 6.20,
- *LocEQTomo*, the local-earthquakes, travel-time tomography of Saccorotti et al. (2014)

In addition, I also considered *RegEQ*, a phase-velocity dispersion calculated from slowness analysis of Rayleigh waves from regional earthquakes

recorded by the GAPSS array.

The Central Sector

The comparison between the predicted phase- and group- velocity dispersion curves, and those respectively obtained from modified-SPAC and NCF analyses is shown in Figure 6.18.

This figure shows that reliable PVDCs are measured only for the frequency band 0.5-0.7 Hz; outside this range, the estimated PVDCs exhibit a steeper trend toward velocities which are lower than the reference ones by more than 500 m/s. An exception is the PVDC relative to LA09-LA12 pair, whose values are completely consistent with the reference ones.
The GVDCs, in figure 6.18b, are closer ($\ll$ 500 m/s) to reference curves, with the only exception of the pair LA07-TRIF, whose velocities are generally lower than those indicated by the predicted curves.

The Southern Sector

Figure 6.21 illustrates the dispersion curves for two station-pairs (LA08-LA10 and LA10-LA12) located along the same E-W profile at the southern border of the most productive area of LTGF. Both phase (Fig. 6.21a) and group (Fig. 6.21b) velocities are very consistent with the velocity ranges spanned by the predicted values.

The NW Sector

Figures 6.22 show the dispersion curves for GAPSS station-pairs spanning the North-West sector of the LTGF. Similarly to what observed for the southern margin, both PVDCs and GVDCs are closer to the reference curves than the results relative to the central part of the geothermal field. Reliable phase velocities are for frequencies $\geq$ 0.3 Hz, while group velocity information begins at $\geq$ 0.5 Hz. Even though individual PVDCs exhibit an oscillatory trend, they are consistent with each other, showing clear velocity inversions over the 0.45 Hz-0.55 Hz and 0.75 Hz - 0.85 Hz frequency intervals.

Overall, the match between the computed and predicted dispersions is

better for NCF results than for the modified-SPAC ones. Greater mismatch is found for SPAC results of the central LTGF, where the PVDCs seem to be more influenced by the strong lateral inhomogeneities and velocity inversions which are expected for this zone. This observation seems to be confirmed by the the better results found at profiles located outside of the most productive area. Actually, one should consider i) that the noise-based analysis should yield averaged mechanical properties of the subsoil between two receivers, and ii) that the frequency band of the estimated dispersion curves is relatively high, thus limiting the retrievable information to the first 1.5-2 Km of depth ($\sim 1/3$ of the longest wavelength), while the reference dispersion curves are influenced by lithologies down to depths ≥ 3 Km.

6.4 Sample Inversion of the Dispersion Curves

In this section I present some sample inversion of the dispersion curves discussed in the previous section.

6.4.1 Methods

The inversion of the surface wave dispersion curves for a velocity structure is conducted using the open-source software package *DINVER*©, which is part of the GEOPSY©project (Wathelet et al., 2004; Wathelet, 2005). *DINVER*©uses the conditional neighborhood algorithm (Sambridge, 1999a,b) to find the 1-D velocity structure, whose predicted dispersion best fits the observed ones in a least-square sense.

The neighborhood algorithm is a Monte Carlo technique relying on a pseudo-random generator, and it is self-adaptive in investigating the parameter space. This method samples the parameter space in order to find models with acceptable data fit. Within this procedure, a series of numbers with uniform probability is initialized by a random number seed. Different starting seeds generate different final models, but if the problem is sufficiently constrained, the algorithm converges to the same region of the model parameter space.

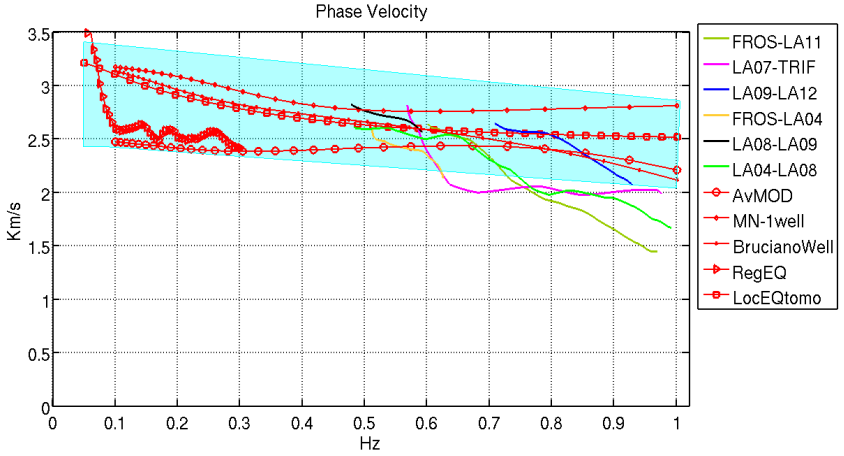

(a)

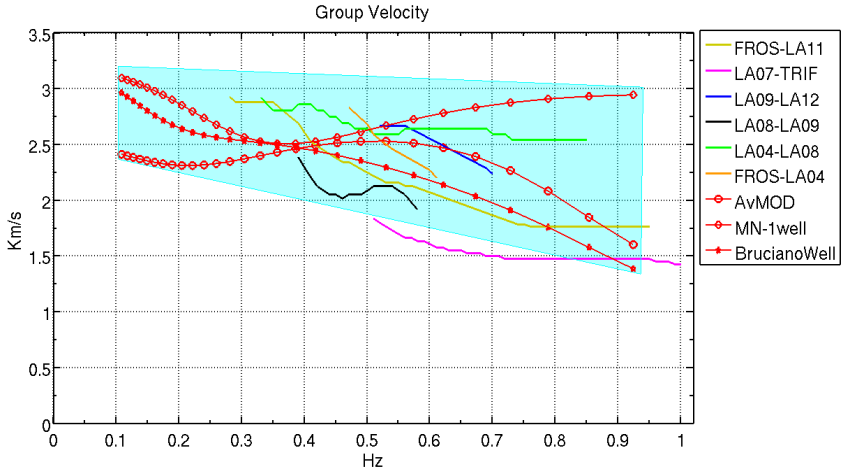

(b)

Figure 6.18: *Comparison between SPAC and NCF results for the central area of the LTGF. PVDCs (SPAC results in (a)) and GVDCs (NCF results in (b)) are shown for different profiles encompassing the area. Red curves with symbols are reference dispersion curves, described in the text. The light blue marked zone represents the range of values in which the results are more trustful.*

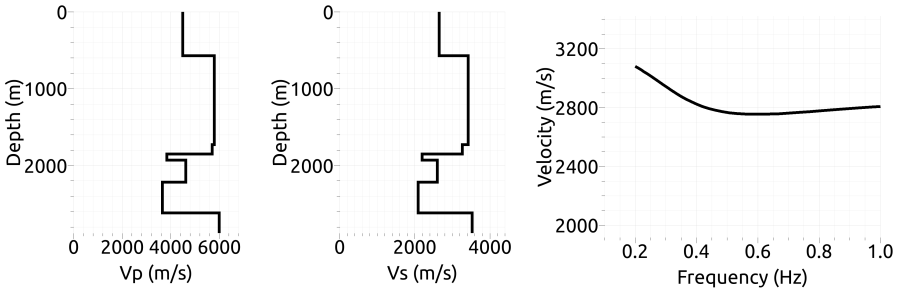

Figure 6.19: *1-D P and S velocity profiles based on two-way-travel time seismic profiles crossed with MN-1 exploration well data (Bertani et al., 2005), and forward computed dispersion curve of the fundamental mode of Rayleigh waves. For the location of MN-1 well see figure 4.4.*

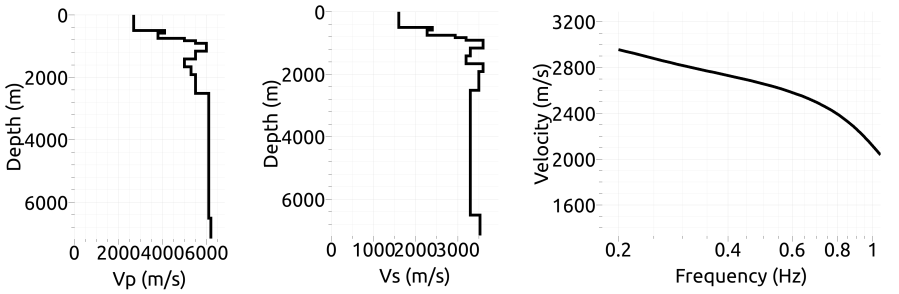

Figure 6.20: *1-D P and S velocity profiles based on the stratigraphy and seismic interpretation published by Batini et al. (1994); on the right the forward computed PVDC for the fundamental mode of Rayleigh waves. For the location of the Bruciano well see figure 4.4.*

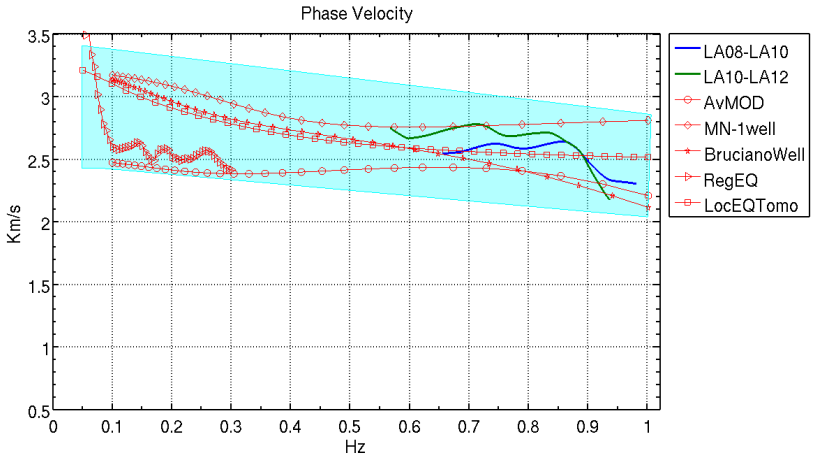

(a)

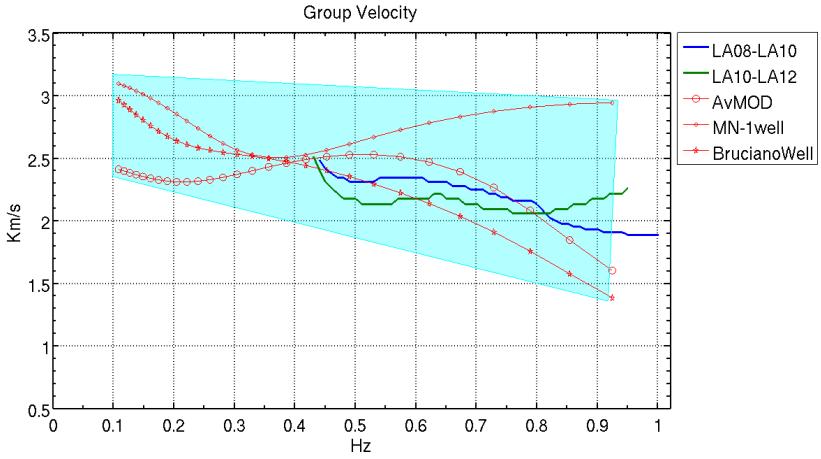

(b)

Figure 6.21: *Comparison of SPAC (a) and NCF (b) results for two station-pairs, on the same profile E-W, on the southern edge of the most productive area of LTGF. The reference dispersion curves are in red, and are the same of figure 6.18. The light blue area highlights most reliable velocity values.*

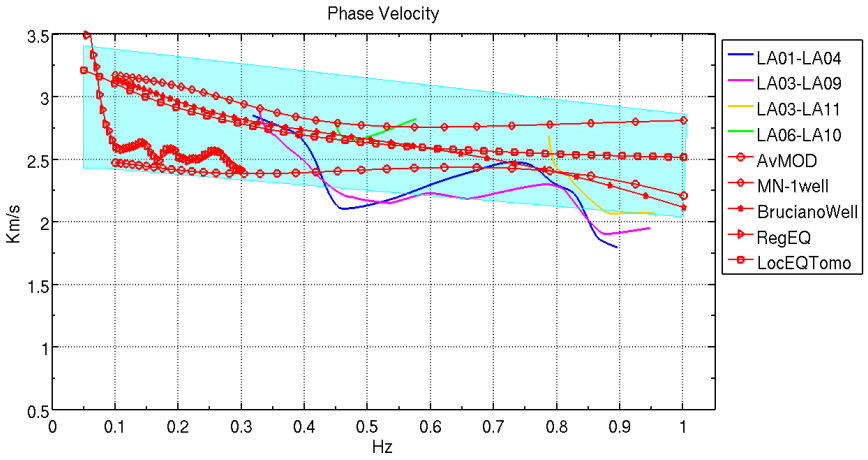

(a)

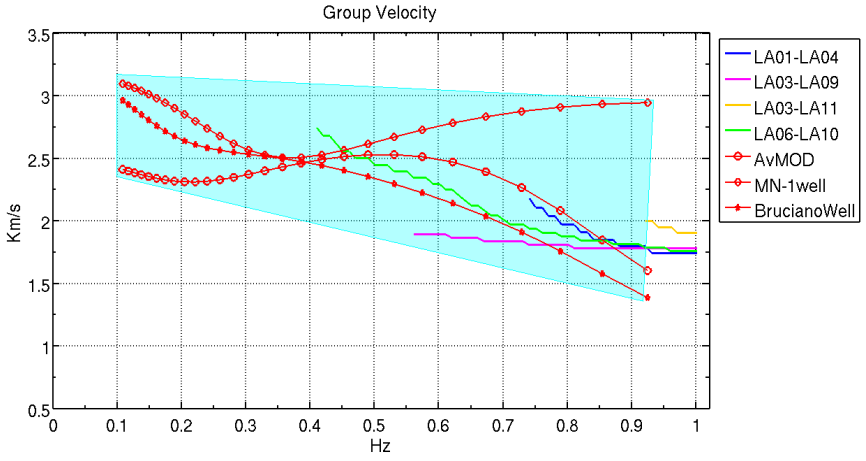

(b)

Figure 6.22: *Comparison of SPAC (a) and NCF (b) results for station-pairs of the North-Western margin of the productive area LTGF. The reference dispersion curves are in red, and are the same of figure 6.18. The light blue area highlights most reliable velocity values.*

The neighborhood algorithm is based on the partition of the parameter space into Voronoi cells. At the central point of each cell, an approximation of the misfit function is set as constant, and it affects the whole cell; with the subsequent iterations, the approximation of the misfit function is progressively refined.

The algorithm consists of 5 steps:

1. A set of n_{s0} models is randomly generated with a uniform probability in the model parameter space;

2. The misfit function is calculated;

3. The n_r, lowest-misfit models are selected;

4. n_s/n_r new samples are generated with a uniform probability in each selected cell;

5. The n_s new samples are added to the previous ensemble of models, then proceeding back to step (2).

The original cell becomes smaller as the sampling rate increases, but the center of the sampling is allowed to jump to another cell, if this latter has a lower misfit.

After a perturbation of the model parameters, a random walk is performed with a uniform probability density function inside the cell and zero outside. To confine the random walk inside a particular cell, the multi-dimensional limits of the cell are computed along lines which are parallel to the parameter axis. The process is exploratory when high (say: $\geq$ 100) n_r and n_s are selected; this usually provides lower final misfits, if the inversion is conducted with a great number of iterations (Wathelet, 2005).

Therefore, 4 tuning parameters are required, for which I selected the following values:

- Number of iteration: 1000,

- n_{s0} number of random models initialized within the parameter space at the beginning of the inversion: 50,

- n_s Number of models to be generates at each iteration: 50,
- n_r Number of best cells (with the lowest misfit) where the n_s models are generated: 100.

In order to check the robustness of the exploration of the parameters space, I conducted 5 distinct runs, each initialized with different seed values.

The choice of the model parametrization was made accounting for the constrains provided by geological-geophysical literature about LTGF, and leaving variability allowance. The parametrization is defined as follows:

```
---------------------- List of parameters and conditions

Parameterization checksum            = 1830560760
Dimension of parameter space         = 18

200 < TopVp0 < 2000 m/s(231 bins)
       BottomVp0 > TopVp0
       Poisson's ratio checked
1700 < BottomVp0 < 3600 m/s(75 bins)
       BottomVp0 > TopVp0
       Poisson's ratio checked
2200 < TopVp1 < 4000 m/s(60 bins)
       BottomVp1 > TopVp1
       Poisson's ratio checked
2400 < BottomVp1 < 4000 m/s(51 bins)
       BottomVp1 > TopVp1
       Poisson's ratio checked
3800 < TopVp2 < 5500 m/s(37 bins)
       BottomVp2 > TopVp2
       Poisson's ratio checked
5500 < BottomVp2 < 6100 m/s(10 bins)
       BottomVp2 > TopVp2
       Poisson's ratio checked
```

```
6100 < TopVp3 < 7500 m/s(20 bins)
       Poisson's ratio checked
100 < TopVs0 < 500 m/s(161 bins)
       BottomVs0 > TopVs0
       Poisson's ratio checked
500 < BottomVs0 < 2200 m/s(148 bins)
       BottomVs0 > TopVs0
       Poisson's ratio checked
1 < DVs0 < 800 m(671 bins)
1100 < TopVs1 < 2400 m/s(78 bins)
       BottomVs1 > TopVs1
       Poisson's ratio checked
1200 < BottomVs1 < 2400 m/s(69 bins)
       BottomVs1 > TopVs1
       Poisson's ratio checked
100 < HVs1 < 700 m(195 bins)
2500 < TopVs2 < 3500 m/s(33 bins)
       BottomVs2 > TopVs2
       Poisson's ratio checked
2900 < BottomVs2 < 4000 m/s(32 bins)
       BottomVs2 > TopVs2
       Poisson's ratio checked
800 < HVs2 < 4000 m(161 bins)
4000 < TopVs3 < 4600 m/s(14 bins)
       Poisson's ratio checked
2200 < TopRho0 < 2600 kg/m3(16 bins)
```

6.5 Examples of S-wave Velocity Profiles at the LTGF

The direct-search inversion, described in the previous subsection 6.4.1, was applied to the phase/group velocity obtained for three profiles crossing the

same areas discussed in 6.3. Even though the two different dispersions could be contemporaneously used for a joint inversion, I intentionally performed separate inversions for phase– and group-velocity dispersions, in order to highlight the different information provided by the two types of data.

Figure 6.23 shows the S-wave velocity profiles obtained for the station-pair FROS-LA11, crossing the productive area of Travale. The velocity profiles are obtained from inversion of phase (panel c) and group (panel d) velocity dispersions, calculated using modified-SPAC and NCF (panels 6.23a, 6.23b, respectively).

Since the dispersions defined by the two methods are defined over different frequency ranges, the corresponding models have distinct depth resolutions, which is on the order of $\sim$ 1500m and $\sim$ 2500m for the PVDC and GVDC results, respectively.

The two profiles are markedly different. A common feature is found at 150 m depth, where velocity increases sharply up to 1200 m/s, likely marking the passage from the Quaternary sediments to the underlying Ligurid Complex. The velocity contrast at $\sim$ 1300 m depth is also recognized by both profiles, but that found from the GVDC inversion is more likely, being constrained by velocity data extending down to lower frequencies. This sudden velocity increase could be associated with the H-Horizon, as inferred from the comparison with a geological cross-sections parallel to this profile (figure 6.24, after Bertini et al. (2006)).

Figure 6.25 illustrates the inversion results for the station-pair LA08-LA10, in the southern margin of the LTGF. Both profiles are characterized by a major velocity discontinuity at depths 600-700 m, below which Vs is as high as $\sim$ 3000 m/s. The maximum resolved depth is $\sim$ 1300 m for the PVDC inversion, and $\sim$ 1800 m for the GVDC inversion, hence no deeper features related to the metamorphic basement can be retrieved.
Above that major discontinuity, the velocities derived from PVDC and GVDC

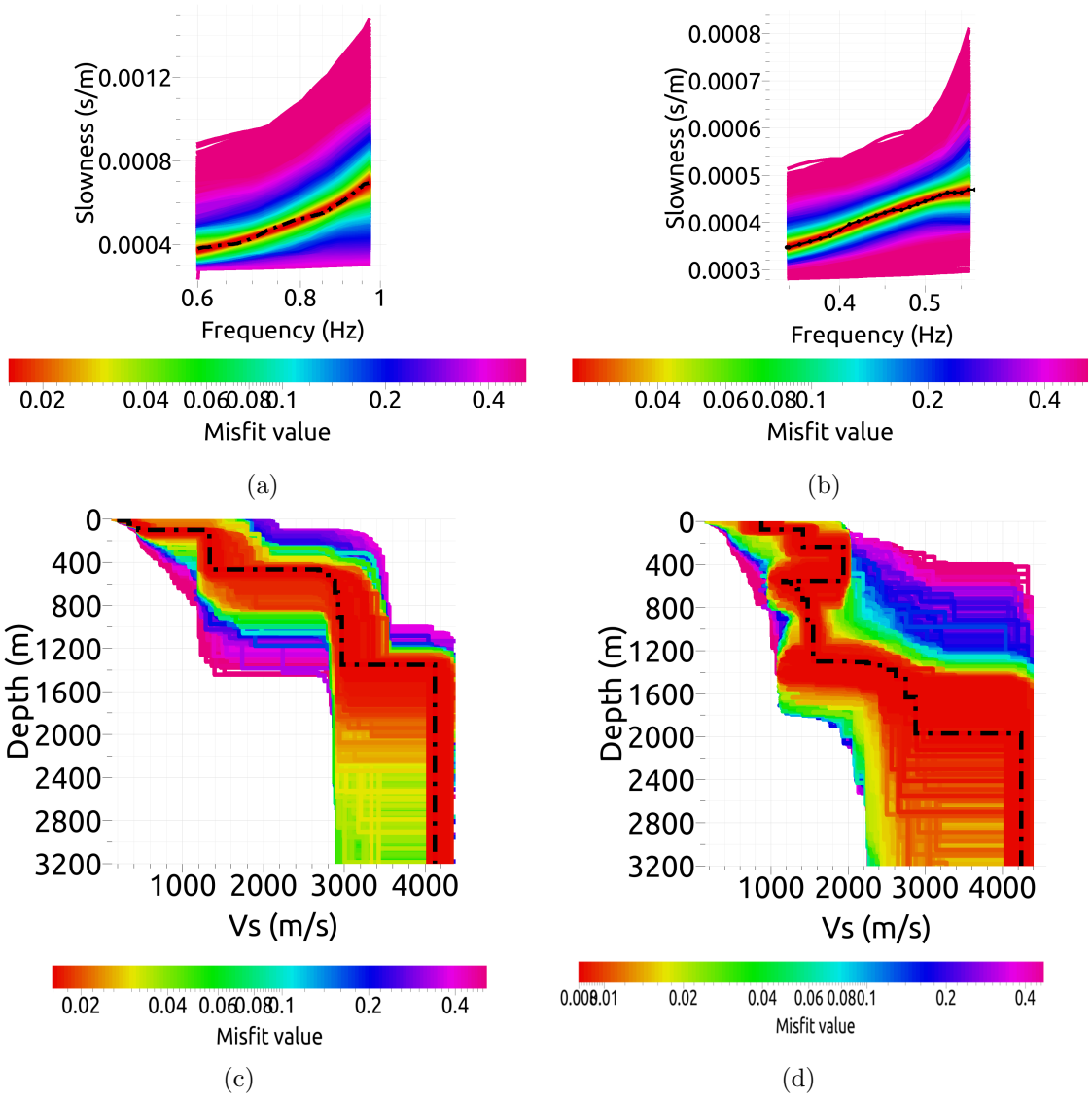

Figure 6.23: *1-D S-velocity profiles inverted from the phase (c) and group (d) velocity dispersion curves relative to the station-pair FROS-LA11, crossing the most productive area of LTGF; the best models, associated with the lower misfit values, are indicated as black dashed lines. The misfits associated with the different predicted dispersion curves are shown in panels (a) (PVDC) and (b) (GVDC), where the experimental data are marked by the black dotted curves. Note that slowness, depth, frequency axes and misfit color-maps are differently scaled, in order to emphasize the features of individual inversions.*

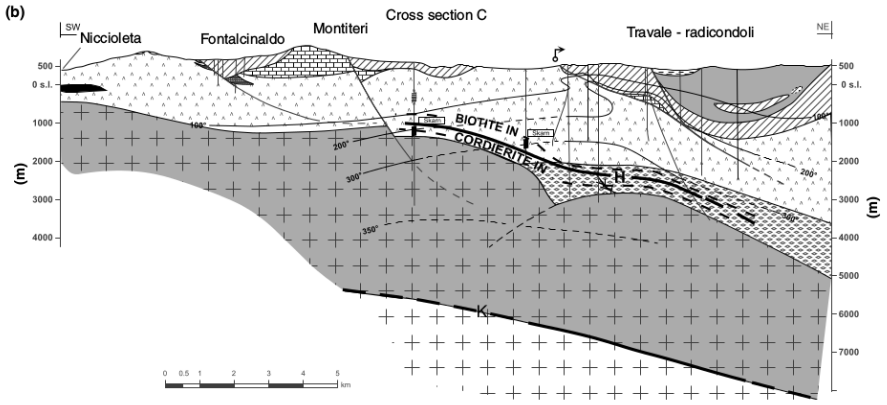

Figure 6.24: *Geological cross-section of the central area of LTGF, published in figure 4-c in Bertini et al. (2006). The H-horizon can be followed, interpreted as the contact between the upper Triassic evaporites– Paleozoic formations and the lower Pliocene granites.*

are markedly different, and it is difficult to state which of the two is more reliable.

Finally, the inversion of PVDC and GVDC estimated for the pair LA01-LA04 (North-West of LTGF) is shown in figure 6.26. Once more, the marked velocity which is encountered at depths of 600 m and 400 m for the PVDC and GVDC inversions, respectively, could be interpreted as top of the Tuscan Nappe formation/Late Triassic evaporites, as for the previous example (figure 6.25).

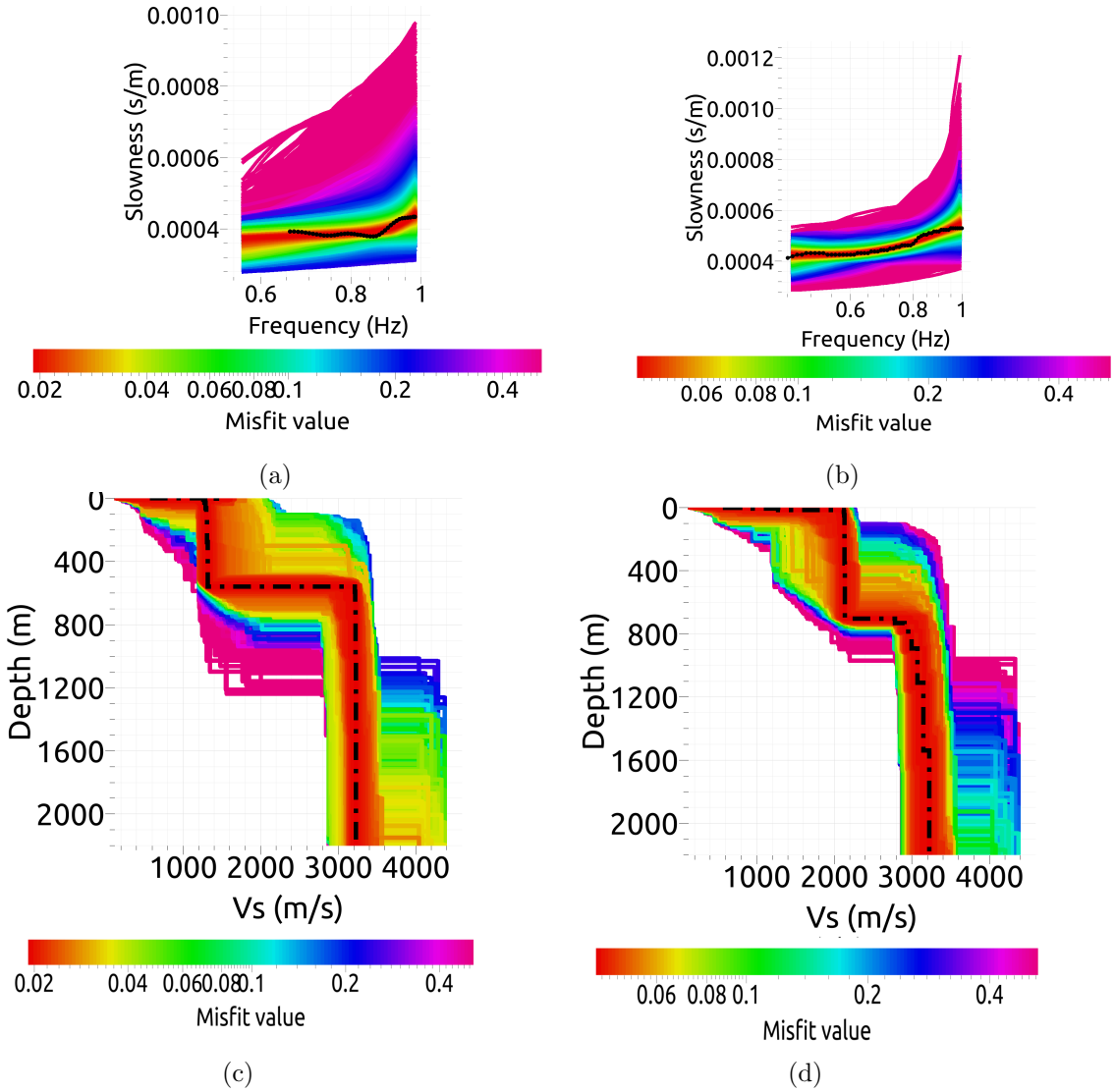

Figure 6.25: *1-D S-velocity profiles inverted from the phase (c) and group (d) velocity dispersion curves relative to the station-pair LA08-LA10, involving the southern margin of the most productive area of LTGF; The best models, associated to the lower misfit value, are indicated as black dashed profile. The forward computed dispersion curves associated to the velocity profiles are in (a) (PVDC) and (b) (GVDC); the black dashed curves are the experimental one. Please note that slowness and frequency axes and misfit color-maps are differently scaled, in order to emphasize singular features.*

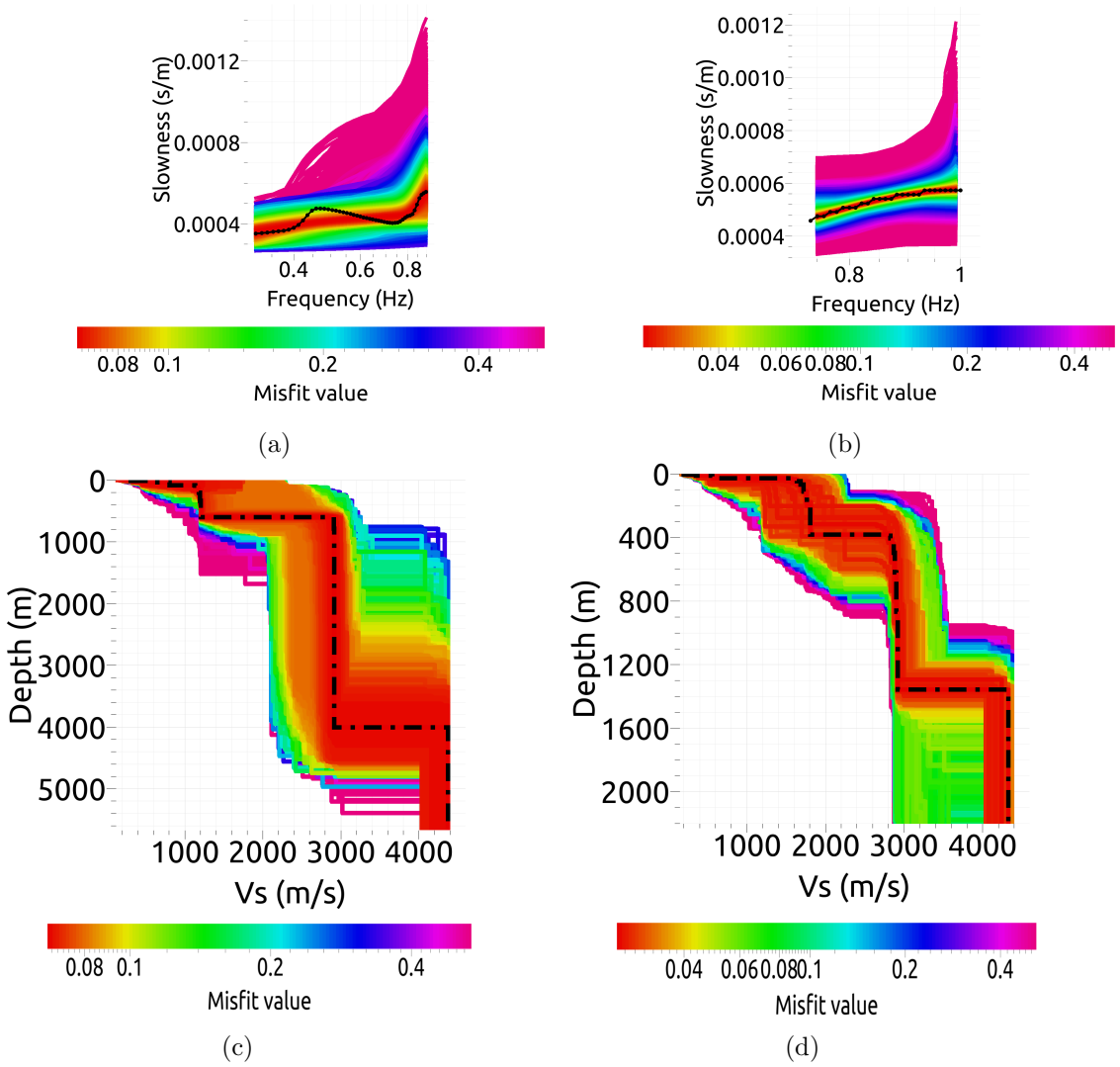

Figure 6.26: *1-D S-velocity profiles inverted from the phase (c) and group (d) velocity dispersion curve relative to the station-pair LA01-LA04, crossing the North-Western part of LTGF; The best models, associated to the lower misfit value, are indicated as black dashed profile. The depth axes are differently scaled. The forward computed dispersion curves associated to the velocity profiles are in (a) (PVDC) and (b) (GVDC); the black dashed curves are the experimental one. Please note that slowness and frequency axes and misfit color-maps are differently scaled, in order to emphasize singular features.*

Discussion and Conclusions

Over the past ten years, seismic ambient noise has been widely exploited for inferring the elastic properties of the Earth's interior, on the basis of the well-established correspondence between the Noise Correlation Function evaluated at a pair of sites, and the Green's function of the medium in between them. Such equivalence relies however on several assumptions, the most critical of which concerns the energy equipartitioning of the noise wavefield. Any attempt of subsurface imaging using passive noise sources should therefore be preceded by an accurate and quantitative assessment about the structure of the noise wavefield.

Within this context, this thesis has been aimed at a thorough investigation about feasibility and robustness of the noise-based methods toward the imaging of complex geological structures at the local ($\sim 10 - 50$ Km) scale. The study focused on the analysis of a large seismological data set collected at the Larderello-Travale geothermal field (Tuscany, Italy), an area for which the underground structure is well-known thanks to decades of geothermal exploration.

My analyses focused on the 0.1-1 Hz portion of the noise spectra which is usually referred to as *Secondary Microseism* (SM), whose characteristics and origin are described in chapter 1. The following two chapters describe the methods used for the deterministic (chapter 2) and stochastic (chapter 3) analyses of the noise wavefield.

A geological and seismological outline of the LTGF and the description of the experimental data set used for this work are provided in chapter 4.

Chapter 5 reports the results from application of the deterministic (beam-

forming) analysis. This part of the work was aimed at verifying the assumptions for the subsequent application of the noise stochastic techniques. The main finding was that secondary microseism wavefield at LTGF is not fully diffuse, but the most prominent directions-of-arrival depend on both frequency and season. In particular, I found that the wavefield at frequencies < 0.3 Hz is dominated by high-apparent-velocity waves, which are particularly evident in the Spring-Summer recordings. Considering their dominant back-azimuth centered at 150°N, these arrivals are interpreted in terms of body waves generated by Winter storms in the southern hemisphere. At frequencies > 0.3 Hz the SM is observed to propagate from a broader range of directions, with a prevalence of sources spanning the 240-330°N and 120-210°N directional intervals. The possible locations of secondary microseism sources exhibit significant concordance with those derived in previous studies on SM in Europe; moreover, the central position of the GAPSS array with respect to the Mediterranean sea allowed also the recognition of likely sources located throughout the eastern quadrants (i.e., Adriatic and Ionian Seas). These results provided a main constraint about the conditions of applicability of the noise stochastic techniques. In fact, the retrieval of surface (Rayleigh) waves Green's functions has to be be carried out at frequencies higher than 0.3 Hz, in order to avoid the interference of the low-frequency body waves arrivals and to account for broader incoming directions.

The above consideration was confirmed by the results from the noise correlation analyses (chapter 6). The action of stable directional sources was evidenced by the time-domain asymmetry and non-zero imaginary parts of the time- and frequency-domain noise cross-correlations, respectively. Such features persist even when stacking the cross-correlations over extended (11 months) time intervals, confirming the temporal stability of the most localized sources. The effects of directionality are alleviated, however, once high-pass filtering the correlation functions at frequencies above 0.3Hz, where the wavefield exhibits improved homogeneity.

These initial analyses also allowed determining the time interval after which the stacked correlation estimates become stable. I found in fact that

the NCFs do not exhibit any significant change for stacking periods longer than ~ 6 months.

A rigorous selection of results from NCF reduced severely the number of the corresponding Green's functions to be used for evaluating the dispersion properties of Rayleigh waves. The selected empirical Green's functions were then subjected to Frequency-Time ANalysis (FTAN), in order to estimate Rayleigh-wave group-velocity dispersion. Such procedure, however, was sometimes affected by ambiguities in the modal attribution of the measured velocities, as a consequence of the mixing between the fundamental- and higher- Rayleigh-wave modes. These misleading measurements were thus discarded, further reducing the number of accepted velocity samples. After this selection, all the retrieved group velocities resulted to be compatible with those predicted from the different models based on exploration-wells and seismic/geological profiles of the area.

I then tested the modified-SPAC method, and estimated the phase-velocity dispersion curve from the inversion of the complex-coherence, $\gamma(f)$. The phase-velocity dispersion curve resulting from the iterative inversion of the matrix $\gamma(f, r)$ relative to the entire array exhibited a weak dependence on the starting model; overall, the results were stable and consistent within each other, but providing velocity values about 500 m/s slower than the range spanned by independent studies on LTGF.

Results from the inversion of the two-station profiles $\gamma(f)$ led to more unstable phase-velocity dispersion curves, especially for station pairs located in the most productive area of LTGF, which is characterised by a more complex and heterogeneous subsoil context.

In the last part of the thesis, I retrieved shear-velocity profiles by inverting separately the group- and phase-velocity dispersions obtained from NCF and SPAC analyses, respectively. These velocity structures were then compared with the available data about the internal structure of the LTGF. Results from the two methods differ significantly, though a concordance is found in the identification of the main velocity discontinuities. In general, velocities resulting from SPAC are lower than those retrieved by NCF, the latter ones being more consistent with the velocity ranges spanned by both

direct and indirect probing of the area.

Overall, the results presented in this work show the limitations of imaging techniques based on secondary microseism wavefields, once applied to complex geological structures characterised by marked heterogeneities at different scale lengths.

In particular, the most critical aspects concern:

- The need of long acquisition periods, in order to obtain stable and reliable correlation-based GF estimates;
- the poor depth penetration, as a consequence of the band limitations imposed by the dominance of body-wave arrivals within the lowest frequency portion (0.1-0.3 Hz) of the SM spectra;
- the possible ambiguities in mode identification, which can bias significantly the subsequent inversion of the dispersion curves.

On the basis of these points, future analysis should include:

- A more thorough assessment of wavefield directionality by using, for instance, F-K filters to isolate waves propagating along the same direction of the station-pair selected for the analyses;
- The utilisation of more sophisticated inversion procedures, by using misfit functions which do not depend upon modal identification (e.g Maraschini et al., 2010).

A further development is represented by the tomographic imaging, choosing the most represented and well–constrained frequencies, for better resolving at least the shallower geological features. Tomographic images at discrete depths could provide details which got lost in 1D shear-velocity profiles, as the latter ones only represent the average properties of the Earth's interior in between the two recording sites.

Finally, it must be noted that the possible SM-generating areas were only inferred on the basis of the retrieved propagation directions. A further development would thus consist in the identification of the microseism sources through (a) triangulation of beamforming results from the different arrays which are operative in Europe, and (b) inversion of seismic amplitudes given an attenuation law. While providing a reference for any stochastic-noise application, these studies would improve the knowledge about the mechanisms of SM generation in the Mediterranean area, thus contributing to the understanding of the relationships between microseisms and sea climate.

Acknowledgements

At the end of this work I would like to express my most sincere acknowledgements to

- the INGV team who organized and conducted the GAPSS experiment;
- Ph.D. Antonio Emolo, who provided thoughtful suggestions throughout the development of this study;
- Prof. Chris Bean and the Geophysics group of the UCD (University College of Dublin) for their hospitality during my secondment;
- Ph.D. Andrea Orlandi from LAMMA for having provided results from WWIII simulations.

Appendix A
Publications on the GAPSS project

In this appendix, I include the abstracts of the scientific publications and the contributes to international conferences about the researches at Larderello-Travale geothermal field, undertaken for the GAPSS (Geothermal Area Passive Seismic Sources) project at which I collaborated during my Ph.D..

Remotely triggered micro-earthquakes in the Larderello-Travale Geothermal Field (Italy) following the 2012 May 20, Mw 5.9 Po-plain earthquake

Citation: Saccorotti, G., Piccinini, D., Mazzarini, F., and Zupo, M. (2013). Remotely triggered micro-earthquakes in the Larderello-Travale geothermal field (Italy) following the 2012 may 20, mw 5.9 po-plain earthquake. *Geophysical Research Letters*, 40(5):835–840.

Abstract

We report observations of remotely triggered earthquakes at the Larderello-Travale Geothermal Field (Italy), following the Mw = 5.9 Po-Plain earthquake on 20 May 2012. Four distinct triggered events are recognized within a short ($\sim$ 25 s) time interval accompanying the sweeping of $\sim$ 10s Rayleigh waves. Triggered sources are clustered at depths in between 4 Km and 6 Km. The magnitude and distance of the mainshock agree well with the triggering threshold previously proposed for The Geysers, California. For three out of four earthquakes, the Rayleigh wave dynamic stresses are mostly associated with extensional vertical (s_{zz}) and shear (s_{xz}) components, which range up to 5 KPa. Once considering the structural setting of the area, the most likely triggering mechanism involves the rupture of normal faults which are kept close to failure by high-pressure crustal fluids.

Passive, Broad-Band seismic measurements for geothermal exploration: the GAPSS experiment

Piccinini, D., Saccorotti, G., Mazzarini, F., Zupo, M., Capello, M., Musumeci, G., Cauchie, L., and Chiarabba, C. (2013). Passive, broad-band seismic measurements for geothermal exploration: the GAPSS experiment. In *Proceedings of the European Geothermal Congress.*

Abstract

Passive seismological imaging techniques based on either transient (earthquakes) or sustained (background noise) signals can provide detailed descriptions of subsurface attributes as seismic velocity, attenuation, and anisotropy. However, the correspondence between these parameters and the physical properties of crustal fluids is still ambiguous. Moreover, the resolving capabilities and condition of applicability of emerging techniques such as the

Ambient Noise Tomography are still to be investigated thoroughly. Following these arguments, a specific project (GAPSS-Geothermal Area Passive Seismic Sources) was planned, in order to test passive exploration methods on a well-known geothermal area, namely the Larderello-Travale Geothermal Field (LTGF). This geothermal area is located in the western part of Tuscany (Italy), and it is the most ancient geothermal power field of the world. Heat flow in this area can reach local peaks of 1000 mW/m^3. The deep explorations in this area showed a deeper reservoir (3000 to 4000 m depth) located within the metamorphic rocks in the contact aureole of the Pliocene-Quaternary granites [Bertini et al., 2006]; it is characterized by a wide negative gravimetric anomaly, interpreted as partially molten granite at temperatures of 800℃[Bottinga and Weill, 1970]. From seismic surveys the marker K (pressurized horizons) was found at depths between 3 and 7 Km [Batini and Nicolich, 1984; Bertini et al., 2006]. The structural grain of the geothermal field is characterized by N-W trending and N-E dipping normal faults whose activity lasts since the Pliocene [Brogi et al., 2003]. GAPSS is ongoing since early May, 2012, and it consists of 12 temporary seismic stations, complemented by two permanent stations from the National Seismic Network of Italy. The resulting array has an aperture of about 50 Km, with average station spacing of 10 Km. Stations are equipped with either broadband (40s and 120s) or intermediate-period (5s), 3-components seismometers. LTGF is seismically active. During the first 2 months of measurements, we located about 250 earthquakes, with a peak rate of up to 40 shocks/day. Preliminary results from analysis of these signals include: (i) a study of local micro-earthquakes remotely triggered by the surface waves from the Po Plain main-shock (May 20,2012). Results suggest a triggering process most likely related to the Coulomb failure of faults kept close to rupture by elevated fluid pore pressure. (ii) The detailed location of clustered microearthquakes from inversion of differential times, thus obtaining a detailed picture of fracture geometry. (iii) Seismic noise analysis, thus far mostly aimed at elucidating the directional properties of the noise wavefield over the microseismic (0.1-0.5 Hz) frequency band.

The Deep Structure of the Larderello-travale Geothermal Field (Italy) from Integrated, Passive Seismic Investigations

Citation: Saccorotti, G., Piccinini, D., Zupo, M., Mazzarini, F., Chiarabba, C., Agostinetti, N. P., Licciardi, A., and Bagagli, M. (2014). The deep structure of the Larderello-Travale geothermal field (Italy) integrated, passive seismic investigations. *Energy Procedia*, 59:227–234.

Abstract

We report the preliminary results from a project (GAPSS-Geothermal Area Passive Seismic Sources), aimed at testing the resolving capabilities of passive exploration methods on a well-known geothermal area, namely the Larderello-Travale Geothermal Field (LTGF). Located in the western part of Tuscany (Italy), LTGF is the most ancient geothermal power field of the world. GAPSS consisted of up to 20 seismic stations deployed over an area of about 50 x 50 Km. During the first 12 months of measurements, we located more than 2000 earthquakes, with a peak rate of up to 40 shocks/day. Preliminary results from analysis of these signals include: (i) analysis of Shear-Wave-Splitting from local earthquake data, from which we determined the areal distribution of the most anisotropic regions; (ii) local-earthquake travel-time tomography for both P- and S-wave velocities; (iii) telesismic receiver function aimed at determining the high-resolution (< 0.5 Km) S-velocity structure over the 0-20 Km depth range, and seismic anisotropy using the decomposition of the angular harmonics of the RF data-set; (iv) S-wave velocity profiling through inversion of the dispersive characteristics of Rayleigh waves from earthquakes recorded at regional distances. After presenting results from these different analyses, we eventually discuss their potential application to the characterization and exploration of the investigated area.

The Broad-Band Seismic Noise Wavefield at the Larderello-Travale Geothermal Field (Italy)

Citation: Zupo, M., Saccorotti, G., Piccinini, D.. The Broad-Band Seismic Noise Wavefield at the Larderello-Travale Geothermal Field (Italy). American Geophysical Union (AGU) Fall Meeting, 9–13 December 2013, San Francisco (CA,USA). Abstract num. S43B-2510

Abstract

Cross-correlation of ambient noise wave-field between a pair of receivers (NCF), provides an estimate of the Green's Function between the two sites, thus allowing extraction of the associated group velocity dispersion curve. This is valid under the assumption that noise sources and/or scatterers are isotropically distributed and uncorrelated each other. These conditions are usually met once the cross-correlations are averaged over long time intervals. At frequencies lower than 1 Hz, ambient noise wavefield is essentially composed by surface waves that are mostly associated with oceanic sources; as a consequence, the noise wavefield may exhibit marked directional properties over short (day) to intermediate (weeks) time scales. A detailed assessment of the nature and duration of these sources is therefore required in order to define the optimal conditions for retrieving the Green's functions from NCF analysis. This study presents ambient noise analysis for the Larderello-Travale Geothermal Field (Italy). We use data collected by a temporary seismic array consisting of 20 broad-band instruments, with station spacing ranging from 6 to 50 Km. Below 1 Hz, the most energetic sources are those associated with both primary and secondary microseisms, with dominant spectral peaks spanning the 0.05-0.5 Hz frequency range. Focusing on the secondary microseism sources (f $>$ 0.1 Hz), we test the validity of the isotropic-wavefield assumption by determining the kinematic properties of the wavefield using frequency-domain beamforming. For the May-November 2012 time span, our results show that the most energetic and persistent wavefield components propagate from WNW (Gulf of Marseille and Genova) and

SW (Sardinia channel). In the late part of the observation period, additional wavefield components are observed to propagate from the NE-SE azimuthal range, corresponding to sources located throughout the Adriatic sea. This suggests that the conditions for the application of the NCF technique can be met by averaging cross-correlation estimates over a period of a few months. The NCF analysis included a pre-processing step, consisting of signal filtering and normalization. Then, we calculated cross- correlations between all independent station pairs, and stacked these functions over the entire observation period. Finally, the retrieved Green's functions are subjected to a frequency-time analysis, in order to obtain group velocity dispersion curves for each station pair. The local velocity structure and the inter-station distances are key factors conditioning the frequency range within which the surface wave dispersion can be correctly measured. When the ratio between the inter-station distance and the wavelength of interest is lower than ~ 3, NCF can severely fail. For these cases, we used the Spatial Autocorrelation Function (SPAC), which relates the frequency-dependent spatial autocorrelation functions to the phase velocity dispersion curve. In the analyzed frequency band we also found evidences for signals traveling with high apparent velocities ($>$ 8000 m/s). Beamforming and polarization analysis indicate that these signals are likely associated with P- waves generated in deep water far from coastlines.

Secondary Microseisms Characterization and Green's Functions Extraction at the Larderello-Travale Geothermal Field (Italy)

Citation: Zupo, M, Saccorotti, G. . Secondary Microseisms Characterization and Green's Functions Extraction at the Larderello-Travale Geothermal Field (Italy). 57th Irish Geological Research Meeting (IGRM), 28 February – 2 March 2014, Dublin (IRE)

Abstract

Cross-correlating a diffusive and uncorrelated wavefield (NCF) over sufficiently long time period can provide an estimate of the Green's function (GF) between two sites, from which is possible to extract the velocity dispersion curve. The noise wavefield at frequencies lower than 1 Hz is mostly composed by surface waves caused by oceanic sea state. This noise mirrors the sea-state variability. This study presents the quantitative analysis of noise recorded at the Larderello-Travale Geothermal Field (Italy) between May-November 2012. We use data collected by a 50 Km diameter temporary seismic array. To validate the assumptions underlying the NCF analysis we first characterize the noise sources. We study the secondary microseisms (f $>$ 0.1 Hz), to determine sources kinematic properties using a beamforming technique. We show that most of the microseisms energy propagates with apparent velocities between 2-3 Km/s. The noise sources show spatially spread back-azimuths with two areas in the Mediterranean with more likely source locations. We see also high apparent velocity ($>$ 8 Km/s) signals: further studies are however needed to better understand these signals. The directional and spectral properties of the noise are then compared to models from WaveWatchIII computed for the Mediterranean. Seismological observations agree with wave models and the comparison show the key role of rocky and steep coasts. The almost isotropic distribution of noise sources indicates that averaging cross-correlation estimates over a few months period can meet the assumptions for the application of the NCF technique. We perform the NCF analysis and the inter-station GF are retrieved. Then we apply the frequency-time analysis (FTAN), in order to obtain group velocity dispersion curves for each station pair. Overall this analysis allows us to undertake depth imaging based on recordings of seismic noise (i.e. in the absence of seismic shots).

Ambient Noise characterization at the Larderello-Travale Geothermal Field (Italy)

Citation: Zupo, M., Saccorotti, G., Piccinini, D., Cauchie, L., Orlandi, A.. Ambient Noise characterization at the Larderello-Travale Geothermal Field (Italy). European Geophysical Union (EGU) General Assembly, 27 April – 2 May 2014, Vienna (AT). Abstract num. 11444

Abstract

Given a pair of receivers, the cross-correlation function of ambient noise wave-field (NCF) provides an estimate of the Green's Function between the two sites, which allows extraction of the associated group velocity dispersion curve. Such a procedure is valid under the assumption that noise sources and/or scatterers are isotropically dis- tributed and uncorrelated each other; these conditions can be achieved once the NCFs are averaged over long time intervals. At frequencies lower than 1 Hz, ambient noise wavefield is essentially composed by surface waves that are mostly associated with oceanic sources; as a consequence, the noise wavefield may exhibit marked directional properties over short (day) to intermediate (weeks) time scales. A detailed assessment of the nature and duration of these sources is therefore required in order to define the optimal conditions for retrieving the Green's functions from NCF analysis. Following these premises, this study focuses on the quantitative analysis of the ambient seismic noise as observed at the Larderello-Travale Geothermal Field (Italy). We use data collected by a temporary seismic array consisting of 20 broad-band instruments, with inter-station distances ranging from 2 to 50 Km. Below 1 Hz, the most energetic sources are those associated with both primary and secondary microseisms, whose dominant spectral peaks span the 0.05-0.5 Hz frequency range. Focusing on the secondary microseism band (f $>$ 0.1 Hz), we determine the kinematic properties of the noise wavefield using frequency-domain beamforming. For the May- November 2012 time span, our results show that the most energetic and persistent wavefield components propagate from

WNW (Gulf of Marseille and Genoa) and SW (Sardinia channel). In the late part of the observation period, additional wavefield components are observed to propagate from the NE-SE quadrant, corresponding to sources located throughout the Adriatic sea. Most of the noise energy propagates with apparent velocities spanning the 2-3 Km/s range, thus suggesting a dominance of surface (Rayleigh) waves. The directional and spectral properties of the noise derived from Beamforming analysis are then compared to outputs from WaveWatch III simulations, which predict the significant wave height and dominant periods throghout the Mediterranean Sea. The good agree- ment between seismological observations and wave models suggest the possibility of adopting seismological noise observations for ocean climate studies. The temporal variability of the spatial distribution of marine noise sources indicates that the conditions for the application of the NCF technique can be met by averaging cross-correlation estimates over a period of a few months. Noise recordings are then subjected to NCF analysis, allowing for the re- trieval of inter-station Green's functions. These latter ones are then subjected to a frequency-time analysis (FTAN), in order to obtain group velocity dispersion curves for each station pair. For the cases in which the ratio between the inter-station distance and the wavelength of interest was lower than ~ 3, we adopted the Spatial Autocorrelation Function (SPAC), which relates the frequency-dependent spatial autocorrelation functions to the phase velocity dispersion curve. In the analyzed frequency band we also found evidences for signals traveling with high appar- ent velocities (> 8 Km/s). Beamforming and polarization analysis indicate that these waves are likely associated with P-waves generated in deep water far from coastlines. Further studies are however needed to better understand location and processes originating these signals.

Passive, broad-band seismic measurements for geothermal exploration : The GAPSS experiment

Citation: Saccorotti, G., Piccinini, D., Zupo, M., Mazzarini, F., Cauchie, L., Chiarabba, C., Piana Agostinetti, N.. Passive, broad-band seismic measurements for geothermal exploration: The GAPSS experiment. European Geophysical Union (EGU) General Assembly, 27 April – 2 May 2014, Vienna (AT). Vol.16, p. 11578

Abstract

Passive seismological imaging techniques based on either transient (earthquakes) or sustained (background noise) signals can provide detailed descriptions of subsurface attributes as seismic velocity, attenuation, and anisotropy. However, the correspondence between these parameters and the physical properties of crustal fluids is still ambiguous. Moreover, the resolving capabilities and condition of applicability of emerging techniques such as the Ambient Noise Tomography are still to be investigated thoroughly. Following these arguments, a specific project (GAPSS-Geothermal Area Passive Seismic Sources) was planned, in order to test passive exploration methods on a well-known geothermal area, namely the Larderello-Travale Geothermal Field (LTGF). This geothermal area is located in the western part of Tuscany (Italy), and it is the most ancient geothermal power field of the world. Heat flow in this area can reach local peaks of 1000 mW/m3. The deep explorations in this area showed a deeper reservoir (3000 to 4000 m depth) located within the metamorphic rocks in the contact aureole of the Pliocene-Quaternary granites; it is characterized by a wide negative gravimetric anomaly, interpreted as partially molten granite at temperatures of 800℃. From seismic surveys the K-marker K (pressurized horizons) was found at depths between 3 and 7 Km. The structural grain of the geothermal field is characterized by N-W trending and N-E dipping normal faults whose ac-

tivity lasts since the Pliocene. GAPSS lasted from early May, 2012, through October, 2013. It consisted of up to 20 temporary seismic stations, complemented by two permanent stations from the National Seismic Network of Italy. The resulting array has an aperture of about 50 Km, with station spacings between 2 and 50 Km. Stations are equipped with either broadband (40s and 120s) or intermediate-period (5s), 3-components seismometers. LTGF is seismically active. During the first 10 months of measurements, we located more than 1000 earthquakes, with a peak rate of up to 40 shocks/day. Preliminary results from analysis of these signals include: (i) The analysis of clustered microearthquakes likely resulting from re-injection processes, thus allowing for the detailed determination of the temporal and magnitude distributions which are likely indicators of induced seismicity; (ii) Seismic noise analysis for deriving the 0.05-0.5 Hz dispersive properties of the noise wavefield, which are inverted for shear-wave velocity profiles; (iii) The analysis of Shear-Wave-Splitting from local earthquake data, from which we found an anisotropic layer which correlates well with the K-horizon; (iv) Local-earthquake Travel-Time tomography for both P- and S-wave velocities, and (v) telesismic receiver function aimed at determining the high-resolution (<0.5 Km) S-velocity structure over the 0-10Km depth range, and seismic anisotropy using the decomposition of the angular harmonics of the RF dataset. This latter technique decouples the P-to-S converted energy generated at isotropic discontinuity from energy generated within an anisotropic body. In this manner, we are able to precisely locate the source of the seismic anisotropy at depth. In this communication we present pre- liminary results from these analysis, I turn discussing their applicability to the exploration of geothermal resources.

Bibliography

Abrahamson, N. A. and Bolt, B. A. (1987). *Array analysis and synthesis mapping of strong seismic motion*. Academic Press Inc.

Accaino, F., Tinivella, U., Rossi, G., and Nicolich, R. (2005). Geofluid evidence from analysis of deep crustal seismic data (southern tuscany, italy). *Journal of volcanology and geothermal research*, 148(1):46–59.

Agamennone, G. (1931-1932). Contributo allo studio dei microsismi. *Boll. Soc. Sismolog. Italiana*, XXX:169–194.

Agnew, D. C. and Berger, J. (1978). Vertical seismic noise at very low frequencies. *Journal of Geophysical Research: Solid Earth (1978–2012)*, 83(B11):5420–5424.

Aki, K. (1957). Space and time spectra of stationary stochastic waves, with special reference to microtremors. *Bull. Earthq. Res. Inst.*, (35):415–456.

Aki, K. (1965). A note on the use of microseisms in determining the shallow structures of the earth's crust. *Geophysics*, 30(4):665–666.

Apostolidis, P., Raptakis, D., Roumelioti, Z., and Pitilakis, K. (2004). Determination of s-wave velocity structure using microtremors and spac method applied in thessaloniki (greece). *Soil dynamics and earthquake engineering*, 24(1):49–67.

Ardhuin, F., Balanche, A., Stutzmann, E., and Obrebski, M. (2012). From seismic noise to ocean wave parameters: General methods and validation. *Journal of Geophysical Research: Oceans (1978–2012)*, 117(C5).

Ardhuin, F., Stutzmann, E., Schimmel, M., and Mangeney, A. (2011). Ocean wave sources of seismic noise. *Journal of Geophysical Research: Oceans (1978–2012)*, 116(C9).

Arias, A., Dini, I., Casini, M., Fiordelisi, A., Perticone, I., and Dell'Aiuto, P. (2010). Geoscientific feature update of the larderello–travale geothermal system (italy) for a regional numerical modeling. In *Proceedings World Geothermal Congress*, page 11.

Asten, M. and Henstridge, J. (1984). Array estimators and the use of microseisms for reconnaissance of sedimentary basins. *Geophysics*, 49(11):1828–1837.

Asten, M. W. (1978). Geological control on the three-component spectra of rayleigh-wave microseisms. *Bulletin of the Seismological Society of America*, 68(6):1623–1636.

Asten, M. W. (2006). On bias and noise in passive seismic data from finite circular array data processed using spac methods. *Geophysics*, 71(6):V153–V162.

Aster, R., M. D. and Bromirski, P. (2008). Multi-decadal climate-induced variability in microseisms. 79(2):194–202.

Babcock, J. M., Kirkendall, B. A., and Orcutt, J. A. (1994). Relationships between ocean bottom noise and the environment. *Bulletin of the Seismological Society of America*, 84(6):1991–2007.

Baldi, P., Bellani, S., Ceccarelli, A., Fiordelisi, A., Squarci, P., and Taffi, L. (1995). Geothermal anomalies and structural features of southern tuscany. In *World Geothermal Congress Proceedings Florence*, pages 1287–1291.

Bao, F., Ni, S., Xie, J., Zeng, X., Li, Z., and Li, Z. (2014). Validating accuracy of rayleigh-wave dispersion extracted from ambient seismic noise via comparison with data from a ground-truth earthquake. *Bulletin of the Seismological Society of America*, 104(4):2133–2141.

Barelli, A., Bertini, G., Buonasorte, G., Cappetti, G., and Fiordelisi, A. (2000). Recent deep exploration results at the margins of the larderello-travale geothermal system. In *Proceedings World Geothermal Congress*, pages 965–970.

Barelli, A., Cappetti, G., and Stefani, G. (1995). Results of deep drilling in the larderello-ravale/radicondoli geothermal area. In *Proceedings World Geothermal Congress WGC9, Florence, Italy*, volume 2, pages 1275–1278.

Batini, F., B. G. G. G. P. E. P. M. and Villa, I. (1985). Deep structure, age and evolution of the larderello travale geothermal field. *Geotherm. Res. Comm., Trans.*, 9:1–7.

Batini, F., Brogi, A., Lazzarotto, A., Liotta, D., and Pandeli, E. (2003). Geological features of larderello-travale and mt. amiata geothermal areas (southern tuscany, italy). *Episodes*, 26(3):239–244.

Batini, F., Console, R., and Luongo, G. (1985). Seismological study of larderello—travale geothermal area. *Geothermics*, 14(2):255–272.

Batini, F, F., Lisi, S., and Pinna, E. (1994). Contributo dei profili sismici in pozzo per l'individuazione di potenziali serbatoi geotermici all'interno del basamento metamorfico del campo di bruciano (area di larderello).

Bensen, G., Ritzwoller, M., Barmin, M., Levshin, A., Lin, F., Moschetti, M., Shapiro, N., and Yang, Y. (2007). Processing seismic ambient noise data to obtain reliable broad-band surface wave dispersion measurements. *Geophysical Journal International*, 169(3):1239–1260.

Bensen, G., Ritzwoller, M., and Shapiro, N. (2008). Broadband ambient noise surface wave tomography across the united states. *Journal of Geophysical Research: Solid Earth (1978–2012)*, 113(B5).

Bertani, R., Bertini, G., Cappetti, G., Fiordelisi, A., and Marocco, B. M. (2005). An update of the larderello-travale/radicondoli deep geothermal system. In *Proceedings*, pages 24–29.

Bertelli, T. (1872). Osservazioni sui piccoli movimenti dei pendoli in relazione ad alucuni fenomeni meteorologiche. *Boll. Meteorol. Osserv. Coll. Roma*, (9):10.

Bertini, G., Cameli, G., Costantini, A., Decandia, F., Dini, I., Elter, F., Lazzarotto, A., Liotta, D., Pandeli, E., and Sandrelli, F. (1994). Structural features of southern tuscany along the monti di campiglia-rapolano terme cross-section. *Mem. Soc. Geol. It*, 48:51–59.

Bertini, G., Casini, M., Gianelli, G., and Pandeli, E. (2006). Geological structure of a long-living geothermal system, larderello, italy. *Terra Nova*, 18(3):163–169.

Bettig, B., Bard, P., Scherbaum, F., Riepl, J., Cotton, F., Cornou, C., and Hatzfeld, D. (2001). Analysis of dense array noise measurements using the modified spatial auto-correlation method (spac): application to the grenoble area. *Bollettino di Geofisica Teorica ed Applicata*, 42(3-4):281–304.

Brogi, A., Lazzarotto, A., Liotta, D., and Ranalli, G. (2003). Extensional shear zones as imaged by reflection seismic lines: the larderello geothermal field (central italy). *Tectonophysics*, 363(1):127–139.

Bromirski, P. D. (2001). Vibrations from the "perfect storm". *Geochemistry, Geophysics, Geosystems*, 2(7).

Bromirski, P. D. and Duennebier, F. K. (2002). The near-coastal microseism spectrum: Spatial and temporal wave climate relationships. *Journal of Geophysical Research: Solid Earth (1978–2012)*, 107(B8):ESE–5.

Bromirski, P. D., Duennebier, F. K., and Stephen, R. A. (2005). Mid-ocean microseisms. *Geochemistry, Geophysics, Geosystems*, 6(4).

Bromirski, P. D., Flick, R. E., and Graham, N. (1999). Ocean wave height determined from inland seismometer data: Implications for investigating wave climate changes in the ne pacific. *Journal of Geophysical Research: Oceans (1978–2012)*, 104(C9):20753–20766.

Brzak, K., Gu, Y. J., Ökeler, A., Steckler, M., and Lerner-Lam, A. (2009). Migration imaging and forward modeling of microseismic noise sources near southern italy. *Geochemistry, Geophysics, Geosystems*, 10(1).

Calcagnile, G. and Panza, G. (1980). The main characteristics of the lithosphere-asthenosphere system in italy and surrounding regions. *Pure and Applied Geophysics*, 119(4):865–879.

Calkins, J. A., Abers, G. A., Ekström, G., Creager, K. C., and Rondenay, S. (2011). Shallow structure of the cascadia subduction zone beneath western washington from spectral ambient noise correlation. *Journal of Geophysical Research: Solid Earth (1978–2012)*, 116(B7).

Calò, M., Kinnaert, X., and Dorbath, C. (2013). Procedure to construct three-dimensional models of geothermal areas using seismic noise cross-correlations: application to the soultz-sous-forêts enhanced geothermal site. *Geophysical Journal International*, page ggt205.

Cameli, G., Dini, I., and Liotta, D. (1993). Upper crustal structure of the larderello geothermal field as a feature of post-collisional extensional tectonics (southern tuscany, italy). *Tectonophysics*, 224(4):413–423.

Cameli, G., Dini, I., and Liotta, D. (1998). Brittle/ductile boundary from seismic reflection lines of southern tuscany (northern apennines, italy). *Mem. Soc. Geol. It*, 52:153–162.

Campillo, M. (2006). Phase and correlation inrandom'seismic fields and the reconstruction of the green function. *Pure and Applied Geophysics*, 163(2-3):475–502.

Campillo, M. and Paul, A. (2003). Long-range correlations in the diffuse seismic coda. *Science*, 299(5606):547–549.

Capon, J. (1969). High-resolution frequency-wavenumber spectrum analysis. *Proceedings of the IEEE*, 57(8):1408–1418.

Capon, J. (1972). Long-period signal processing results for lasa, norsar and alpa. *Geophysical Journal International*, 31(1-3):279–296.

Cappetti, G., Fiordelisi, A., Casini, M., Ciuffi, S., and Mazzotti, A. (2005). A new deep exploration program and preliminary results of a 3d seismic survey in the larderello-travale geothermal field (italy). In *Proceedings 2005 World Geothermal Congress, Antalia, Turkey*.

Casini, M., Ciuffi, S., Fiordelisi, A., Mazzotti, A., Perticone, I., Spinelli, E., and Stucchi, E. (2009). 3d seismic for the deep exploration of the travale geothermal field (italy): I-get project results. In *Geothermal Resources Council annual meeting*, pages 1035–1039. Geothermal Resources Council.

Cessaro, R. K. (1994). Sources of primary and secondary microseisms. *Bulletin of the Seismological Society of America*, 84(1):142–148.

Chávez-García, F. J. and Rodríguez, M. (2007). The correlation of microtremors: empirical limits and relations between results in frequency and time domains. *Geophysical Journal International*, 171(2):657–664.

Chávez-García, F. J., Rodríguez, M., and Stephenson, W. (2006). Subsoil structure using spac measurements along a line. *Bulletin of the Seismological Society of America*, 96(2):729–736.

Chávez-García, F. J., Rodríguez, M., and Stephenson, W. R. (2005). An alternative approach to the spac analysis of microtremors: exploiting stationarity of noise. *Bulletin of the Seismological Society of America*, 95(1):277–293.

Chevrot, S., Sylvander, M., Benahmed, S., Ponsolles, C., Lefevre, J., and Paradis, D. (2007). Source locations of secondary microseisms in western europe: Evidence for both coastal and pelagic sources. *Journal of Geophysical Research: Solid Earth (1978–2012)*, 112(B11).

Chouet, B., De Luca, G., Milana, G., Dawson, P., Martini, M., and Scarpa, R. (1998). Shallow velocity structure of stromboli volcano, italy, derived from small-aperture array measurements of strombolian tremor. *Bulletin of the Seismological Society of America*, 88(3):653–666.

Claerbout, J. F. (1968). Synthesis of a layered medium from its acoustic transmission response. *Geophysics*, 33(2):264–269.

Console, R. and Rosini, R. (1998). Non-double-couple microearthquakes in the geothermal field of larderello, central italy. *Tectonophysics*, 289(1):203–220.

Cox, H. (1973). Spatial correlation in arbitrary noise fields with application to ambient sea noise. *The Journal of the Acoustical Society of America*, 54(5):1289–1301.

De Matteis, R., Vanorio, T., Zollo, A., Ciuffi, S., Fiordelisi, A., and Spinelli, E. (2008). Three-dimensional tomography and rock properties of the larderello-travale geothermal area, italy. *Physics of the Earth and Planetary Interiors*, 168(1):37–48.

De Verdière, Y. C. (2006a). Mathematical models for passive imaging i: general background. *arXiv preprint math-ph/0610043*.

De Verdière, Y. C. (2006b). Mathematical models for passive imaging ii: Effective hamiltonians associated to surface waves. *arXiv preprint math-ph/0610044*.

Derode, A., Larose, E., Tanter, M., De Rosny, J., Tourin, A., Campillo, M., and Fink, M. (2003). Recovering the green's function from field-field correlations in an open scattering medium (l). *The Journal of the Acoustical Society of America*, 113(6):2973–2976.

Duvall, T., Jeffferies, S., Harvey, J., and Pomerantz, M. (1993). Time–distance helioseismology.

Dziewonski, A., Bloch, S., and Landisman, M. (1969). A technique for the analysis of transient seismic signals. *Bulletin of the Seismological Society of America*, 59(1):427–444.

Ebeling, C. W. (2012). 1 inferring ocean storm characteristics from ambient seismic noise: A historical perspective. *Advances in Geophysics*, 53:1.

Ekström, G., Abers, G. A., and Webb, S. C. (2009). Determination of surface-wave phase velocities across usarray from noise and aki's spectral formulation. *Geophysical Research Letters*, 36(18):L18301.

Essen, H.-H., Klussmann, J., Herber, R., and Grevemeyer, I. (1999). Does microseisms in hamburg (germany) reflect the wave climate in the north atlantic? *Deutsche Hydrografische Zeitschrift*, 51(1):33–45.

Essen, H.-H., Krüger, F., Dahm, T., and Grevemeyer, I. (2003). On the generation of secondary microseisms observed in northern and central europe. *Journal of Geophysical Research: Solid Earth (1978–2012)*, 108(B10).

Ferrazzini, V., Aki, K., and Chouet, B. (1991). Characteristics of seismic waves composing hawaiian volcanic tremor and gas-piston events observed by a near-source array. *Journal of Geophysical Research: Solid Earth (1978–2012)*, 96(B4):6199–6209.

Fokkema, J. T. and van den Berg, P. M. (1993). *Seismic applications of acoustic reciprocity*, volume 552. Elsevier.

Foulger, G. (1982). Geothermal exploration and reservoir monitoring using earthquakes and the passive seismic method. *Geothermics*, 11(4):259–268.

Friedrich, A., Krüger, F., and Klinge, K. (1998). Ocean-generated microseismic noise located with the gräfenberg array. *Journal of Seismology*, 2(1):47–64.

Garus, D. and Wegler, U. (2011). The green's functions constructed from 17 years of ambient seismic noise recorded at ten stations of the german regional seismic network. *Bulletin of the Seismological Society of America*, 101(6):2833–2842.

Gerstoft, P., Fehler, M. C., and Sabra, K. G. (2006a). When katrina hit california. *Geophysical Research Letters*, 33(17).

Gerstoft, P., Sabra, K. G., Roux, P., Kuperman, W., and Fehler, M. C. (2006b). Green's functions extraction and surface-wave tomography from microseisms in southern california. *Geophysics*, 71(4):SI23–SI31.

Gerstoft, P., Shearer, P. M., Harmon, N., and Zhang, J. (2008). Global p, pp, and pkp wave microseisms observed from distant storms. *Geophysical Research Letters*, 35(23).

Gerstoft, P. and Tanimoto, T. (2007). A year of microseisms in southern california. *Geophysical Research Letters*, 34(20):L20304.

Godin, O. A. (2006). Recovering the acoustic green's function from ambient noise cross correlation in an inhomogeneous moving medium. *Physical review letters*, 97(5):054301.

Godin, O. A. (2010). Cross-correlation function of acoustic fields generated by random high-frequency sources. *The Journal of the Acoustical Society of America*, 128(2):600–610.

Goldstein, P .and Snoke, A. (2005). Sac availability for the iris community. *Incorporated Institutions for Seismology Data Management Center Electronic Newsletter*, 7:1–6.

Goldstein, P., Dodge, D., Firpo, M., and Minner, L. (2003). Sac2000: Signal processing and analysis tools for seismologists and engineers, invited contribution to whk lee, h. kanamori, pc jennings, and c. kisslinger, eds. *The IASPEI International Handbook of Earthquake and Engineering Seismology*, 81:1613–1620.

Gouedard, P., Stehly, L., Brenguier, F., Campillo, M., Colin de Verdiere, Y., Larose, E., Margerin, L., Roux, P., Sánchez-Sesma, F. J., Shapiro, N., et al. (2008). Cross-correlation of random fields: mathematical approach and applications. *Geophysical prospecting*, 56(3):375–393.

Grevemeyer, I., Herber, R., and Essen, H.-H. (2000). Microseismological evidence for a changing wave climate in the northeast atlantic ocean. *Nature*, 408(6810):349–352.

Gualtieri, L., Stutzmann, E., Capdeville, Y., Ardhuin, F., Schimmel, M., Mangeney, A., and Morelli, A. (2013). Modelling secondary microseis-

mic noise by normal mode summation. *Geophysical Journal International*, 193(3):1732–1745.

Gutenberg, B. (1958). Microseisms. *Advances in Geophysics*, 5:53–92.

Hasselmann, K. (1963). A statistical analysis of the generation of microseisms. *Reviews of Geophysics*, 1(2):177–210.

Hasselmann, K. (1974). On the spectral dissipation of ocean waves due to white capping. *Boundary-Layer Meteorology*, 6(1-2):107–127.

Hasselmann, K., Barnett, T., Bouws, E., Carlson, H., Cartwright, D., Enke, K., Ewing, J., Gienapp, H., Hasselmann, D., Kruseman, P., et al. (1973). Measurements of wind-wave growth and swell decay during the joint north sea wave project (jonswap).

Haubrich, R., Munk, W., and Snodgrass, F. (1963). Comparative spectra of microseisms and swell. *Bulletin of the Seismological Society of America*, 53(1):27–37.

Haubrich, R. A. and McCamy, K. (1969). Microseisms: Coastal and pelagic sources. *Reviews of Geophysics*, 7(3):539–571.

Henstridge, J. D. (1979). A signal processing method for circular arrays. *Geophysics*, 44(2):179–184.

Hillers, G., Ben-Zion, Y., Landes, M., and Campillo, M. (2013). Interaction of microseisms with crustal heterogeneity: A case study from the san jacinto fault zone area. *Geochemistry, Geophysics, Geosystems*, 14(7):2182–2197.

Kedar, S., Longuet-Higgins, M., Webb, F., Graham, N., Clayton, R., and Jones, C. (2008). The origin of deep ocean microseisms in the north atlantic ocean. *Proceedings of the Royal Society A: Mathematical, Physical and Engineering Science*, 464(2091):777–793.

Kennett, B., Brown, D., Sambridge, M., and Tarlowski, C. (2003). Signal parameter estimation for sparse arrays. *Bulletin of the Seismological Society of America*, 93(4):1765–1772.

Kibblewhite, A. and Wu, C. (1991). The theoretical description of wave–wave interactions as a noise source in the ocean. *The Journal of the Acoustical Society of America*, 89(5):2241–2252.

Köhler, A., Ohrnberger, M., Scherbaum, F., Wathelet, M., and Cornou, C. (2007). Assessing the reliability of the modified three-component spatial autocorrelation technique. *Geophysical Journal International*, 168(2):779–796.

Koper, K. D., Seats, K., and Benz, H. (2010). On the composition of earth's short-period seismic noise field. *Bulletin of the Seismological Society of America*, 100(2):606–617.

Kundu, P., Cohen, I., and Dowling, D. (2012). Fluid mechanics, 920 pp.

Lacoss, R., Kelly, E., and Toksöz, M. (1969). Estimation of seismic noise structure using arrays. *Geophysics*, 34(1):21–38.

Landès, M., Hubans, F., Shapiro, N., Paul, A., and Campillo, M. (2010). Origin of deep ocean microseisms by using teleseismic body waves. *Journal of Geophysical Research*, 115(B5):B05302.

Larose, E., Derode, A., Campillo, M., and Fink, M. (2004). Imaging from one-bit correlations of wideband diffuse wave fields. *Journal of Applied Physics*, 95(12):8393–8399.

Larose, E., Khan, A., Nakamura, Y., and Campillo, M. (2005). Lunar subsurface investigated from correlation of seismic noise. *Geophysical Research Letters*, 32(16).

Larose, E., Margerin, L., Derode, A., van Tiggelen, B., Campillo, M., Shapiro, N., Paul, A., Stehly, L., and Tanter, M. (2006). Correlation of random wavefields: An interdisciplinary review. *Geophysics*, 71(4):SI11–SI21.

Lehujeur, M., V. J. M. A. S. J. (2013). Imaging of a deep geothermal reservoir using ambient noise correlation. In *Proceedings of the European Geothermal Congress*.

Levshin, A., Ratnikova, L., and Berger, J. (1992). Peculiarities of surface-wave propagation across central eurasia. *Bulletin of the Seismological Society of America*, 82(6):2464–2493.

Levshin, A. and Ritzwoller, M. (2001). Automated detection, extraction, and measurement of regional surface waves. In *Monitoring the Comprehensive Nuclear-Test-Ban Treaty: Surface Waves*, pages 1531–1545. Springer.

Levshin, A.L., Y. T. L. A. B. B. B. M. R. L. . I. E. (1989). Seismic surface waves in a laterally inhomogeneous earth.

Li, H., Bernardi, F., and Michelini, A. (2010). Surface wave dispersion measurements from ambient seismic noise analysis in italy. *Geophysical Journal International*, 180(3):1242–1252.

Lin, F.-C., Moschetti, M. P., and Ritzwoller, M. H. (2008). Surface wave tomography of the western united states from ambient seismic noise: Rayleigh and love wave phase velocity maps. *Geophysical Journal International*, 173(1):281–298.

Lin, F.-C., Ritzwoller, M. H., Townend, J., Bannister, S., and Savage, M. K. (2007). Ambient noise rayleigh wave tomography of new zealand. *Geophysical Journal International*, 170(2):649–666.

Liotta, D. and Ranalli, G. (1999). Correlation between seismic reflectivity and rheology in extended lithosphere: southern tuscany, inner northern apennines, italy. *Tectonophysics*, 315(1):109–122.

Lobkis, O. I. and Weaver, R. L. (2001). On the emergence of the green's function in the correlations of a diffuse field. *The Journal of the Acoustical Society of America*, 110:3011.

Longuet-Higgins, M. S. (1950). A theory of the origin of microseisms. *Philosophical Transactions of the Royal Society of London. Series A, Mathematical and Physical Sciences*, 243(857):1–35.

Lund, J. W. (2004). 100 years of geothermal power production. *Geo-Heat Center Bulletin*, 25(3):11–19.

Ma, S., Prieto, G., and Beroza, G. (2008). Testing community velocity models for southern california using the ambient seismic field. *Bulletin of the Seismological Society of America*, 98(6):2694–2714.

Maraschini, M., Ernst, F., Foti, S., and Socco, V. L. (2010). A new misfit function for multimodal inversion of surface waves. *Geophysics*, 75(4):G31–G43.

Maresca, R., Galluzzo, D., and Del Pezzo, E. (2006). H/v spectral ratios and array techniques applied to ambient noise recorded in the colfiorito basin, central italy. *Bulletin of the Seismological Society of America*, 96(2):490–505.

Marzorati, S. and Bindi, D. (2008). Characteristics of ambient noise cross correlations in northern italy within the frequency range of 0.1–0.6 hz. *Bulletin of the Seismological Society of America*, 98(3):1389–1398.

Miche, M. (1944). Mouvements ondulatoires de lamer en profondeur constante ou decroissante. *Annales des Ponts et Chaussees*, 114:25–78.

Milne, J. (1883). Earth pulsations. *Nature*, 28:367–370.

Minissale, A. (1991). The larderello geothermal field: a review. *Earth-Science Reviews*, 31(2):133–151.

Mordret, A., Landès, M., Shapiro, N., Singh, S., Roux, P., and Barkved, O. (2013). Near-surface study at the valhall oil field from ambient noise surface wave tomography. *Geophysical Journal International*, 193(3):1627–1643.

Morse, P. M. and Feshbach, H. (1953). *Methods of Theoretical Physics, Part I.* McGraw-Hill Science/Engineering/Math.

Moschetti, M., Ritzwoller, M., and Shapiro, N. (2007). Surface wave tomography of the western united states from ambient seismic noise: Rayleigh wave group velocity maps. *Geochemistry, Geophysics, Geosystems*, 8(8).

Munk, W. H., Snodgrass, F. E., and Tucker, M. J. (1959). *Spectra of low-frequency ocean waves.* University of California Press.

Nishida, K., Kawakatsu, H., Fukao, Y., and Obara, K. (2008). Background love and rayleigh waves simultaneously generated at the pacific ocean floors. *Geophysical Research Letters*, 35(16).

Obrebski, M., Ardhuin, F., Stutzmann, E., and Schimmel, M. (2012). How moderate sea states can generate loud seismic noise in the deep ocean. *Geophysical Research Letters*, 39(11).

Okada, H. (2006). Theory of efficient array observations of microtremors with special reference to the spac method. *Exploration Geophysics*, 37(1):73–85.

Okada, H. and Suto, K. (2003). *The microtremor survey method*, volume 12. Society of Exploration Geophysicists with the cooperation of Society of Exploration Geophysicists of Japan [and] Australian Society of Exploration Geophysicists.

Orcutt, J. A., Cox, C. S., Kibblewhite, A. C., Kuperman, W., and Schmidt, H. (1993). Observations and causes of ocean and seafloor noise at ultra-low and very-low frequencies. In *Natural physical sources of underwater sound*, pages 203–232. Springer.

Paul, A., Campillo, M., Margerin, L., Larose, E., and Derode, A. (2005). Empirical synthesis of time-asymmetrical green functions from the correlation of coda waves. *Journal of Geophysical Research: Solid Earth (1978–2012)*, 110(B8).

Pedersen, H. A. and Krüger, F. (2007). Influence of the seismic noise characteristics on noise correlations in the baltic shield. *Geophysical Journal International*, 168(1):197–210.

Peterson, J. (1993). Observations and modeling of seismic background noise.

Piccinini, D., Saccorotti, G., Mazzarini, F., Zupo, M., Capello, M., Musumeci, G., Cauchie, L., and Chiarabba, C. (2013). Passive, broad-band

seismic measurements for geothermal exploration: the gapss experiment. In *Proceedings of the European Geothermal Congress*.

Pierson, W. J. and Moskowitz, L. (1964). A proposed spectral form for fully developed wind seas based on the similarity theory of sa kitaigorodskii. *Journal of geophysical research*, 69(24):5181–5190.

Poli, P., Campillo, M., Pedersen, H. A., et al. (2012). Seismic noise tomography in regions with small velocity contrasts and strong noise directivity: application to the northern baltic shield.

Prieto, G. A., Denolle, M., Lawrence, J. F., and Beroza, G. C. (2011). On amplitude information carried by the ambient seismic field. *Comptes Rendus Geoscience*, 343(8):600–614.

Prieto, G. A., Lawrence, J. F., and Beroza, G. C. (2009). Anelastic earth structure from the coherency of the ambient seismic field. *Journal of Geophysical Research: Solid Earth (1978–2012)*, 114(B7).

Rhie, J. and Romanowicz, B. (2004). Excitation of earth's continuous free oscillations by atmosphere–ocean–seafloor coupling. *Nature*, 431(7008):552–556.

Rickett, J. and Claerbout, J. (1999). Acoustic daylight imaging via spectral factorization: Helioseismology and reservoir monitoring. *The leading edge*, 18(8):957–960.

Ritzwoller, M. H., Lin, F.-C., and Shen, W. (2011). Ambient noise tomography with a large seismic array. *Comptes Rendus Geoscience*, 343(8):558–570.

Roberts, J. C. and Asten, M. W. (2004). Resolving a velocity inversion at the geotechnical scale using the microtremor (passive seismic) survey method. *Exploration geophysics*, 35(1):14–18.

Roux, P., Kuperman, W., Group, N., et al. (2004a). Extracting coherent wave fronts from acoustic ambient noise in the ocean. *The Journal of the Acoustical Society of America*, 116(4):1995–2003.

Roux, P., Kuperman, W. A., Hodgkiss, W. S., Song, H. C., Akal, T., and Stevenson, M. (2004b). A nonreciprocal implementation of time reversal in the ocean. *The Journal of the Acoustical Society of America*, 116(2):1009–1015.

Roux, P., Sabra, K. G., Gerstoft, P., Kuperman, W., and Fehler, M. C. (2005). P-waves from cross-correlation of seismic noise. *Geophysical Research Letters*, 32(19).

Roux, P., Song, H. C., and Kuperman, W. (2003). Time-reversal using ambient noise as a probe source. *The Journal of the Acoustical Society of America*, 113(4):2218–2218.

Ruigrok, E., Campman, X., Draganov, D., and Wapenaar, K. (2010). High-resolution lithospheric imaging with seismic interferometry. *Geophysical Journal International*, 183(1):339–357.

Ruigrok, E., Campman, X., and Wapenaar, K. (2011). Extraction of p-wave reflections from microseisms. *Comptes Rendus Geoscience*, 343(8):512–525.

Sabra, K., Gerstoft, P., Roux, P., Kuperman, W., and Fehler, M. (2005a). Extracting time-domain green's function estimates from ambient seismic noise. *Geophysical Research Letters*, 32(3):L03310.

Sabra, K. G., Gerstoft, P., Roux, P., Kuperman, W., and Fehler, M. C. (2005b). Surface wave tomography from microseisms in southern california. *Geophysical Research Letters*, 32(14).

Sabra, K. G., Roux, P., and Kuperman, W. (2005c). Emergence rate of the time-domain green's function from the ambient noise cross-correlation function. *The Journal of the Acoustical Society of America*, 118(6):3524–3531.

Saccorotti, G., Chouet, B., and Dawson, P. (2003). Shallow-velocity models at the kilauea volcano, hawaii, determined from array analyses of tremor wavefields. *Geophysical Journal International*, 152(3):633–648.

Saccorotti, G., Piccinini, D., Mazzarini, F., and Zupo, M. (2013). Remotely triggered micro-earthquakes in the larderello-travale geothermal field (italy) following the 2012 may 20, mw 5.9 po-plain earthquake. *Geophysical Research Letters*, 40(5):835–840.

Saccorotti, G., Piccinini, D., Zupo, M., Mazzarini, F., Chiarabba, C., Agostinetti, N. P., Licciardi, A., and Bagagli, M. (2014). The deep structure of the larderello-travale geothermal field (italy) from integrated, passive seismic investigations. *Energy Procedia*, 59:227–234.

Sambridge, M. (1999a). Geophysical inversion with a neighbourhood algorithm—i. searching a parameter space. *Geophysical Journal International*, 138(2):479–494.

Sambridge, M. (1999b). Geophysical inversion with a neighbourhood algorithm—ii. appraising the ensemble. *Geophysical Journal International*, 138(3):727–746.

Sánchez-Sesma, F. and Campillo, M. (2006). Retrieval of the green's function from cross correlation: the canonical elastic problem. *Bulletin of the Seismological Society of America*, 96(3):1182–1191.

Sánchez-Sesma, F. J., Pérez-Ruiz, J. A., Luzon, F., Campillo, M., and Rodríguez-Castellanos, A. (2008). Diffuse fields in dynamic elasticity. *Wave motion*, 45(5):641–654.

Savage, M. K., Lin, F.-C., and Townend, J. (2013). Ambient noise cross-correlation observations of fundamental and higher-mode rayleigh wave propagation governed by basement resonance. *Geophysical Research Letters*, 40(14):3556–3561.

Schulte-Pelkum, V., Earle, P. S., and Vernon, F. L. (2004). Strong directivity of ocean-generated seismic noise. *Geochemistry, Geophysics, Geosystems*, 5(3).

Seats, K. J., Lawrence, J. F., and Prieto, G. A. (2012). Improved ambient noise correlation functions using welch's method. *Geophysical Journal International*, 188(2):513–523.

Shapiro, N. M. and Campillo, M. (2004). Emergence of broadband rayleigh waves from correlations of the ambient seismic noise. *Geophysical Research Letters*, 31(7).

Shapiro, N. M., Campillo, M., Stehly, L., and Ritzwoller, M. H. (2005). High-resolution surface-wave tomography from ambient seismic noise. *Science*, 307(5715):1615–1618.

Shapiro, N. M., Ritzwoller, M., and Bensen, G. (2006). Source location of the 26 sec microseism from cross-correlations of ambient seismic noise. *Geophysical research letters*, 33(18).

Slob, E. and Wapenaar, K. (2007). Electromagnetic green's functions retrieval by cross-correlation and cross-convolution in media with losses. *Geophysical Research Letters*, 34(5).

Snieder, R. (2004). Extracting the green's function from the correlation of coda waves: A derivation based on stationary phase. *Physical Review E*, 69(4):046610.

Socco, V. L., Strobbia, C., and Foti, S. (2002). Multimodal interpretation of surface wave data. In *8th EEGS-ES Meeting*.

Stachnik, J., Dueker, K., Schutt, D., and Yuan, H. (2008). Imaging yellowstone plume-lithosphere interactions from inversion of ballistic and diffusive rayleigh wave dispersion and crustal thickness data. *Geochemistry, Geophysics, Geosystems*, 9(6).

Stehly, L., Campillo, M., and Shapiro, N. (2006). A study of the seismic noise from its long-range correlation properties. *Journal of Geophysical Research: Solid Earth (1978–2012)*, 111(B10).

Stutzmann, E., Ardhuin, F., Schimmel, M., Mangeney, A., and Patau, G. (2012). Modelling long-term seismic noise in various environments. *Geophysical Journal International*, 191(2):707–722.

Stutzmann, E., Roult, G., and Astiz, L. (2000). Geoscope station noise levels. *Bulletin of the Seismological Society of America*, 90(3):690–701.

Stutzmann, E., Schimmel, M., Patau, G., and Maggi, A. (2009). Global climate imprint on seismic noise. *Geochemistry, Geophysics, Geosystems*, 10(11).

Tanimoto, T. (2007). Excitation of microseisms. *Geophysical research letters*, 34(5):L05308.

Tanimoto, T., Ishimaru, S., and Alvizuri, C. (2006). Seasonality in particle motion of microseisms. *Geophysical Journal International*, 166(1):253–266.

Tarantola, A. and Valette, B. (1982). Generalized nonlinear inverse problems solved using the least squares criterion. *Reviews of Geophysics*, 20(2):219–232.

ToksöZ, M. N. and Lacoss, R. T. (1968). Microseisms: Mode structure and sources. *Science*, 159(3817):872–873.

Traer, J., Gerstoft, P., Bromirski, P. D., Hodgkiss, W. S., and Brooks, L. A. (2008). Shallow-water seismoacoustic noise generated by tropical storms ernesto and florence. *The Journal of the Acoustical Society of America*, 124(3):EL170–EL176.

Tsai, V. C. and Moschetti, M. P. (2010). An explicit relationship between time-domain noise correlation and spatial autocorrelation (spac) results. *Geophysical Journal International*, 182(1):454–460.

Vanorio, T., De Matteis, R., Zollo, A., Batini, F., Fiordelisi, A., and Ciulli, B. (2004). The deep structure of the larderello-travale geothermal field from 3d microearthquake traveltime tomography. *Geophysical research letters*, 31(7):L07613.

Verbeke, J., Boschi, L., Stehly, L., Kissling, E., and Michelini, A. (2012). High-resolution rayleigh-wave velocity maps of central europe from a dense ambient-noise data set. *Geophysical Journal International*.

Wang, C., Zhang, J., Yan, L., Liu, H., and Zhao, D. (2014). Application of passive source surface-wave method in site engineering seismic survey. *Earthquake Science*, 27(1):101–106.

Wapenaar, C. P. A., Draganov, D., and Robertsson, J. O. (2008). *Seismic interferometry: history and present status*, volume 26. Society of Exploration Geophysicists.

Wapenaar, K. (2006). Green's function retrieval by cross-correlation in case of one-sided illumination. *Geophysical Research Letters*, 33(19).

Wapenaar, K. and Fokkema, J. (2006). Green's function representations for seismic interferometry. *Geophysics*, 71(4):SI33–SI46.

Wapenaar, K., Fokkema, J., and Snieder, R. (2005). Retrieving the green's function in an open system by cross correlation: A comparison of approaches (l). *The Journal of the Acoustical Society of America*, 118(5):2783–2786.

Wapenaar, K., Slob, E., and Snieder, R. (2006). Unified green's function retrieval by cross correlation. *Physical Review Letters*, 97(23):234301.

Wathelet, M. (2005). *Array recordings of ambient vibrations: surface-wave inversion*. PhD thesis, Liége University, Belgium.

Wathelet, M., Jongmans, D., and Ohrnberger, M. (2004). Surface-wave inversion using a direct search algorithm and its application to ambient vibration measurements. *Near surface geophysics*, 2(4):211–221.

Weaver, R. L. and Lobkis, O. I. (2001). Ultrasonics without a source: Thermal fluctuation correlations at mhz frequencies. *Physical Review Letters*, 87(13):134301.

Weaver, R. L. and Lobkis, O. I. (2005). Fluctuations in diffuse field–field correlations and the emergence of the green's function in open systems. *The Journal of the Acoustical Society of America*, 117(6):3432–3439.

Webb, S. C. (1992). The equilibrium oceanic microseism spectrum. *The Journal of the Acoustical Society of America*, 92(4):2141–2158.

Webb, S. C. (1998). Broadband seismology and noise under the ocean. *Reviews of Geophysics*, 36(1):105–142.

Webb, S. C. (2007). The earth's 'hum'is driven by ocean waves over the continental shelves. *Nature*, 445(7129):754–756.

Wielandt, E. (2003). Seismometry. In Lee, W. H., Jennings, P., Kisslinger, C., and Kanamori, H., editors, *International Handbook of Earthquake & Engineering Seismology*. Academic Press.

Yamamoto, H. (2000). Estimation of shallow s-wave velocity structures from phase velocities of love-and rayleigh-waves in microtremors. In *Proceedings of the 12th World Conference on Earthquake Engineering*.

Yang, Y. and Ritzwoller, M. H. (2008). Characteristics of ambient seismic noise as a source for surface wave tomography. *Geochemistry, Geophysics, Geosystems*, 9(2).

Yang, Y., Ritzwoller, M. H., Levshin, A. L., and Shapiro, N. M. (2007). Ambient noise rayleigh wave tomography across europe. *Geophysical Journal International*, 168(1):259–274.

Yao, H., Beghein, C., and Van Der Hilst, R. D. (2008). Surface wave array tomography in se tibet from ambient seismic noise and two-station analysis-ii. crustal and upper-mantle structure. *Geophysical Journal International*, 173(1):205–219.

Yao, H. and Van Der Hilst, R. D. (2009). Analysis of ambient noise energy distribution and phase velocity bias in ambient noise tomography, with application to se tibet. *Geophysical Journal International*, 179(2):1113–1132.

Yao, H., van Der Hilst, R. D., and Maarten, V. (2006). Surface-wave array tomography in se tibet from ambient seismic noise and two-station analysis—i. phase velocity maps. *Geophysical Journal International*, 166(2):732–744.

Yokoi, T. and Margaryan, S. (2008). Consistency of the spatial autocorrelation method with seismic interferometry and its consequence. *Geophysical Prospecting*, 56(3):435–451.

Zhang, J. and Gerstoft, P. (2014). Local-scale cross-correlation of seismic noise from the calico fault experiment. *Earthquake Science*, pages 1–8.

Zhang, J., Gerstoft, P., and Bromirski, P. D. (2010). Pelagic and coastal sources of p-wave microseisms: Generation under tropical cyclones. *Geophysical Research Letters*, 37(15):L15301.

Zhou, L., Xie, J., Shen, W., Zheng, Y., Yang, Y., Shi, H., and Ritzwoller, M. H. (2012). The structure of the crust and uppermost mantle beneath south china from ambient noise and earthquake tomography. *Geophysical Journal International*, 189(3):1565–1583.